ScuDo
Scuola di Dottorato ~ Doctoral School
WHAT YOU ARE, TAKES YOU FAR

Doctoral Dissertation
Doctoral Program in Management and Production Engineering (29^{th}cycle)

Functional modelling and prototyping of electronic integrated kinetic energy harvesters

By

Nicoló Manca

******

Supervisor(s):
Prof. E., Bonisoli
Prof. M., Repetto

Doctoral Examination Committee:
Prof. L., Garbuio, Grenoble Institute of Technology
Prof. E., Rustighi, University of Southampton
Prof. P., Alotto, Universitá degli Studi di Padova
Prof. A., Manuello Bertetto, Universitá di Cagliari
Prof. M.G., Tehrani, University of Southampton

Politecnico di Torino
2017

Declaration

I hereby declare that, the contents and organization of this dissertation constitute my own original work and does not compromise in any way the rights of third parties, including those relating to the security of personal data.

Nicoló Manca
2017

* This dissertation is presented in partial fulfillment of the requirements for **Ph.D. degree** in the Graduate School of Politecnico di Torino (ScuDo).

"Sometimes ignorance is a good thing.
You don't know the problem is insoluble,
so you go ahead and do it"

J. M. Kosterlitz
rock climbing pioneer
and 2016 Nobel Prize in Physics

Acknowledgements

This thesis concludes my work during the last three years at the Politecnico di Torino in the context of a research project funded and carried out in partnership with STMicroelectronics.

I want to sincerely thank my supervisors Dr. Elvio Bonisoli, Associate Professor at the Department of Mechanical and Aerospace Engineering, and Dr. Maurizio Repetto, Full Professor at the Department of Energy, mostly for their guidance and experience, driven force of this work, but also for the time they dedicated to me, the laughs and the fights during our meetings that made my job much more a pleasure and a constant challenge.

A special acknowledgement is addressed to Ing. Alessandro Gasparini, Ing. Stefano Ramorini and Ing. Alberto Cattani of the STMicroelectronics team. Thanks for your support, your knowledge and your experience, essential elements that made possible the results of this project.

I equally acknowledge Dr. Lauric Garbuio, Maître de Conférences at Université Grenoble-Alpes, Dr. Nicolas Galopin, Maître de Conférences at Université Grenoble-Alpes and Dr. Hervé Chazal, Maître de Conférences at Université Grenoble-Alpes, for welcoming me as visiting research student. Sharing your knowledge and experience during eight months, you allowed me to spread my point of view on this topic.

I also thank my desk-neighbours Matteo, Marco and Domenico...because often best ideas comes from coffee-break talkings!

A particular thought goes to my family, to Lucia and to my friends for the support in the good moments and the *slaps* to be back on the path during difficulties.

In the end, thanks to you all as these three years allowed me to grow both as a researcher and both as a person.

Abstract

The aim of developing infinite-life autonomous wireless electronics, powered by the energy of the surrounding environment, drives the research efforts in the field of Energy Harvesting. Electromagnetic and piezoelectric techniques are deemed to be the most attractive technologies for vibrational devices. In the thesis, both these technologies are investigated taking into account the entire energy conversion chain. In the context of the collaboration with the STMicroelectronics, the project of a self-powered Bluetooth step counter embedded in a training shoe has been carried out. A cylindrical device $\varnothing\, 27 \times 16$ mm including the transducer, the interface circuit, the step-counter electronics and the protective shell, has been developed. Environmental energy extraction occurs exploiting the vibration of a permanent magnet in response to the impact of the shoe on the ground. A self-powered electrical interface performs maximum power transfer through optimal resistive load emulation and load decoupling. The device provides 360 µJ to the load, the 90% of the maximum recoverable energy. The energy requirement is four time less than the provided and the effectiveness of the proposed device is demonstrated also considering the foot-steps variability and the performance spread due to prototypes manufacturing. In the context of the collaboration with the G2Elab of Grenoble and STMicroelectronics, the project of a piezoelectric energy harvester has been carried out. With the aim of exploiting environmental vibrations, a uni-morph piezoelectric cantilever beam 60×25×0.5 mm with a proof mass at the free-end has been designed. Numerical results show that electrical interfaces based on SECE and sSSHI techniques allows increasing performance up to the 125% and the 115% of that in case of STD interface. Due to the better performance in terms of harvested power and in terms of electric load decoupling, a self-powered SECE interface has been prototyped. In response to 2 m/s^2 56,2 Hz sinusoidal input, experimental power recovery of 0.56 mW is achieved demonstrating that the device is compliant with standard low-power electronics requirements.

Contents

List of Figures

List of Tables

Chapter 1

Introduction

The work presented in this thesis derives from the PhD programme on energy harvesting of Politecnico di Torino led in partnership with STMicroelectronics, a global semiconductor leader.
The enormous progress made in the field of semiconductor during the last decades drastically reduced energy consumption and size of electronic devices. This, together with the development of the Micro-Electro-Mechanical Systems (MEMS) technology, exponentially increased the panorama of the possible applications leading to the concept of Internet of Things (IoT). In the scenario where electrical devices spread everywhere in the environment, the idea of exploiting the environmental energy itself for power supply, drives the research efforts in the flourishing field of Energy Harvesting. The always growing number of papers and patents, the achieved state-of-the-art and the developed applications, pushed electronics companies to invest on this topic.

In this context, the *Department of Management and Production Engineering* together with the *Department of Energy* of Politecnico di Torino carried out successful projects in collaboration with industrial and academic partners. The energy harvesting system for the Pirelli Cyber Tyre [8] and for computer mouse application [9] represent challenging applications successfully developed. The gained experience during these activities built a grounded base for the energy harvesting project here described.
From the experience of the Politecnico di Torino and the know-how of STMicroelectronics, constantly projected toward the technology innovation research, it takes

shape a collaborative project aiming at investigating both the electromagnetic and both the piezoelectric technology applied to the energy harvesting in order to design and develop functional prototypes. The long term target is to build the set of tools, resources and abilities necessary to make an application idea a functional prototype, reducing design and engineering time in order to rapidly respond to the marked inputs.

The thesis is focus on exploiting the mechanical vibration of a specific environment to power supply an infinite-life device by converting the mechanical energy into electrical via electromagnetic induction and piezoelectric effects. Thus the project is divided into two macro arguments that derive from a unified model describing the kinetic energy harvesting.

After an introductive literature overview on the main energy harvesting techniques and the state-of-the-art, Chapter 2, a unified simplified model valid for both electromagnetic and both piezoelectric technologies is presented and discussed starting from the description of the energy conversion chain in Chapter 3.
System modelling details and power managing techniques for both the considered technologies are presented in Chapter 4. The analysis is focused on the electromechanical conversion phenomenon involved, the generator and transducer modelling, the electrical circuit topologies implemented to optimise the electromechanical coupling and their effect on the energy extraction performance.
Chapter 5 presents the project in the electromagnetic field carried out together with the STMicroelectronics Analog and MEMS Group (AMG) to develop a prototypes batch of self-powered Bluetooth step counter placed in the sole of a training shoe [10]. The device target is to exploit only the energy harvested by the impact of the shoe on the ground to sense the foot-step and send the information to a remote receiver.
Chapter 6 presents the project in the piezoelectric field carried out at the Grenoble Electrical Engineering Laboratory of Grenoble under the supervision of STMicroelectronics AMG to develop a prototype of cantilever beam energy harvester targeted to environmental vibrations.
Lastly, Chapter 7 briefly summarise the outcomes of the thesis and future developments.

Chapter 2

Energy Harvesting techniques

2.1 Motivation

In the last decades, the semiconductor industry made enormous progress in chip manufacturing. The development of lithography technique strongly pushed the boundary of chip density leading to compact, low-power, low-cost, multi-function integrated chips (ICs), and opening the doors of the Micro Electro-Mechanical Systems (MEMS) revolution, Fig. 2.1a [1]. Miniature electronics devices, such as portable mobiles, tablet computers, GPS systems or ambient monitoring sensors, invaded market making possible applications unattainable until few years before and stimulating the development of specific applications such as Wireless Sensor Nodes (WSNs), Structural Health Monitoring (SHM), Non-Destructive Evaluation (NDE) and wearable computing.

In the last years, the concept of Internet of Things (IoT) spread widely in electronics indicating a cluster of miniature electronics devices connected together to collect and exchange data. IoT is a rapidly emerging application space and it is becoming the largest electronics market for the semiconductor industry [11], Fig. 2.1b. In the world of IoT, devices are supposed to appear everywhere in house construction, human health monitoring systems, automatic controlling and logistics networks, making the conventional power grid unsuitable and batteries undesirable for their limited lifespan, maintenance costs and problematic disposal.

With the introduction of Low- and Ultra-Low-Power electronics, the consumption of wireless sensors has been largely reduced [12]: typical power need of mobile

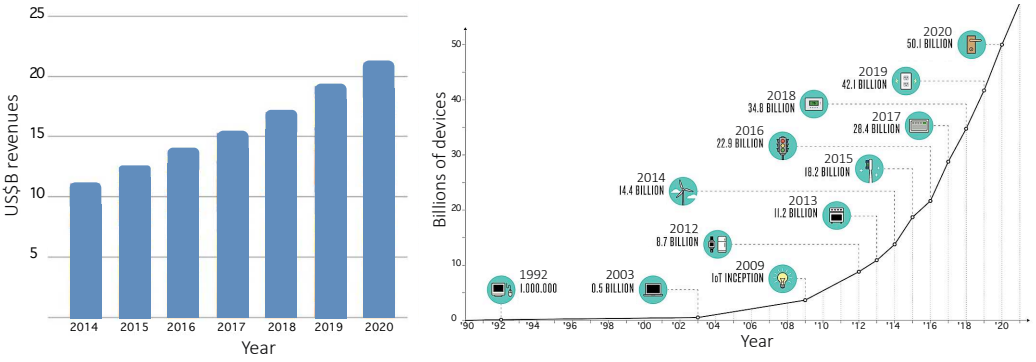

(a) (b)

Fig. 2.1 a) MEMS market trend and forecast [1] and b) electronics device volumes growth with the spread of IoT [2].

devices ranges between hundreds of milliwatts for MP3s, mobile phones and GPS applications to few micro-watts for wristwatches, RFID, MEMS sensors and actuators. Considering that usually the seconds are in a sleep state for the 99.9% of their operation time, waking up for only few milliseconds to transmit data, their average power consumption is below 10 µW.

A standard lithium battery can provide about 30 µW/cc for 1 year while a vibration-driven generator could last for at least 50 years with the same power level [13]. In this way, large research interest was attracted by the concept of *ubiquitous energy*. Energy is everywhere in the environment surrounding us, present in different forms. By exploiting appropriate phenomena and materials, it is possible to harvest environmental energy converting it into ready-to-use electrical energy for storing otherwise supplying battery-less devices. In most cases, the recovered energy would be wasted with no specific use in the environment. In other cases, energy is recovered from sources that are not significantly influenced by this process.

The idea of developing infinite-life autonomous wireless electronics, powered recovering wasted energy, drives the research efforts in the flourishing field of Energy Harvesting, as the exponential increasing in the number of patents since the early '90s demonstrates, Fig 2.2.

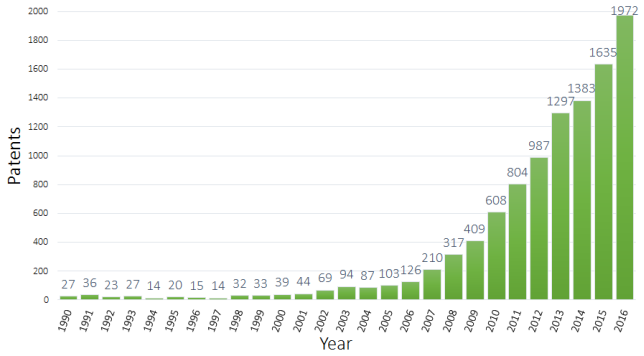

Fig. 2.2 Energy Harvesting patents since 1990 [3].

2.2 Energy harvesting techniques

Energy harvesting, or sometimes energy scavenging, is the process consisting in the conversion of ambient energy present in the environment into directly available electrical energy. Due to the small amounts of energy available in the surrounding ambient, typically, energy harvesting is applied to supply small-scale, low-power electronic devices. The target device can be driven synchronously, using right away the recovered energy, or asynchronously, recharging temporary storage systems as super-capacitors or thin film Lithium batteries for future use. Capacitors are usually preferred as temporary storage systems for their longer lifetime, higher power density and fast recharging [14].

According to Thomas et al. [15], energy present in the surrounding ambient can be classified in five different categories: kinetic (mechanical motion like biological energy, vibrational or intermittent sources), photonic (like light sources), thermal (temperature gradients or time variation), electromagnetic (like electromagnetic field differences or electromagnetic waves), and autophagus structure-power. In [16], Harb includes in the list also radioactive reactions and micro water flow. In [4, 5] chemical sources are considered.

In order to convert these kinds of energy into electrical, for each situation a transducer exploiting peculiar phenomena and materials is required. A well documented and comprehensive state-of-the-art review on energy harvesting techniques have been made by Rabaey et al. [17], Roundy et al. [18], Paradiso and Starner [19], Thomas et al. [15], Vullers et al. [20], Cantatore and Ouwerkerk [21], Mitcheson et al. [22], Harb [16], Matiko et al. [23] and Vocca et al. [14], while Oudenhoven et al. [24] proposed a performance analysis of batteries for autonomous sensor systems. Here,

the state-of-the-art in terms of research progress and commercial products is only briefly outlined for a more clear understanding and comparison.

2.2.1 Limitations of batteries

Autonomous wireless electronics are very attractive devices. In an IoT network and even in a stand-alone device, the absence of cables means ease of installation, deployment and re-deployment. Typically these devices are battery-powered so, if on the one hand they present the advantage of being wireless, on the other they are affected by the limitations characteristic of the batteries themselves [23].

The difference between device and battery life-span is a critical aspect. As the device is always designed to operate for a longer period than the battery duration, at some point replacing or recharging is required. In addition to the service disruption during substitution, maintenance costs have to be considered, especially when a large amount of devices are deployed in a network. Another aspect to be considered is the the self-discharging. In case of very low-power electronic systems, or systems dormant most of the time, considering the average power consumption and the battery capacity, it can be theoretically expected to have a device operative for a very extended period of time. However, due to internal chemical reactions, batteries self-discharge over time and the following depletion becomes a limiting factor. Third, indirect but not less critical issue is the batteries disposal as they contain chemicals, hazardous both to the environment and to health if not carefully handled.

All these weaknesses make energy harvesting a compelling alternative to batteries as avoids maintenance costs, life-span problem and disposal issue of batteries, capturing and exploiting otherwise wasted energy.

2.2.2 Photonic energy harvesting

Energy harvesting from light sources exploits photovoltaic phenomenon. The so-called photovoltaic effect can convert light into electricity via materials such as monocrystalline silicon, multicrystalline silicon and cadmimum telluride [25]. When light strikes these materials, part of the photons is absorbed. The energy of the photon is transferred to an electron that is able to escape from its normal position in

an atom. As these materials are semiconductors, electrons flow through the material becoming electrical current in a circuit.

Photovoltaic energy harvesting is the most common method of harvesting energy and is now a well-established technology. Energy can be recovered both from natural sun light and both from artificial light using solar cells also known as photovoltaic cells. Cells can be represented as semiconductor diodes with a large p-n junction in the plane of the cell. When exposed to light, electric potential is developed between the p and n-type materials, Fig. 2.3.

The amount of harvested power depends on the intensity, spectral content, incident angle of the light falling on the surface of the cell, and on the size, sensitivity, temperature and type of the cells itself. During a bright sunny day, about 1 kW/m^2 of solar power hits a cell surface directly facing the sun. Conversion efficiency ranges from 8 up to 30% for commercial devices, reaching about 35% in some experimental prototypes.

Typically, rigid-substrate semiconductor devices are employed as these have higher efficiencies. However, if installation on non-flat surfaces or flexibility are required, third generation, thin film, photovoltaic cells and modules known as dye-sensitized solar cells (DSSCs) on a flexible substrate are present on the market.

In order to improve efficiency and obtain the maximum power transfer, sun tracking techniques [26] and Maximum Power Point Tracking (MPPT) methods [27] are applied. In general, sun tracking aims to move the harvesting system to compensate the source motion keeping the best orientation, while MPPT aims to automatically find the output voltage or current at which the cell reaches its maximum power point.

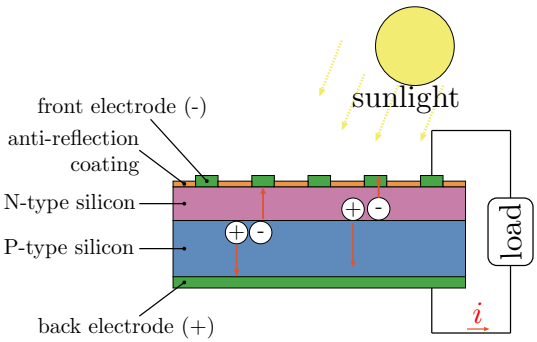

Fig. 2.3 Photovoltaic cell working principle.

Electronic consumer products powered by light sources are increasing in the market. Also standalone solar-powered wireless sensor nodes for wireless sensor networks are commercially available.

2.2.3 Thermal energy harvesting

Thermal energy can be harvested exploiting temperature gradients or temperature fluctuation. In the first case the involved phenomena is the thermoelectric effect, while in the second is the pyroelectric effect.
Thermoelectric energy harvesters are based on the Seebeck effect. Thermocouples composed by junctions alternating n-type and p-type semiconductors are subjected to different temperatures. Usually, in order to maximise the output voltage, the junction pairs are connected electrically in series and thermally in parallel, see Fig. 2.4. These kinds of transducers, called thermopiles, generate a voltage proportional to the temperature difference between the hot and the cold side, the number of thermocouples and a Seebeck coefficient.
At present, the application of thermoelectric energy harvesters is not suitable for mass market. The main limitation is that, typically, only limited temperature differences can be exploited. Considering the thermal gradient between the human body, 37 °C, and a typical environment temperature, 20 °C, the conversion efficiency is very low, about 5.5% [19]. Nevertheless, Lu et al. [28] proposed a prototype which generates up to 150 mW with a temperature difference of 34 °C for buildings application. Kim et al. [29] developed a 500 µm thin, lightweight and flexible wearable thermoelectric generator fabricated on a glass fabric. Exploiting a temperature difference of 15 °C between human skin and a surrounding environment, the proposed device generates a voltage output of 3 mV.

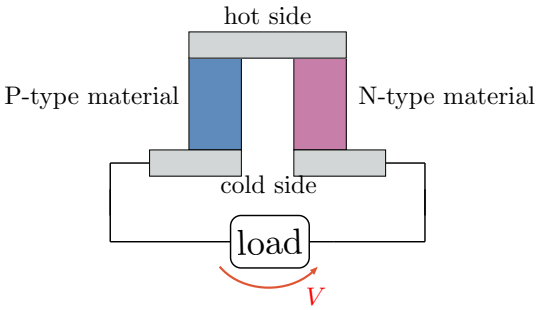

Fig. 2.4 Working principle of a Seebeck based thermal energy harvester.

Other ways to exploit thermal gradient are thermoionic conversion, thermomagnetism, ferroelectricity, and Nerst effect. Anyway the thermoelectric effect is usually the most effective [15].
As alternative to the Seebeck based devices, pyroelectric materials allow converting temperature time fluctuation into electrical charge. Pyroelectric materials are dielectrics with the property of showing spontaneous electrical polarization as function of temperature. It follows that temperature changes cause induced charge variations, thus current [30]. Materials used in pyroelectric devices include piezoelectric materials such as PZT (lead zirconate titanate) and PVDF (polyvinylidene fluoride).

At present, pyroelectricity is used for sensor application in thermal imaging cameras but there is not commercially available energy harvester based on this phenomenon even if several studies are present in literature [30, 31].

2.2.4 Electromagnetic waves energy harvesting

Electromagnetic waves are the result of radiation emitting devices such as radio and TV transmitters, mobile phones, Wi-Fi routers or satellite communications. By means of a properly designed antenna it is possible to collect the energy associated to the electromagnetic radiation converting it into an alternating electric current [15]. Electromagnetic waves energy harvesters are also known as radio frequency energy harvesters.
The amount of the harvested energy depends on the transmitted power, on the gain of the transmitting and of the receiving antenna, and on the distance between source and harvester [32]. However, according to Nishimoto et al. [33], even if the transmitted power is in the order of several kilowatts, the received power will typically be in the order of micro or milliwatts. This drop is mainly due to the transmitted power quadratic decrease with the distance, that causes losses between transmitter and harvester. Losses also occur in the internal circuitry of the harvester leading to a recovered power of 200 µW, 2 m away from a source transmitting a power of 100 mW [34]. Considering normal sources of radiation as standard transmitter or alternate current cables, the harvested power is usually less than 1 µW [19].

As the harvesting from electromagnetic waves already present in the environment may impede or prevent the primary function of the waves themselves, there are no commercial devices for electromagnetic waves energy harvesting.

2.2.5 Chemical energy harvesting

Chemical energy harvesting mainly bases on two energy vectors: enzymatic biofuel-cells (BFC) and salt content in fluids.
Enzymatic BFCs have attracted large interest due to the ability in generating power from the bioelectrocatalytic reaction of common chemicals and metabolites, such as glucose and alcohol, under physiological conditions. In [4], an epidermal BFC is designed and manufactured to generate power from the lactate present in the human skin perspiration during physical activity. Lactate represent a convenient biofuel since it is abundant in human perspiration, can be readily oxidized by commercially available enzymes, and is directly correlate to muscular exertion. For this type of energy harvester, two screen-printed transfer-tattoo electrodes are directly applied on the skin, Fig. 2.5a "U" and "C" shape. Experimental power density ranges from 5 to 70 μWcm^{-2}.

Inspired by the electric eel and the biological systems that have the inherent skill to generate considerable bioelectricity from the salt content in fluids with highly selective ion channels and pumps on cell membranes, [5] proposes an energy harvesting system that converts Gibbs free energy in the form of a salinity gradient into electricity. Through a polyimide membrane 12 µm thick placed between two chambers of a conductivity cell, Fig. 2.5b, a maximum power output of 26 pW is achieved.

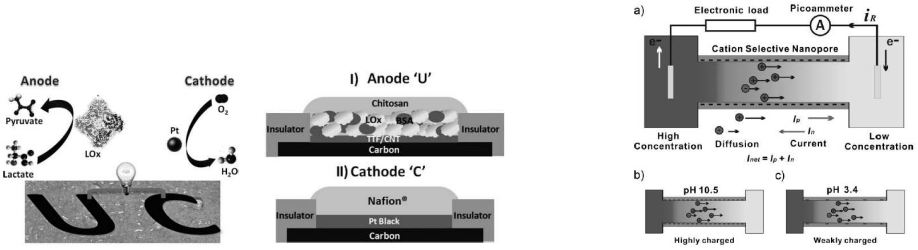

(a) (b)

Fig. 2.5 Chemical energy harvesters working principles. a) Illustration of the epidermal BFC and the constituents of the anode and cathode [4]. b) Ion diffusion across single ion-selective nanopores driven by concentration gradient, schematic illustration of the net diffusion current generation [5].

2.2.6 Kinetic energy harvesting

Kinetic energy is widely present in our environment in the form of vibrations or intermittent motions. Due to its power density, versatility and abundance, kinetic energy is deemed to be the most attractive harvesting source for low-power electronics [22]. This kind of energy source is located in buildings, vibrating machineries, natural environments, human activities and body movements.
The kinetic energy harvesting is the conversion of this mechanical energy into electrical. Usually, the source movement is not significantly influenced neither by the presence of the harvesting device, and neither by the amount of energy extracted. Sometimes the vibrational source is an unwanted side effect which can be usefully damped by the energy harvesting process.
Several approaches have been described in literature. Typically, devices are based on a mass-spring-damper system designed to work at resonance in case of periodic sources, and to exploit the free oscillations of the mass or an imposed kinematic in the case of intermittent sources. In each case, the harvester mass moves excited by the source and its kinetic energy is converted through the following transduction mechanisms [21]:

- *electromagnetic induction*: the motion of the proof mass causes variations of the magnetic flux linked with a coil. Thus, according to Faraday's law, a voltage across the loop itself is generated, Fig. 2.6a;
- *piezoelectricity*: the motion of the proof mass induces mechanical stress in a piezoelectric material generating charge separation and hence electric current in a connected circuit, Fig. 2.6b;
- *electrostatic*: the motion of the proof mass is coupled to the plates of a mechanically variable capacitor. The mechanical vibrations, acting against the electric field, induce charge variations on the plates and, thus, current in a connected circuit, Fig. 2.6c.

Electromechanical transduction in achieved by the exploitation of peculiar proprieties of materials to couple mechanical and electrical behaviour. The involved materials are magnetically induced, electrostatic, electrostrictive or magnetostrictive. Being these proprieties coupled in certain materials, this fact can be exploited to improve harvesting performance as shown in [35].

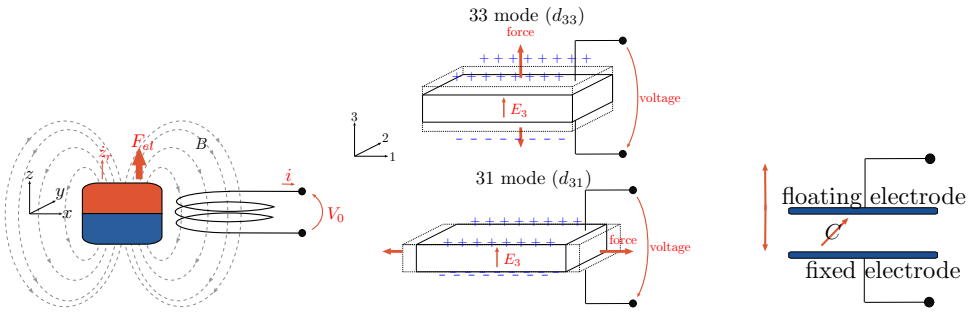

(a) electromagnetic induction (b) piezoelectricity (c) electrostatic

Fig. 2.6 Kinetic energy harvesters working principles.

Most of the transducers can be modelled as an input that causes relative displacement between the proof mass and the frame, so that the mass can produce work against a damping force due to a magnetic or electric field or a piezoelectric material. The work against this damping force is transformed into electric energy. Obviously, in a practical implementation part of the damping is due to friction, plastic deformation, air damping, etc. causing energy losses.

Due to the variable nature of vibrations and movements in terms of frequency and intensity, the resulting AC voltage and current are not suitable for energy storage or direct supply. An electric interface is usually implemented for AC/DC voltage regulation. In addition, different power conditioning techniques have been proposed in order to optimise energy conversion performance, [36–40].

Nowadays, different kinetic energy harvesters are commercially available for both vibrational and both intermittent sources. Leading companies on the market are Perpetuum Ltd. [41], Ferro Solutions Inc. [42] and Mide Volture [43]. Although presenting quite bulky size, commercial energy harvesters power density ranges from 10 to 300 µW/cc relative to acceleration levels of 0.01 - 1 g rms. Several prototypes of harvesters have been successfully demonstrated by universities and private teams. Tornincasa et al. [8] proposed a vibration-powered wireless sensor node for vehicle tires embedding a millimetre-size electromagnetic generator. Beeby et al. [44] implemented a sensor node based on a micro-electromagnetic generator. Roundy et al. [45] developed millimetre-sized electrostatic generators while Peano et al. [46] and Basset et al. [47] successfully built micro-scale electrostatic harvesters. Miao [48] proposed a parametric generator for biomedical applications. Vasic et al. [49]

developed a centimetre-size piezoelectric harvester for bicycle application while example of nano piezoelectric generators is proposed by Zhu et al. [50].

Chapter 3

Kinetic energy harvester modelling

3.1 Introduction

Energy harvesting devices consist of an energy harvesting system (EH) that performs the energy recovery and conversion, and a target electronics that consumes or stores this energy. As anticipated in the previous chapter, kinetic energy harvesting is deemed to be the most attractive technique for low-power electronics due to its energy source power density, versatility and abundance in the environment.

In the following, starting from the description of the energy conversion chain from the mechanical source to the electrical output, the main elements of the kinetic EH are illustrated. A general model valid for both electromagnetic and both piezoelectric technologies is presented and discussed.

3.2 Energy conversion chain

The aim of an EH system is to provide the energy recovered from a mechanical source to an electric load. The mechanical source may assume different forms as vibrations, shocks or intermittent movements which energy have to be extracted by the system. The electrical energy provided to the load, has to be suitable for the electronics supplying or for energy storing. Thus the EH has to perform three main functions: energy extraction, energy conversion and energy transfer/management.

Fig. 3.1 shows a general diagram of the mechanical-to-electrical energy conversion performed by a kinetic energy harvesting system.

In order to describe its behaviour, the EH system can be divided in three main parts as illustrated in Fig. 3.2. The *mechanical part*, often called *energy harvester*, performs energy extraction from the environment. Ambient energy is transferred to a mechanical structure in order to make it available for the conversion. The mechanical structure assumes a very important role acting as a band-pass filter in steady state operation or intermediate mechanical energy storage in impulsive operation. The *transduction mechanism*, or the *transducer*, converts the extracted mechanical energy into electrical energy exploiting a physical phenomenon of electromechanical coupling. The *electrical part*, often called *harvester interface* or *electrical interface*, performs electrical energy management and transfer to the electric load. In its basic configuration, it directly connects transducer and load. Usually, it assumes more complex architectures in order to perform voltage rectification and/or energy conversion maximisation by means of power conditioning techniques.

Although the overall energy flow through the system is from the mechanical (input) to the electrical (output) domain, some considerations are necessary. By means of the transducer, the two domains are coupled. It follows that mechanical energy is transferred toward the electrical domain but, at the same time, electrical energy is transferred backward to the mechanical domain. The backward energy flow does not affect the source as the EH is usually negligible with respect to the source itself. However, it influences the dynamics of the mechanical part of the systems and consequently the amount of energy that can be extracted from the environment. For this reason, in the analysis of the harvesting system and in the design for a specific application, it is not possible to separately consider the two domains. A global model of the EH system, able to take into account all the elements involved in the energy recovery process is needed.

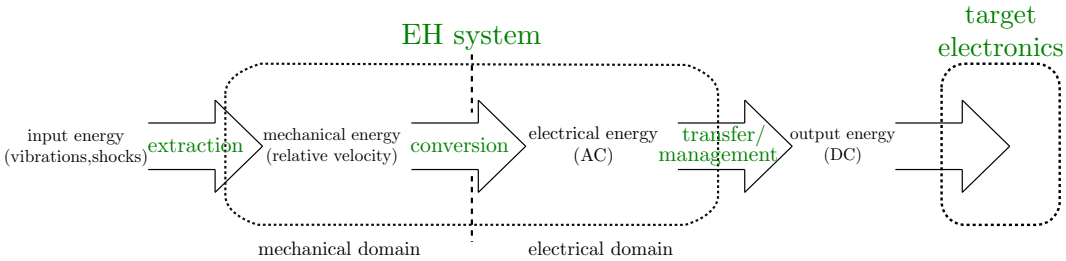

Fig. 3.1 Kinetic EH main energy flows.

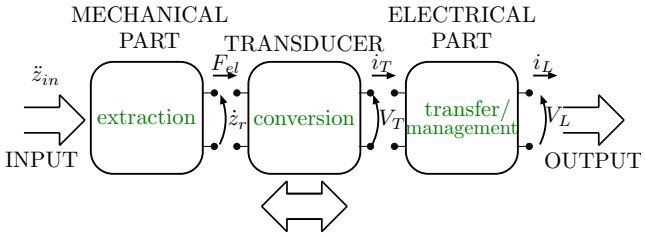

Fig. 3.2 Kinetic EH systems general structure.

In the following the three main parts constituting the EH are analysed separately and then merged together in the global simplified model of Fig. 3.3.

3.3 EH lumped parameters modelling

Mechanical part In kinetic energy harvesting, the energy extraction process consists in transferring the mechanical energy of the source to an inertial mass by exploiting the direct application of a force or making use of the inertial force [14]. Generally, a lumped parameter model consisting of a second order mass-spring-damper single-degree-of-freedom (SDOF) system is considered. This assumption well describes EHs with a single floating mass connected to the host structure by means of a helical spring, as the majority of the electromagnetic energy harvesters. If the connection element is a cantilever beam, as in the majority of the piezoelectric systems where the piezoelectric element is bonded on the beam surface, more detailed models have been established [51]. However, being this system intrinsically relatively poor from the standpoint of the modal density, normally a clear separation between the first bending mode and the other resonance frequencies is present. As the first bending mode provides the most effective electromechanical conversion, the SDOF model is still realistic for the sake of simplicity when the mechanical system is excited around its first resonance frequency or the mass freely oscillates after a shock input [52–54]. Fig. 3.3 shows the basic model of a vibration-based generator independently from the technology exploited for the energy conversion.
Due to its simplicity, reduced computing time and reliability, such an analytical model is very convenient and largely implemented for energy conversion analysis and energy harvester design.

In the considered model, the mechanical system is connected to the transducer by means of an element that influences the dynamics with a force that, as will be shown,

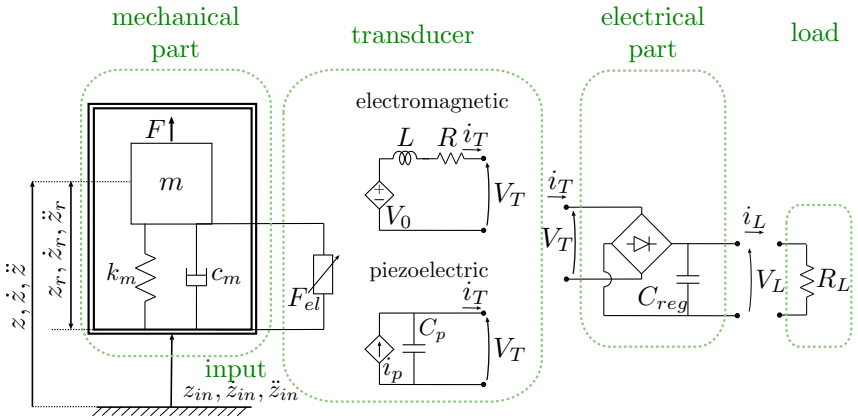

Fig. 3.3 Kinetic EH model.

depends on the state of the electrical part. In the most generic case, when both a direct external force acts on the mass and both a kinematic is imposed to the host structure, the mechanical behaviour of the system can be described by the equation:

$$m\ddot{z} + c_m(\dot{z} - \dot{z}_{in}) + k_m(z - z_{in}) + F_{el} = F(t) \tag{3.1}$$

where dots stand for time-derivatives. $z(t)$, $\dot{z}(t)$, $\ddot{z}(t)$ are the absolute displacement, velocity and acceleration of the floating mass m. $z_{in}(t)$, $\dot{z}_{in}(t)$, $\ddot{z}_{in}(t)$ are the absolute displacement, velocity and acceleration imposed to the host structure. k and c_m are the mechanical stiffness and the parasitic damping of the system, $F(t)$ is the external force directly applied to the mass and $F_{el}(t)$ is the electrical force exerted on the mass due to the transduction mechanism. The equation above can be reformulated introducing the relative displacement z_r given by the difference between the displacement of the floating mass z and the displacement of the frame z_{in}:

$$m\ddot{z}_r + c_m\dot{z}_r + k_m z_r + F_{el} = F(t) - m\ddot{z}_{in} \tag{3.2}$$

Considering a direct force energy harvester, as no kinematic is imposed to the harvester frame, z_{in} and its derivatives are null, and eq. 3.2 becomes:

$$m\ddot{z}_r + c_m\dot{z}_r + k_m z_r + F_{el} = F(t) \tag{3.3}$$

where z and its derivatives are equals to z_r and its derivatives. Considering an inertial force energy harvester, as no external force acts on m, $F(t)$ is null, and eq. 3.2

becomes:

$$m\ddot{z}_r + c_m\dot{z}_r + k_m z_r + F_{el} = -m\ddot{z}_{in} \tag{3.4}$$

It can be noted that the form of eq. 3.3 is very similar to eq. 3.4 where $-m\ddot{z}_{in}$ plays the role of the external force.
As they only need one point of attachment to the vibrating structure, allowing simpler miniaturization and deployment, inertial devices are generally preferred to the direct-force. Thus, only this configuration will be considered in the following.

Electromechanical analogy In the EH design and simulation, it becomes essential to build global models taking into account all the different parts involved. From this standpoint, it is sensible to represents the whole system in the same *language* by constructing an equivalent model where mechanical/electrical components and variables are *translated* into electrical/mechanical components and variables by means of an electromechanical analogy.
The most simplified model is that proposed by Williams and Yates [55]. The transducer and the electrical part are depicted as a dashpot in parallel to the mechanical spring and damper since, due to the conversion of mechanical energy into electrical, they additionally damp the system. It follows that F_{el} can be considered as the force generated by an *electrical damper* that represents the energy conversion/transfer/management/consumption. A mechanical equivalent of the energy harvesting system is built without defining the relation between electrical and mechanical parameters. This very simplifying assumption may be useful to stress out some general considerations about energy conversion performance in terms of energy transferred to the electrical part of the system. Stephen [56] considers purely resistive electric load and proposes a mechanical equivalent model where defines the electrical damping in terms of load resistor and electromechanical coupling in the case of electromagnetic linear EH. This is usefull to distinguish between energy transferred to the electrical part and the amount that can be harvested. However, it makes difficult the representation of the non-linear electric/electronic interfaces employed for power management.
As will be further discussed in the following chapter, in order to increase/optimise recovery performance, non-linear electric/electronic interfaces are employed. Instead of representing diodes and transistors in mechanical terms, it results more convenient to represents the simplified SDOF mechanical part in electrical terms. Possible

electrical equivalents are presented by [57, 38, 58, 59] for both electromagnetic and both piezoelectric EHs. Theoretically it is possible to identify several analogies but the most widely used are the impedance analogy and the mobility analogy.
The analogies are based on the concept of *across* or *effort* variables and *thorough* or *flow* variables. An across/effort variable is a variable determined by measuring the difference of values acting at the two extreme points of an element or in a specific point. A through/flow variable is a variable transmitted through an element without modification or characterising the element itself. The product of the two must be a power.
In the electrical domain, considering an electric component as an element connecting two terminals, the voltage v is the across/effort variable as it is defined as the difference between the potential level of the terminals, while the current i is the through/flow variable as it is *transmitted* from a terminal to the other. The product of current and voltage is the power related to the element, $P_{el} = iv$. In the mechanical domain, power is defined as the product of force F and velocity $\dot{x}$, $P_m = F\dot{x}$. Depending on the standpoint, [60–63], force and velocity can be considered effort or flow variables and thus differently associated to the voltage and the current of the equivalent electric circuit.

If the equivalent electric model associates force to voltage and velocity to current gives the impedance or Maxwell's analogy. This analogy is based on the equivalence of the real part of impedance in the two different energy domains, namely the dissipative behaviour in the two systems is represented in the same way.The mass element is connected to one of the terminals by means of a dotted line as this terminal represents an inertial reference having constant velocity and no acceleration. Fig. 3.4a represent the electrical equivalent of the mechanical part. The two representations present different shape but they are governed by the same equation, eq. 3.4, where the mass m is substituted by an inductor $L = m$, the damper c_m by a resistor $R_m = c_m$, the spring k_m by a capacitor $C = \frac{1}{k_m}$, the inertial force imposed by the kinematics is substituted by a voltage source and the electric force by the voltage at the transducer terminals. As main advantage over the mobility analogy, the impedance analogy maintains the meaning of impedance in the mechanical domain and in its equivalent electrical circuit. As a drawback, it does not maintain the topology of the original system. Elements in parallel in the mechanical system, as the damper and the spring, are connected in series in the equivalent model and vice versa.

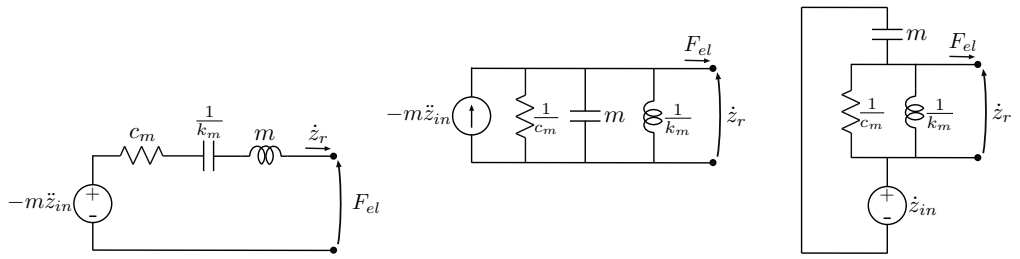

(a) (b)

Fig. 3.4 Equivalent circuit of inertial generator: a) impedance analogy and b) mobility analogy.

If the analogy associates force to current and velocity to voltage gives the mobility or Firestone's analogy. Differently from the impedance analogy standpoint, in this representation the force is transmitted through the element while the velocity of the element is given by the difference between the velocity of the points that it connects. It follows that force is the through variable while velocity the across variable of the equivalent electrical system.Fig. 3.4b represent the electrical equivalent of the mechanical part. In this analogy, the topology of the mechanical system is conserved by the electrical circuit, so for example to the spring and the damper in parallel correspond an inductor and a resistor in parallel. The two systems are governed by the same equation, eq. 3.4, where the mass m is substituted by a grounded capacitor $C = m$, the damper c by a resistor $R = \frac{1}{c_m}$, the spring k_m by an inductor $L = \frac{1}{k_m}$, the inertial force imposed by the kinematics is substituted by a current source and the electric force by the transducer terminals. The system can be reshaped considering as source the kinematic imposed to the structure. In this representation the source of the equivalent circuit is a voltage generator. As main advantage of this analogy over the impedance one, the topology of the mechanical system is preserved by the equivalent electrical circuit. This aspect may be useful in constructing the equivalent of more complex systems or when additional components have to be added to an existing model. As a drawback, being the mechanical impedance represented as electrical admittance, mechanical dissipation is represented as electrical conductance.

Electrical part The electrical part of the EH system consists in the circuit that connects the transducer to the electric load. As the AC voltage and current induced by the transducer are neither suitable for electronics supply nor for energy storage,

power processing steps are necessary [57]. Usually, the output current of the transducer is rectified by means of an AC/DC converter, subsequently a DC/DC converter regulates voltage to make it compliant to the electric load requirements. A simplified but common view consists in considering a linear circuit by replacing the extraction circuit with an equivalent linear impedance. A resistor is connected to the generator, recovery performance depends on its value and, thus, it is adapted to maximise power harvesting. This case, called *classical extraction circuit*, represents the maximum amount of energy that can be recovered with the EH device [38].
Through the implementation of power management strategies, it is possible to act on the electromechanical coupling of the system in order to influence the energy conversion performance. Several techniques have been proposed, [64, 37, 65–68]. Their implementation in the interface circuit is specific for each transducer technology and is presented in the dedicated sections.

Transducer The transducer is the coupling element between the mechanical and the electrical domains. It performs the energy conversion by establishing a relation between force and velocity at the mechanical side, and voltage and currents at electrical one. Converting relations are strictly connected to the nature of the transducer in terms of the exploited phenomenon, transducer topology and operating conditions.
The transducer can be modelled as a transformer: the primary circuit is connected to the mechanical part, while the secondary to the electrical. Depending on the phenomenon involved and on the topology of the device, different relations between the mechanical and electrical variables can be derived for the forward and reverse conversion. The relations here anticipated, are discussed in details in the dedicated sections.
In electromagnetic energy harvesters, a magnet moves with respect to an induction coil. Usually, the forward effect relates the voltage generated at the secondary with the velocity at the primary, while the reverse effect relates the current at the secondary with the force at the primary, Fig. 3.3:

$$V_0 = -\lambda' \dot{z}_r \tag{3.5}$$

$$F_{el} = \lambda' i_T \tag{3.6}$$

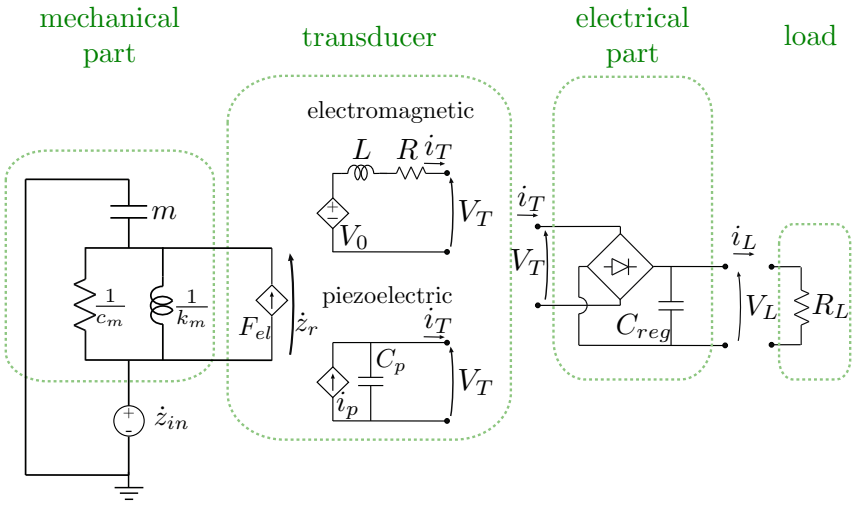

Fig. 3.5 Electrical equivalent kinetic EH model.

where λ' is the derivative of the magnetic flux linkage with respect to the relative displacement, V_0 is the induced voltage and i_T is the transducer current. R and L are the resistance and the inductance of the transducer coil.

In piezoelectric case energy harvesters, a piezoelectric patch bonded on a cantilever beam is deformed. The forward effect is described as a current at the secondary due to the velocity at the primary, while the reverse effect as a force at the primary due to the voltage at the secondary, Fig. 3.3:

$$i_p = -\beta \dot{z}_r \tag{3.7}$$

$$F_{el} = -\alpha V_T \tag{3.8}$$

where i_p is the induced current and α and β are two transduction coefficients that take into account the generalised coupling factor of the piezoelectric patch and the geometry of the EH system.

Electrical equivalent kinetic EH model Fig. 3.5 shows the global lumped parameter model describing the behaviour of the EH system under the application of a kinematic input to the host structure. Mobility analogy is considered for the representation of the mechanical part. The electrical part consists in a rectifier circuit. Other configurations will be presented in the sections dedicated to piezoelectric and electromagnetic technologies. The presented model is translated in Matlab and Simulink environment to build a block-oriented parametric simulation model. Each

element of the device is represented as a *box* containing its mathematical description. The characteristics are determined by geometry and material proprieties, and the behaviour depends on the interactions with the other components.

3.4 Energy conversion considerations

Williams and Yates [55] firstly proposed a basic model for electromagnetic vibrational energy harvesters. They considered the dissipative effect of the energy conversion as a damping effect, thus modelling F_{el} as an electrical damping force proportional to the relative velocity between the mass and the frame:

$$F_{el} = c_{el}\dot{z}_r \tag{3.9}$$

where c_{el} is an equivalent electrical damping.
In this simple model, the combination of mechanical and electrical damping is treated as equivalent linear viscous damping:

$$c = c_m + c_{el} \tag{3.10}$$

Although this approximation is a fair representation of the electromagnetic conversion when a pure resistive electric load is connected, it is quite poor for the piezoelectric. Moreover it does not take into account the effect of complex electric circuit coupled to the mechanical system. Nevertheless, many interesting conclusions about energy conversion may be drawn from the analysis of this simple model.Conclusions, extensively motivated and illustrated in [56], especially concern the maximum amount of power that can be extracted by the mechanical source and the maximum amount that can be transferred to the electrical domain.

Considering eq.s 3.9 and 3.10, eq. 3.1 becomes:

$$m\ddot{z} + c(\dot{z} - \dot{z}_{in}) + k_m(z - z_{in}) = 0 \tag{3.11}$$

that multiplied by $\dot{z}$ and re-arranged gives the expression of the conservation of power:

$$k(z_{in} - z)\dot{z}_{in} + c(\dot{z}_{in} - \dot{z})\dot{z}_{in} = c(\dot{z} - \dot{z}_{in})^2 + \frac{\mathrm{d}}{\mathrm{d}t}\left(\frac{m\dot{z}^2}{2} + \frac{k_m(z - z_{in})^2}{2}\right) \tag{3.12}$$

The instantaneous power flowing into the system, left side, is equal to the power absorbed by the damper, dissipated or harvested, plus the time rate of change of the sum of the kinetic and strain energies, right side. If no damping is present, $c = 0$, the whole power goes towards the build-up of the energy of the system, the oscillation amplitude increases and no steady-state is achieved. This consideration is important to avoid considering possible ``no-damping'' scenarios from the results obtained for steady-state conditions.
In real applications, damping is always present. As shown by eq. 3.12, mechanical and electrical contributions of damping, participate both in energy transfer from the environment to the system and both to it dissipation/harvesting. It follows that the mechanical contribution c_m plays a beneficial and a dissipative role. In [56], it is shown that the energy per cycle contributed by the damper can be both positive, negative or zero, and that the mechanical component cannot contribute more energy than it dissipates.

For harmonic base excitation $z_{in} = Z_{in}\sin(\omega t)$ and introducing the relative displacement z_r, eq. 3.11 becomes:

$$m\ddot{z}_r + c\dot{z}_r + k_m z_r = m\omega^2 Z_{in}\sin(\omega t) \tag{3.13}$$

whose steady-state solution is:

$$z_r = Z_r\sin(\omega t - \varphi) \tag{3.14}$$

where Z_r and φ are the relative displacement amplitude and the phase angle:

$$Z_r = \frac{m\omega^2 Z_{in}}{\sqrt{(k_m - \omega^2 m)^2 + c^2\omega^2}} \tag{3.15}$$

$$\varphi = \tan^{-1}\left(\frac{c\omega}{(k_m - \omega^2 m)}\right) \tag{3.16}$$

Maximum power extracted from the input The average power in terms of relative displacement amplitude of the mass is:

$$P = \frac{1}{2}c\omega^2 {Z_r}^2 \tag{3.17}$$

Substituting eq. 3.15 and considering $\omega = \omega_n = \sqrt{k_m/m}$, the maximum power is given by:

$$P\big|_{\omega=\omega_n} = \frac{{\omega_n}^4 m^2 Z_{in}^2}{2c_m} = \frac{{\omega_n}^3 m Z_{in}^2}{4\zeta} \tag{3.18}$$

where ζ is the damping ratio of the system:

$$\zeta = \zeta_m + \zeta_{el} = \frac{c}{2m\omega_n} \quad \zeta_m = \frac{c_m}{2m\omega_n}; \quad \zeta_{el} = \frac{c_{el}}{2m\omega_n}; \tag{3.19}$$

It might be tempting but quite wrong to deduce that the power increases towards infinity as the damping ratio decreases toward zero. This equation, in fact, gives the power in steady-state condition, situation that would never be reached if $\zeta \to 0$.

Limited stroke implications As a practical device is constrained by a maximum relative displacement of the floating mass Z_{rmax}, it is useful to express in these terms the power flowing from the environment to the device and its value for $\omega = \omega_n$:

$$P_{extr} = \frac{c\, m\omega^4 Z_{in} Z_{rmax}}{2\sqrt{(k-\omega^2 m)^2 + c^2\omega^2}} \tag{3.20}$$

$$P_{extr}\big|_{\omega=\omega_n} = \frac{{\omega_n}^3 m Z_{in} Z_{rmax}}{2} \tag{3.21}$$

Several observation may be drawn. It is worth emphasising that these observations pertain to the flow of energy from the environment into the device, and not the power delivered to an electrical load. In fact, eq. 3.21 refers to the average power dissipated by the mechanical damping or transferred to the electrical domain.
In order to obtain the maximum power flow, the energy harvester should be designed matching its natural frequency with the excitation frequency. In this condition, the average power flow into the device is independent of the damping ratio, eq. 3.21. Obvious consideration is that the excitation amplitude Z_{in} should be as large as possible. Being this a characteristic of the source, this is not a parameter on which to act, but a criterion for the input choice. Also the available stroke of the seismic mass within the device and the mass itself should be as large as possible. Clearly, these could be conflicting parameters.
In designing device or in tuning an existing one against variable input, it might be useful to be able to vary/control the damping c. This ability allows setting the

dynamics of the system according to the magnitude of the input, letting Z_r approach the maximum allowed Z_{rmax}. If Z_{in} is small, then the damping should be small as well to permit to Z_r to be as similar as possible to Z_{rmax}. The power extracted will be small due to the little input, but maximised due the optimal exploitation of the stroke. If Z_{in} is large, then the damping should be large as well so that Z_r does not exceed Z_{rmax}. If Z_r exceeds Z_{rmax}, more power will be dissipated in the impacts of the mass against the mechanical stopper. By increasing damping, the system response bandwidth is broadened and the resulting harvester is less sensitive to the input frequency variations. In the case of low input, the response broadening through c increment causes heavy decrease in power recovery. This two conflicting effects have to be considered together.

Maximum power delivered to the electrical domain Considering eq. 3.19, the maximum average power delivered to the electrical domain through the transduction mechanism is:

$$P_{el}\big|_{\omega=\omega_n} = \frac{\zeta_{el}\omega_n{}^3 m Z_{in}^2}{4(\zeta_m+\zeta_{el})^2} = \frac{2c_m c_{el}}{(c_m+c_{el})^2}P_{extr} \leq \frac{1}{2}P_{extr} \tag{3.22}$$

that is maximised by matching the mechanical and electrical loads, $\zeta_m = \zeta_{el}$. This conclusion, given by $\mathrm{d}P_{el}/\mathrm{d}\zeta_{el} = 0$, is valid as the electrical and mechanical damping ratios are independent.
The amount of power delivered to the electric load will be discussed in the specific sections dedicated to the electromagnetic and piezoelectric energy harvesting.

Chapter 4

Electromagnetic and piezoelectric energy harvesters modelling

4.1 Introduction

Nowadays, electromagnetic and piezoelectric transduction are largely used in numerous applications.
Rotating generators exploiting electromagnetic conversion are widely applied in many fields, from large-scale power generators to bicycle dynamos or Seiko kinetic watches [6]. In the field of energy harvesting, large interest is focused in linear transducers to harvest power from vibrations. These generators, if well-designed and not constrained in size, can be extremely efficient in converting mechanical energy into electrical exploiting the Faraday's law of electromagnetic induction. In this work, this type of kinetic EH is considered.
Piezoelectric conversion is a well established technology to convert mechanical energy into electrical and vice versa. Piezoelectric materials are widely employed in commercial sensors and actuators and represent a promising way in the kinetic energy harvesting field. Piezoelectric proprieties derive from dipole structure of such materials. When subject to a mechanical force, the material becomes electrically polarised. This phenomenon is called *piezoelectric direct effect* and the polarisation level is proportional to the mechanical strain induced by the applied force. Conversely, the inverse phenomenon called *piezoelectric reverse effect*, consists in the deformation of the material due to the dipoles rotation when an electric field is

applied. Typical piezoelectric materials are crystal materials such as quartz, ceramics such as lead zirconate titanate (PZT), thin-film materials such as sputtered zinc oxide and polymer materials such as polyvinylidene fluoride (PVDF). The piezoelectric characteristics of these material are strongly anisotropic. Thus, they depends on the direction of the applied/resulting mechanical strain and on the direction of the resulting/applied polarisation. In addition, the piezoelectric proprieties are typically sensible to temperature and stress levels, and decay with age.

In the following sections, electromechanical and piezoelectric energy harvester modelling is discussed.

4.2 Electromagnetic energy harvester modelling

4.2.1 Electromagnetic effect

The transduction phenomenon at the base of the working principles of the electromagnetic generators is the electromagnetic induction. According to Faraday's law, when an electric conductor moves through a magnetic field, a potential difference, or an electromotive force, is induced between the ends of the conductor itself. The resulting voltage induced in a circuit, V_0, is proportional to the time rate of change of the magnetic flux Φ of that circuit [69].

$$V_0 = -\frac{\mathrm{d}\Phi}{\mathrm{d}t} \tag{4.1}$$

In the majority of practical implementations, the conductor is a multi-turn coil. A permanent magnet creates the magnetic field which flux in the i-th turn can be computed as:

$$\frac{\mathrm{d}\Phi_i}{\mathrm{d}t} = \int_{A_i} \frac{\mathrm{d}B}{\mathrm{d}t} \sin\varphi \, \mathrm{d}A \tag{4.2}$$

where B is the magnetic flux density, A_i is the area of the i-th turn and φ is the angle between the coil and the magnetic flux direction.
The voltage generated in a coil of N turns is given by:

$$V_0 = -N\frac{\mathrm{d}\Phi_{av}}{\mathrm{d}t} \tag{4.3}$$

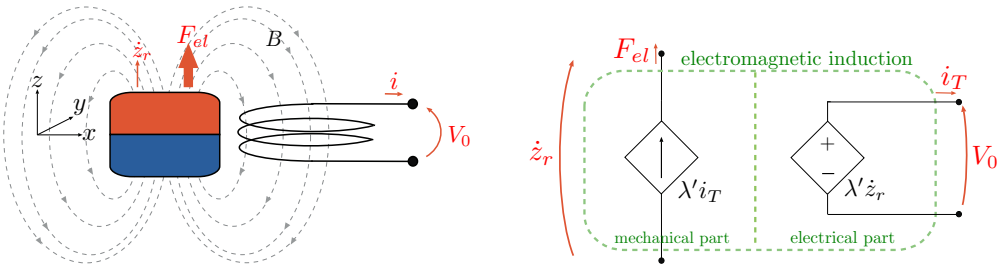

(a) (b)

Fig. 4.1 a) Electromagnetic induction principle and b) schematic model.

where Φ_{av} is the average flux per turn.
If the permanent magnet linearly moves with respect to the coil, for example along the z-direction, see Fig. 4.1a, V_0 can be expressed as the product of the flux linkage gradient with respect to z direction, λ', and the relative velocity between magnet and coil, $\dot{z}_r$:

$$V_0 = -N\frac{\mathrm{d}\Phi_{av}}{\mathrm{d}z}\frac{\mathrm{d}z}{\mathrm{d}t} = -\lambda'\dot{z}_r \tag{4.4}$$

The current resulting in the coil crates its own magnetic field that opposes the field that has given rise to it. It follows an electromagnetic force, F_{el}, that opposes the generator motion. From the power balance between the mechanical and the electrical side, F_{el} is derived:

$$F_{el}\dot{z}_r = V_0 i = \lambda'\dot{z}_r i \quad \Rightarrow \quad F_{el} = \lambda' i \tag{4.5}$$

$$\tag{4.6}$$

4.2.2 Generator modelling (mechanical part and transducer)

The energy harvesting system considered in the following consists of an electromagnetic linear generator which layout is shown in Fig. 4.2a. Although very simple in layout, this solution provides high power density performance and thus, results convenient for kinetic EH applications [22, 70]. A permanent magnet is suspended on a spring and it can oscillate along the vertical direction z. The spring is connected to the case of the device. An induction coil is in-built in the structure of the EH

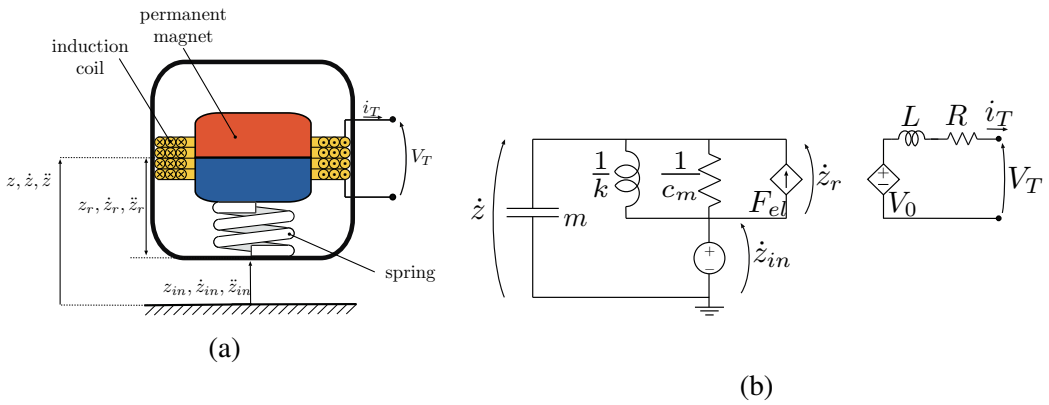

Fig. 4.2 a) Electromagnetic EH scheme and b) electrical equivalent circuit.

and wound along z. When a mechanical input is applied to the structure of the EH, inertial force acts on the floating magnet producing relative motion with respect to the coil. This causes variation of the flux linkage in the coil and, thus, induces voltage. If the transducer is connected to an electric load, current is generated. As a feedback, a force proportional to the current flowing in the transducer acts on the magnets opposing its motion. It is by acting against this force that mechanical energy is transformed into electrical energy.

The electromagnetic energy harvesting system, mechanical part and transducer, can be modelled as shown in Fig. 4.2b.
The governing equations of the system are:

$$\begin{cases} m\ddot{z}_r + c_m\dot{z}_r + k_m z_r + F_{el} = -m\ddot{z}_{in} \\ V_T = V_0 - Ri_T - L\frac{\mathrm{d}i_T}{\mathrm{d}t} \\ F_{el} = \lambda' i_T \\ V_0 = \lambda'\dot{z}_r \end{cases} \tag{4.7}$$

where z_r refers to the relative displacement between the floating magnet and the coil, $\ddot{z}_{in}$ is the acceleration profile imposed to the structure of the device, F_{el} is the force due to the current flowing into the coil, and V_0 is the voltage induced due to $\dot{z}_r$. m is the mass of the floating magnet, k_m is the stiffness of the spring, c_m is the mechanical damping coefficient, λ' is the derivative of the magnetic flux linkage with respect to the relative displacement, R and L are respectively the internal resistance and inductance of the coil.

Power considerations By multiplying the first of eq. 4.7 by $\dot{z}_r$ and the second by i_T, the power balance of the mechanical part and electrical side is derived:

$$\underbrace{-m\ddot{z}_{in}\dot{z}_r}_{input} = \underbrace{m\ddot{z}_r\dot{z}_r}_{kinetic} + \underbrace{c_m\dot{z}_r^2}_{damping} + \underbrace{k_m\dot{z}_r z_r}_{elastic} + \underbrace{\lambda' i_T\dot{z}_r}_{electromagnetic} \tag{4.8}$$

$$\underbrace{V_T i_T}_{output} = \underbrace{\lambda' i_T\dot{z}_r}_{converted} - \underbrace{Ri_T^2}_{coil\,losses} - \underbrace{\frac{1}{2}L\dot{i}_T i_T}_{inductance} \tag{4.9}$$

The power extracted from the mechanical source and injected in the harvester, consists of the kinetic term related to the floating magnet, the elastic term due to the mechanical spring, the power wasted through the mechanical damper and the power delivered to the electric part of the system through the electromagnetic conversion. The output electric power outgoing the generator is the power converted minus the power in the coil inductance and the power dissipated through its internal resistance.

Characteristic parameters Considering open and short-circuit conditions of the generator terminals of Fig. 4.2b, two different resonance frequencies exist.
In OC i_T is null, thus no energy is transferred to the electric domain. The stiffness of the system depends only on the mechanical proprieties:

$$k_{OC} = k_m \tag{4.10}$$

$$\omega_{OC} = \sqrt{\frac{k_{OC}}{m}} \tag{4.11}$$

Conversely, neglecting resistive losses, in SC it is possible to define a short-circuit stiffness k_{SC} that takes into account the conservative behaviour of the coil inductance:

$$k_{SC} = k_{OC} + \frac{\lambda'}{L} > k_m \tag{4.12}$$

where the electric stiffness k_{el} is defined as:

$$k_{el} = \frac{\lambda'}{L} \tag{4.13}$$

As a consequence, the two configurations present two distinct resonance frequencies ω_{OC} and ω_{SC}:

$$\omega_{SC} = \sqrt{\frac{k_{SC}}{m}} = \omega_{OC}\sqrt{1 + \frac{\lambda'}{k_{OC}L}} \tag{4.14}$$

The following dimensionless coefficients can be introduced in order to describe the system. The effectiveness of the electromechanical conversion performed by the generator is described by means of two coupling coefficients k^2 and k^2_{mod}. The electromechanical coupling factor k^2 is defined as the ratio between the SC electromagnetic energy stored in the coil and the overall energy of the system in the

assumption of steady state condition and no resistive losses. The modified electromechanical coupling coefficient k^2_{mod} is defined as the ratio between the electromagnetic energy stored in the coil and the elastic energy in the generator.

$$k^2 = \frac{Li_T^2}{k_{SC}z_r^2} = \frac{\lambda'^2}{k_{SC}L} = \frac{\omega_{SC}^2 - \omega_{OC}^2}{\omega_{SC}^2} \tag{4.15}$$

$$k^2_{mod} = \frac{Li_T^2}{k_{OC}z_r^2} = \frac{\lambda'^2}{k_{OC}L} = \frac{k^2}{1-k^2} \tag{4.16}$$

It is worth noting that $k^2 = 1$ means that all the mechanical energy entering the system is converted into electromagnetic energy. If k^2 tends to 1 then k^2_{mod} tends to infinity while if the system is weakly coupled the two coefficients assume similar values.

The resistive losses coefficient ξ_e represents the resistive losses within the coil induced during the electro-mechanical conversion.

$$\xi_e = \frac{R}{2\omega_{OC}L} \tag{4.17}$$

Usually, the inductance of the coil is negligible with respect to its resistance and thus generator electrical losses represent a critical aspect in energy recovery performance.

The mechanical quality factor Q_m represents the ability of the system in making the input energy available for recovery purposes. It is defined as the ratio of the mechanical energy stored to the dissipated and, thus, it reflects the effective energy available. At low loss damping it is defined as: [71]:

$$Q_m = \frac{\sqrt{k_{OC}\,m}}{c_m} = \frac{1}{2\zeta_m} \tag{4.18}$$

The product of the electromechanical coupling factor and the mechanical quality factor expresses the global electromechanical coupling figure of merit of the system k^2Q_m.

4.2.3 Circuit topologies for performance maximisation

In the EH model, the electric load is represented by its equivalent impedance. A resistor R_L is thus connected to the system and the harvested power is defined as the

power that it dissipates. The dimensionless load coefficient ξ_c can be defined as:

$$\xi_c = \frac{R_L}{2L\omega_{OC}} \tag{4.19}$$

As the electric energy provided by the generator is not suitable for electronics supply, an electric interface is interposed between the transducer and the load. The main task is to rectify the generator output. Several techniques for power managing have been proposed.

STD technique The most elementary circuit to perform rectification is the *standard technique* (STD), Fig. 4.3. Transducer output is rectified through a full-wave diode bridge and filtered by a regulation capacitor C_{reg}.

From eq. 4.7, neglecting bridge electrical losses and non-linearities induced to the displacement, the expression of power is derived with respect to the dimensionless characteristic parameters when a sinusoidal input of amplitude Z_{in} excites the system at its resonance frequency ω_{OC} [38, 72]:

$$P = \frac{k^2 Q_m \xi_c [1 + (\xi_e + \xi_c)^2]}{[1 + 4(\xi_e + \xi_c)^2 + 2k^2 Q_m (\xi_e + \xi_c)]^2} m Q_m \omega_{OC}^3 Z_{in}^2 \tag{4.20}$$

P depends on the electrical load represented as ξ_c and tends towards a limit value which is a function of the mass, the input, the quality factor Q_m and the resonance frequency:

$$P_{lim} = \frac{m\omega_{OC}^4 Z_{in}^2 Q_m}{8\omega_{OC}} = \frac{m^2 \omega_{OC}^4 Z_{in}^2}{8c_m} \tag{4.21}$$

If $\xi_e = 0$, two maxima of P exist for two different values of R_L. However this represents the unrealistic case of no losses in the electrical domain. Real cases imply losses due to coil resistance and thus $\xi_e > 0$. In this condition there is only one optimal resistive load depending on the coupling coefficient value if $k^2 Q_m \leq 2$:

$$\begin{cases} R_{opt\,STD} = L\omega_{OC} \\ P_{max\,STD} = \frac{k^2 Q_m}{(2+k^2 Q_m)^2} \frac{m^2 \omega_{OC}^4 Z_{in}^2}{c_m} \end{cases} \tag{4.22}$$

If $k^2 Q_m > 2$, power is maximised for two values of R_L:

$$\begin{cases} R_{opt\,STD} = \frac{L\omega_{OC}(k^2 Q_m \pm \sqrt{(k^2 Q_m)^2 - 4})}{4} \\ P_{max\,STD} = \frac{m^2 \omega_{OC}^4 Z_{in}^2}{8 c_m} \end{cases} \tag{4.23}$$

If coil inductance can be neglected as in most cases, power is maximised in the *electrical domain analogue matching* (EDAM) condition described in [56]:

$$\begin{cases} R_{opt\,STD} = R + \frac{\lambda'^2}{c_m} \\ P_{max\,STD} = \frac{\lambda'^2}{(c_m R + \lambda'^2)} \frac{m^2 \omega_{OC}^4 Z_{in}^2}{8 c_m} \end{cases} \tag{4.24}$$

The maximisation of the output power consists in setting the load equivalent resistor R_L equal to the optimal value. The optimal value depends on the electromechanical characteristic of the system.

Optimal load impedance emulation technique The aim of the harvester interface circuit is to provide the basic functionality of rectification and voltage level shifting, while loading the harvester with the optimum impedance, independently of its input and output conditions. In order to perform this function, several architectures have been proposed. One strategy is to implement a HI able to emulate optimal load impedance.

Rao et al. [36] proposed a self-powered control circuit based on a full-wave rectifier and an active diode that exploits pulse frequency modulation (PFM) fot the regulation of a boost converter. The system achieves an efficiency up to the 60% of the maximum recoverable power on a resistive load considering a sinusoidal input.

Szarka et al. [65] propose a fully autonomous power conditioning system with maximum power transfer tracking (MPTT). The system is able to operate the harvester at the maximum power point against varying excitation and load condition with an

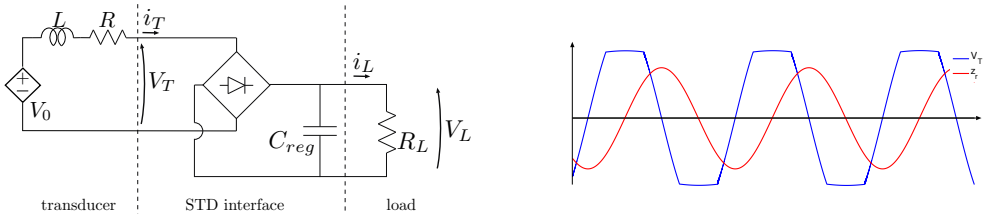

Fig. 4.3 STD technique.

energy transfer efficiency up to 70% of that potentially extractable.
In the present work, a self-powered harvester interface is proposed and developed in sec. 5.4.3. The aim is to perform optimal resistive load emulation while charging an output capacitor independently from the signal provided by the transducer (shape and voltage level) and from the voltage of the storage capacitor. The interface is based on a full wave active boost converter driven by an ultra-low power microcontroller equipped with a transducer current controller for pulse width modulation (PWM). It is implemented to an energy harvesting system designed to work in response to an impulsive input. Details will be discussed in the following.

SMFE technique Arroyo et al. [38] propose the *Synchronous Magnetic Flux Extraction* (SMFE) technique, an easier to implement alternative to the optimum impedance emulation that provides transducer and load decoupling. Based on the *Synchronous Electric Charge Extraction* (SECE) technique for piezoelectric generators (see sec. 4.3.3), SMFE adapts the working principle to the electromagnetic generators. The basic idea is to exploit the coil inductance as intermediate energy storage. Being the electromagnetic transducer inductive, the technique does not require an intermediate level of conversion and, theoretically, energy can be directly transferred from the coil to a storage element.
The induction coil is in short circuit condition most of the time. The energy stored in the coil inductance is proportional to i_T. Each time the induced current reaches an extreme, twice a period, the coil is briefly connected to a storage capacitor to shape an electric oscillator and transfer the energy stored. As the current generated into the electromagnetic transducer is out of phase with respect to the magnet relative displacement, the parameter ϕ defined as the phase angle between a maximum of

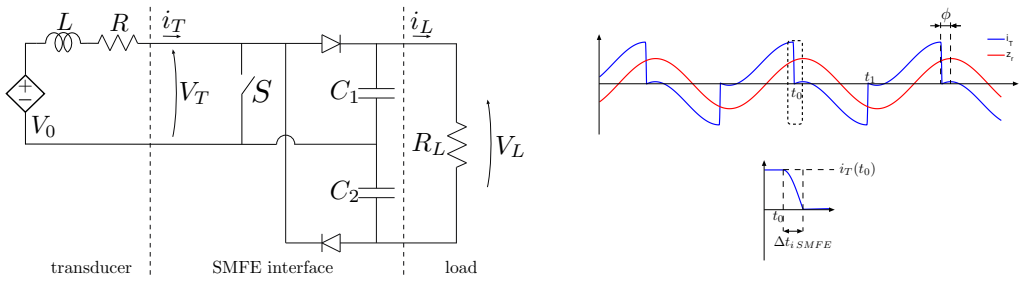

Fig. 4.4 SMFE technique.

displacement and the instant of commutation is introduced. In order to maximise the transferred energy, ϕ has to be tuned to obtain the the commutation at the extreme of the current. In the case of a transducer without resistive losses, i_T is in phase with z_r and thus energy transfer is maximised for $\phi = 0$.
Fig. 4.4 illustrates the architecture and the typical waveform of the SMFE technique. Power conversion is controlled by the switch S that is closed most of the time to short-circuit the transducer. When i_T reaches its maximum, $t = t_0$, S is opened and the energy accumulated into L is transferred to C_1. After a time interval $\Delta t_{iSMFE} = \frac{\pi}{2}\sqrt{LC_1}$, given by half of the period of the electric oscillator, i_T is null and energy transfer completed. S is closed again and the process repeated when the current reaches the minimum in order to charge C_2. Neglecting losses due to diodes voltage drop and switch, the power supplied to the load at resonance is [38]:

$$\begin{cases} P_{SMFE} = \frac{4\pi k^2 Q_m (1+4\xi_e^2)(1+e^{-2\pi\xi_e})^2 \sin^2(\phi+\psi)}{[2k^2 Q_m \sin(\phi+\psi)\cos(\phi+\psi)(1+e^{-2\pi\xi_e})]^2+[\pi(1+4\xi_e^2)+2k^2 Q_m \sin^2(\phi+\psi)(1+e^{-2\pi\xi_e})]^2} \frac{m^2\omega_{OC}^4 Z_{in}^2}{8c_m} \\ \phi = \frac{1}{2}\arctan\left(\frac{4\xi_e}{1-4\xi_e^2}\right) \\ \psi = \arctan\left(\frac{1}{2\xi_e}\right) \end{cases} \tag{4.25}$$

where ψ is a parameter introduced to simplify the expression of P_{SMFE}.

Fig. 4.5 shows the trends of the harvested power in case of STD technique and implementing SMFE as a function of $k^2 Q_m$ and ξ_e. Power is normalised with respect to P_{lim}. Electrical losses due to the HI are neglected.
For $\xi_e > 0.4$ STD technique performance is better than that of SMFE technique independently of the value of $k^2 Q_m$. The same stands for $\xi_e < 0.4$ if $k^2 Q_m > 1.3$. It follows that the SMFE approach is convenient only for low values of $k^2 Q_m$ and ξ_e. By optimising the value of L with an additional inductor, it is possible to make SMFE performance always increasing with $k^2 Q_m$ and comparable to that of the classic approach even for low ξ_e maintaining the gain in case of small $k^2 Q_m$ and ξ_e [38]. However, for high resistive transducers, inductance optimisation result difficult to be carried out.

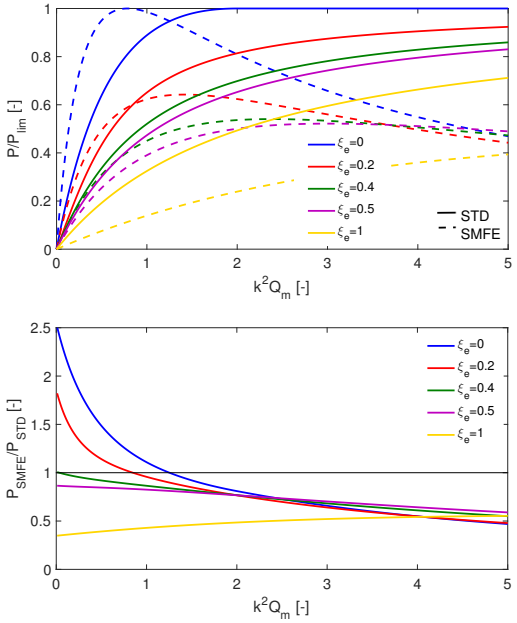

Fig. 4.5 Harvested normalised power implementing STD and SMFE techniques as a function of k^2Q_m and for several ξ_e.

4.3 Piezoelectric energy harvester modelling

4.3.1 Piezoelectric effect

In energy harvesting applications, the piezoelectric effect can be described by using the linear constitutive equations of the piezoelectric materials [71]:

$$\boldsymbol{\delta_p} = \boldsymbol{s^E} \cdot \boldsymbol{\sigma} + \boldsymbol{d}^T \cdot \boldsymbol{E} \tag{4.26}$$

$$\boldsymbol{D} = \boldsymbol{d} \cdot \boldsymbol{\sigma} + \boldsymbol{\varepsilon^\sigma} \cdot \boldsymbol{E} \tag{4.27}$$

where $\boldsymbol{\delta_p}$ is the mechanical strain, $\boldsymbol{\sigma}$ is the mechanical stress, $\boldsymbol{D}$ is the electrical displacement (charge density), $\boldsymbol{E}$ is the electric field, $\boldsymbol{s^E}$ is the compliance under a zero or constant electrical field (indicated by the superscript E) and $\boldsymbol{\varepsilon^\sigma}$ is the dielectric permittivity under a zero or constant stress (indicated by the superscript σ). $\boldsymbol{d}$ and $\boldsymbol{d}^T$ are the matrices for the direct and the reverse piezoelectric effect, where the superscript T means the transposed matrix. Eq.s 4.26 and 4.27 describe respectively the reverse and the direct piezoelectric effect. If the coupling term $\boldsymbol{d}$ is left out, these two equations becomes the uncoupled constitutive equations of an elastic dielectric material. Without the coupling term $\boldsymbol{d}^T \cdot \boldsymbol{E}$, eq. 4.26 is simply Hooke's law relating strain and stress. Likewise, eq. 4.27 is simply the dielectric equation when the coupling term $\boldsymbol{d} \cdot \boldsymbol{\sigma}$ is neglected. [71] reports the detailed matrices notation for a piezoelectric material such as PZT ceramic.

In energy harvesting applications, the piezoelectric material is employed as sensor. Exploiting the direct effect, a mechanical action generates an electrical effect. However, the reverse effect is present and influences the dynamics of the mechanical part of the system. Thus, it cannot be neglected. For a complete description of the system, taking into account the two effects is required.
Due to the anisotropy of the piezoelectric proprieties, a piezoelectric material can be used in different ways. Usually, the electromechanical coupling along two preferred directions is exploited. Typical modes are the 33 and 31 modes illustrated in Fig. 4.6. According to this notation, the first number indicates the voltage direction considered, namely the direction of the electrodes, while the second indicates the direction along which the stress is applied/generated. In both cases, voltage is applied along the 3 direction; this means that in both cases electrodes are attached to the surfaces perpendicular to this axis (upper and bottom surfaces). In 33 mode, *compressive*

mode, stress acts in the same direction as voltage, while in mode 31, *lateral mode*, the stress is applied along a perpendicular direction. For a more complete description, refer to the IEEE standards [73].

In the majority of th energy harvesting applications, the piezoelectric patch is used in the lateral mode although the compressive mode exploits a larger piezoeletric constant ($d_{31} \approx 0.5 d_{33}$ for PZT [74]). In compressive mode, strain is usually very limited while, bonding the piezoelectric patch onto a flexing structure generates larger deformation. This is the common case of a piezoelectric patch bonded on a beam that acts as mechanical spring. Another approach consists in using an interdigital electrode arrangement to exploit both the high lateral strain and both the high 33 coupling property of piezoelectric materials, [6]. Placing the electrodes as shown in Fig. 4.7, allows exploiting the lateral strain as it was a compressive mode strain. The drawback of this configuration is the small active area of the device.

Considering the piezoelectric patch working in the 31 mode shown in Fig. 4.8a, the constitutive eq.s 4.26 and 4.27 can be simplified in one dimension:

$$\delta_1 = s_{11}^E \cdot \sigma_1 + d_{31} \cdot E_3 \tag{4.28}$$

$$D_3 = d_{31} \cdot \sigma_1 + \varepsilon_{33}^\sigma \cdot E_3 \tag{4.29}$$

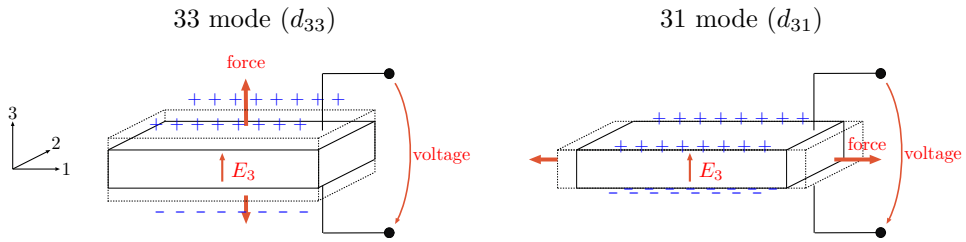

Fig. 4.6 Piezoelectric material in 33 and 31 operating mode. (In blue it is indicated the charge separation within the piezoelectric material)

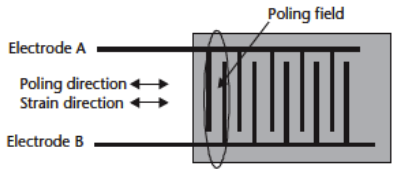

Fig. 4.7 Interdigital electrode arrangement [6].

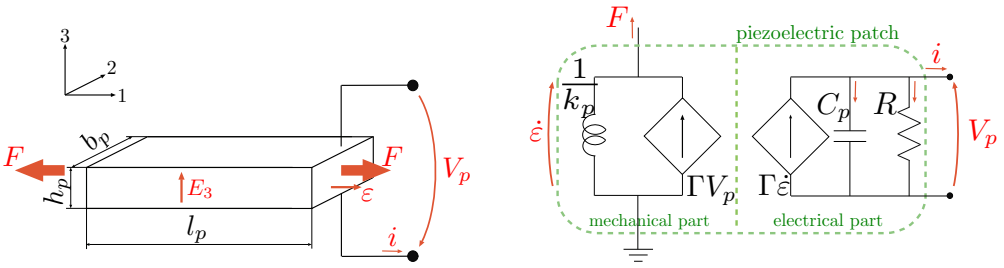

(a) (b)

Fig. 4.8 a) Piezoelectric patch used in the 31 mode and b) schematic model.

When a force F is applied along the 1 direction, it causes the elongation ε along the same direction. Due to the piezoelectric effect, a voltage V_p is generated in the 3 direction and, if a circuit is connected, a current i is induced. Considering the relations of eq. 4.30, it is possible to rewrite eq.s 4.28 and 4.29 in terms of macroscopic variables F, ε, V_p, i. Introducing the parasitic resistance R, dielectric losses are taken into account.

$$E_3 = -\frac{V_p}{h_p}; \qquad q = D_3 b_p l_p; \qquad \sigma_1 = \frac{F}{b_p h_p}; \qquad \delta_1 = \frac{\varepsilon}{l_p}; \qquad i = \frac{\mathrm{d}q}{\mathrm{d}t} \tag{4.30}$$

$$\begin{cases} F = k_p \varepsilon + \Gamma V_p \\ i = \Gamma \dot{\varepsilon} - C_p \dot{V}_p - \frac{V_p}{R} \end{cases} \tag{4.31}$$

where k_p is the axial stiffness of the piezoelectric patch along 1 direction, C_p is the clamped or blocked capacitance of the piezoelement along 3 direction, Γ is the force-voltage factor or the generalized electromechanical coupling factor (GEMC) [75], and they are defined as:

$$k_p = \frac{b_p h_p}{l_p s_{11}^E}; \qquad C_p = \left(\varepsilon_{33}^\sigma - \frac{d_{31}^2}{s_{11}^E}\right)\frac{b_p l_p}{h_p}; \qquad \Gamma = \frac{d_{31} b_p}{s_{11}^E} \tag{4.32}$$

According to eq. 4.31, the force F consists of the axial elastic force $k_p\varepsilon$ that depends only on the mechanical characteristics of the piezoelectric element, and the electromechanical coupling force ΓV_p that is due to the state of the connected electric circuit. The outgoing current of the piezoelectric element i consists of a contribution $\Gamma\dot{\varepsilon}$ due to the mechanical behaviour and related to the time derivative of the elongation along 1 direction, a contribution $C_p V_p$ related to an equivalent capacitance between the electrodes, and a contribution $\frac{V_p}{R}$ due to the dielectric losses. According

to eq.s 4.31, the mechanical part of the piezoelectric patch can be seen as a spring and a controlled force generator in parallel, while the electrical is equivalent to a circuit containing a controlled current source, a capacitor and a resistor in parallel. Usually, R assumes very large value and thus can be considered as an open circuit. Fig. 4.8b shows the schematic model of the piezoelectric patch. Under the same mechanical excitation, the larger Γ is, the more energy is generated in the electrical domain. On Γ also depends the magnitude of the effect that the electrical part has on the mechanical.
As the induced current is proportional to $\dot{\varepsilon}$, thus, considering one end of the patch fixed, it is proportional and in phase with the velocity of the free-end. In open circuit condition $i = 0$ and a certain voltage is generated in the clamped capacitance. Being the voltage in quadrature with respect to the current, the resulting electric force in the mechanical part is in phase with the displacement of the free end of the patch. It follows that the controlled force generator in the mechanical part of the system can be substituted with an equivalent spring. A stiffer system results. If the piezoelectric element is connected to a very low resistive load, the voltage generated at its terminals is in phase with the current induced by the mechanical part. Thus, the controlled force generator in the mechanical part corresponds to an equivalent damper as described by [55, 56]. A damped system results. In the first case all the energy delivered to the electrical side is returned to the mechanical, conversely in the second it is entirely dissipated. In intermediate load conditions, the feedback force generated by the electrical part, due to its phase, presents both conservative and both dissipative behaviour.

The ability of a piezoelectric patch to convert mechanical energy into electrical when used in 31 mode is measured by the *squared piezoelectric material coupling factor* k_{31}^2. According to the IEEE Standards on Piezoelectricity [73], k_{31}^2 exclusively depends on the the piezoelectric material properties and is defined as:

$$k_{31}^2 = \frac{d_{31}^2}{\varepsilon_{33}^{\sigma} s_{11}^{E}} \tag{4.33}$$

The squared coupling factor k_{31}^2 measures the ratio of the electrical (mechanical) energy stored to the amount of the mechanical (electrical) energy applied in the the forward (reverse) piezoelectric effect. Typical values of k_{31} are $\sim$0.3 for piezoceramic materials and $\sim$0.12 for polymer [6]. It is possible to link the material coupling

factor to the GEMC Γ by considering eq. 4.32:

$$k_{31}^2 = \frac{\Gamma^2}{k_p C_P} \tag{4.34}$$

4.3.2 Energy harvester modelling (mechanical part and transducer)

In the following, a simple piezoelectric energy harvester consisting of a piezoelectric patch bonded on a cantilever beam with a tip mass is considered, Fig. 4.9a.
When a mechanical input acts at the joint along the vertical direction, the cantilever beam vibrates. Due to deflection of the free-end, the support beam bends and thus strain is induced to the piezoelectric layer. Being the deflection of the free-end very limited, and being the piezoelectric patch very thin, strain is modelled as traction/compression along the 1 direction of the piezoelectric element. Electrodes are applied along the 3 direction, thus the piezoelectric patch works in 31 mode. Due to mechanical vibrations, AC current is induced for piezoelectric direct effect and, if the transducer terminals are not short-circuited, a voltage is generated. The voltage at the transducer terminals, according to the piezoelectric reverse effect, induces a mechanical stress in the piezoelectric patch along the 1 direction. As a consequence of the shift of the piezoelectric patch with respect to the neutral surface of the support beam, voltage produces a force along the z direction at the free-end of the beam.
When the cantilever beam vibrates at the first mode, the first bending mode, the largest strain is induced in the piezoelectric patch and the more energy is generated in the electric circuit. This operating condition is the more convenient for energy harvesting purposes. Normally, due to the poor modal density of the cantilever beam,

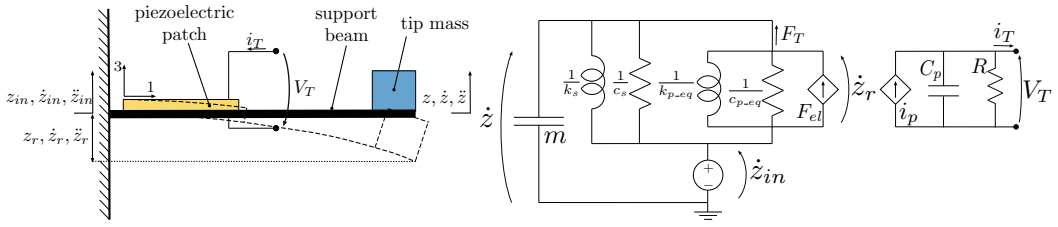

(a) (b)

Fig. 4.9 Piezoelectric EH based on a cantilever beam: a) scheme and b) electrical equivalent circuit.

a clear separation between the first and the following modes is present and the first bending mode well describes the beam behaviour when it is excited around this frequency or the mass freely oscillates after a shock. In this assumption, the energy harvesting system, mechanical part and transducer, can be modelled as shown in Fig. 4.9b.

In the piezoelectric EH modelling, it is worth noting that eq. 4.31 cannot be directly implemented to describe the electromechanical coupling of the system.
The model shown in Fig. 4.9b describes the system illustrated in Fig. 4.9a, and refers to forces, displacements and velocities along the z axis. Eq. 4.31 refers to force, elongation and elongation speed acting along the 1 direction of the piezoelectric patch.
In the EH system, the force F, due to the characteristics of the system produces a force F_T applied to the free-end of the cantilever beam along the z axis. In the same way, the displacement of the free-end along the z axis, due to the characteristics of the system, induces elongation along the 1 direction of the piezoelectric patch and, thus, its velocity induces current.
Therefore, it is necessary to refer the force F and the elongation speed $\dot{\varepsilon}$ of eq. 4.31 to the force F_T and the relative velocity $\dot{z}_r$ acting in the mechanical model by means of two coefficients A and B:

$$F_T = -A\,F \tag{4.35}$$

$$\dot{\varepsilon} = -B\,\dot{z}_r \tag{4.36}$$

defined as:

$$A = \frac{\Delta h}{\left(L - \frac{l_p}{2}\right)} \tag{4.37}$$

$$B = l_p \frac{3\Delta h}{L^3}\left(L - \frac{l_p}{2}\right) \tag{4.38}$$

where Δh is the distance between the piezoelectric patch and support beam neutral surfaces, L is the support beam length, and $A > B$ results. For the details on the calculations of A and B see Appendix A.
Being eq. 4.31 derived from the constitutive equations of the piezoelectric material, a static condition is considered and no mechanical dissipative effect is considered. Even if in the majority of cases it is negligible, at least in the modelling of the

system it has to be considered. Thus, the term $c_p\dot{\varepsilon}$ is added to the expression of F, eq. 4.31, when implemented in eq. 4.39, where c_p is the mechanical damping of the piezoelectric patch.
The coupling equations of the piezoelectric patch used in 31 mode, eq. 4.31, become the equations of the piezoelectric transducer consisting of a the patch bonded on a cantilever beam:

$$\begin{cases} F_T &= -AF = -A(c_p\dot{\varepsilon} + k_p\varepsilon + \Gamma V_T) = c_{p\_eq}\dot{z}_r + k_{p\_eq}z_r - \alpha V_T \\ i_T &= \Gamma\dot{\varepsilon} - C_p\dot{V}_T - \frac{V_T}{R} = -\beta\dot{z}_r - C_p\dot{V}_T - \frac{V_T}{R} \end{cases} \tag{4.39}$$

where F_T is the force acting on the tip mass along z direction due to the piezoelectric patch, k_{p_eq} and c_{p_eq} are the equivalent mechanical stiffness and damping of the piezoelectric patch when its behaviour is referred to the relative displacement of the tip mass. i_T and V_T are the output current and voltage of the transducer. α and β are the electromechanical coupling coefficients of the transducer respectively for the reverse and forward piezoelectric effect. C_p and R are the clamped capacitance and the dielectric loss respectively. Due to the topology of the transducer, the two effects are described by different coefficients as experimentally proven by [58].
The governing equations of the systems are:

$$\begin{cases} m\ddot{z}_r + c_m\dot{z}_r + k_m z_r + F_{el} = -m\ddot{z}_{in} \\ i_T = i_p - C_p\dot{V}_T - \frac{V_T}{R} \\ F_{el} = -\alpha V_T \\ i_p = -\beta\dot{z}_r \end{cases} \tag{4.40}$$

where z_r, $\dot{z}_r$, $\ddot{z}_r$ refer to the relative displacement of the tip mass with respect to the joint, $\ddot{z}_{in}$ is the the acceleration profile imposed to the joint, F_{el} is the force due to the reverse piezoelectric effect, and i_p is the current due to the forward piezoelectric effect.
In modelling the cantilever beam EH, in order to take into account not only the inertia of the tip mass, the moving mass m is given by the sum of the tip mass at the free-end of the cantilever beam m_t and the contribution weighted by θ due to the mass of the support beam m_s and of the piezoelectric patch m_p:

$$m = m_t + \theta(m_s + m_p) \tag{4.41}$$

The overall stiffness of the mechanical system k_m is given by the contribution due to the bending stiffness k_s of the cantilever beam and the contribution due to the bonded piezoelectric patch k_p:

$$k_m = k_s + k_{p\_eq} \tag{4.42}$$

$$k_s = \frac{3E_s I_s}{L^3} \tag{4.43}$$

$$k_{p\_eq} = A\,B\,k_p \tag{4.44}$$

where E_s is the elastic modulus of the cantilever beam and $I_s = \frac{b_s h_s^3}{12}$ is its second moment of inertia.
The overall damping of the mechanical system c_m is given by the sum of the contribution due to the cantilever beam c_s and due to the piezoelectric patch c_p:

$$c_m = c_s + c_{p\_eq} = 2\zeta\sqrt{k_m m} \tag{4.45}$$

$$c_s = 2\zeta_s\sqrt{k_s m} \tag{4.46}$$

$$c_{p\_eq} = 2\zeta_p\sqrt{k_{p\_eq} m} = ABc_p \tag{4.47}$$

$$\zeta = \frac{\zeta_s\sqrt{k_s} + \zeta_p\sqrt{k_{p\_eq}}}{\sqrt{k_m}} \tag{4.48}$$

The clamped capacitance of the piezoelectric patch C_p is calculated as in eq. 4.32, here it is reported for convenience:

$$C_p = \left(\varepsilon_{33}^T - \frac{d_{31}^2}{s_{11}^E}\right)\frac{b_p l_p}{h_p} \tag{4.49}$$

The piezoelectric transduction coefficients α and β relate the generalised coupling factor of the piezoelectric patch to the mechanical proprieties of the EH system:

$$\alpha = A\Gamma \tag{4.50}$$

$$\beta = B\Gamma \tag{4.51}$$

Power considerations By multiplying the first of eq. 4.40 by $\dot{z}_r$ and the second by V_T, the power balance of the mechanical part and of the electrical side is derived:

$$\underbrace{-m\ddot{z}_{in}\dot{z}_r}_{input} = \underbrace{m\ddot{z}_r\dot{z}_r}_{kinetic} + \underbrace{c_m\dot{z}_r^2}_{damping} + \underbrace{k_m\dot{z}_r z_r}_{elastic} + \underbrace{(-\alpha V_T\dot{z}_r)}_{piezoelectric} \tag{4.52}$$

$$\underbrace{V_T i_T}_{output} = \underbrace{(-\beta\dot{z}_r V_T)}_{converted} - \underbrace{C_p\dot{V}_T V_T}_{capacitance} - \underbrace{\frac{V_T^2}{R}}_{piezo\,losses} \tag{4.53}$$

The input power of the system, namely the power extracted from the mechanical source and injected in the harvester, consists of the kinetic power of the floating mass, the elastic power stored in the mechanical spring, the power wasted through the mechanical damper and the overall power delivered to the the electric part of the system through the piezoelectric element. The output power, namely the electric power provided to the electrical part of the system, consists of the converted power from the mechanical domain minus the power stored in the clamped capacitance of the piezoelectric patch and that lost by the dielectric. It is worth noting that the input power of the electrical part, the converted power, is different from the power outgoing the mechanical system due to the piezoelectric coupling. As $\alpha > \beta$, the input power in the electrical part, namely the maximum recoverable, is lower than the power outgoing the mechanical part. An important note about the meaning of the electromechanical coupling coefficients and on the ability of the considered model in describing the power conversion is necessary.

The electromechanical coupling coefficients β and α describe how the transducer relates the mechanical variable $\dot{z}_r$ to the electrical variable i and how the electrical variable V_T is related to the mechanical variable F_{el}. β and α extend the meaning of Γ when a mechanical transformer is interposed between the vibrating system and the transducer piezoelectric patch. In this case the mechanical transformer is represented by the cantilever beam that relates the 1 direction of the piezoelectric patch to the z direction of the vibrating system through the coefficients A and B.

Considering a system represented by a piezoelectric element bonded on a cantilever beam of the same length, and considering the vibration of the free-end along the x direction, the elongation ε of the patch corresponds to the deflection x_r ($\varepsilon = x_r$) and the force F is applied to the free-end ($F_T = F$). Thus, $A = B = 1$ and $\alpha = \beta = \Gamma$. It follows that the power outgoing the mechanical system due to the piezoelectric

coupling, P_{mech_piezo} is equal to the input power of the electrical part, P_{elec_piezo}:

$$P_{mech\_piezo} = P_{elec\_piezo} = \Gamma \dot{z}_r V_p \tag{4.54}$$

Considering the cantilever beam EH system, the relation between the free-end deflection z_r and the elongation of the piezoelectric patch ε is different from the relation between the force applied to the patch along the 1 direction and to the free-end along the z direction. Thus, $A \neq B$ and $\alpha \neq \beta$. It follows that the power outgoing the mechanical system due to the piezoelectric coupling is not equal to the input power of the electrical part. Being $A > B$ and thus $\alpha > \beta$, the first power is larger than the latter.

$$P_{mech\_piezo} = \alpha \dot{z}_r V_p \tag{4.55}$$

$$P_{elec\_piezo} = \beta \dot{z}_r V_p \tag{4.56}$$

$$P_{mech\_piezo} > P_{elec\_piezo} \tag{4.57}$$

Thus the recoverable power at the electrical side is lower than the power extracted by the mechanical system due to the piezoelectric coupling.

Characteristic parameters As for the case of electromagnetic EH, considering open and short-circuit condition of the electric terminals of the transducer, Fig. 4.9b, two different resonance frequencies exist.
In SC, V_T is null, thus from eq.s 4.52 and 4.53 no energy is transferred to the electric load and no electrical feedback force acts to the mechanical part. The resonance frequency of the system depends only on its mechanical properties:

$$k_{SC} = k_m \omega_{SC} = \sqrt{\frac{k_{SC}}{m}} \tag{4.58}$$

In OC, i_T is null and V_T is in phase with z_r. Thus, the controlled force generator acts as a spring k_{el} or, according to the mobility analogy, it can be replaced with an inductor $\frac{C_p}{\alpha\beta}$. It follows a stiffer mechanical system:

$$k_{OC} = \frac{1}{L_{OC}} = k_{SC} + \frac{\alpha\beta}{C_p} > k \tag{4.59}$$

where an electric stiffness is defined as:

$$k_{el} = \frac{\alpha\beta}{C_p} \tag{4.60}$$

Higher resonance frequency results:

$$\omega_{OC} = \sqrt{\frac{k_{OC}}{m}} = \omega_{SC}\sqrt{1+\frac{\alpha\beta}{k_{SC}C_p}} \tag{4.61}$$

It is worth noting that, in both OC and SC condition, the damping effect due to the electric load ($R_L = \infty$ and $R_L = 0$ respectively) is null.

In order to evaluate the electromechanical coupling factor of the energy harvesting system through the piezoelectric patch, it is possible to extend the concept of the squared piezoelectric material coupling factor k_{31}^2 to the *squared electromechanical coupling factor*, k^2. This parameter takes into account not only the properties of the piezoelectric material, but also the mechanical characteristics of the systems. In these terms, for example, a device where the piezoelectric patch is very close to the neutral surface of the support beam may result less coupled than a system where the distance is larger, even if k_{31}^2 is smaller.
The electromechanical coupling factors k^2 and k_{mod}^2, introduced in sec. 4.2.2 for the electromagnetic EH, are defined as:

$$k^2 = \frac{C_p V_T^2}{k_{OC} z_r^2} = \frac{\alpha\beta}{k_{OC}C_p} = \frac{\omega_{OC}^2 - \omega_{SC}^2}{\omega_{OC}^2} \tag{4.62}$$

$$k_{mod}^2 = \frac{C_p V_T^2}{k_{SC} z_r^2} = \frac{\alpha\beta}{k_{SC}C_p} = \frac{k^2}{1-k^2} \tag{4.63}$$

Typical values of k^2 in piezoelectric EH are in the range of $0.01 - 0.1$ [76, 75].

The resistive losses coefficient ξ_e represents the dielectric losses within the piezoelectric layer responsible of the self-discharging:

$$\xi_e = \frac{1}{2R\omega_{SC}} \tag{4.64}$$

Usually, as R tends to be large, this kind of losses are considered only in static condition. In the following section, R will be neglected.

The ability of the system in making the input energy available for recovery purposes is represented by the mechanical quality factor Q_m. This parameters is the ratio of the mechanical energy stored to the energy dissipated and, thus, it reflects the effective available energy. At low loss damping, Q_m is defined as [71]:

$$Q_m = \frac{1}{2\zeta} \tag{4.65}$$

In piezoelectric energy harvesting systems, the product of the effective coupling factor and the mechanical quality factor, $k_{eff}^2 Q_m$, expresses the *global electromechanical coupling figure of merit*.

4.3.3 Circuit topologies for performance maximisation (electrical part)

Usually, piezoelectric energy harvesting systems present poor coupling between the mechanical and electrical domains. The force due to the voltage at the transducer terminals is low and the oscillation amplitude of the tip-mass is due almost exclusively to the mechanical parasitic damping rather than the electrical loading. In this condition, the maximum power that can be dissipated in a linear load resistance R_L or into a circuit with an equivalent input impedance, occurs when [70]:

$$R_L = R_{opt} = \frac{1}{\omega C_p} \tag{4.66}$$

It is evident from eq. 4.66 that the power that can be recovered is limited by the clamped capacitance of the piezoelectric patch.

STD technique In the practical implementation of the EH device, the electric load represented by a resistor R_L, cannot be directly connected to the transducer terminals because a stabilised DC voltage is required.

The most elementary circuit topology to carry out this function, is the so called *standard technique* (STD), Fig. 4.10. The transducer output voltage is rectified with a full-wave diode bridge and filtered using a regulation capacitor C_{reg}.
According to [76], when a sinusoidal vibrational input of amplitude Z_{in} excites the

EH at its resonance frequency ω_{SC}, neglecting the electrical losses due to the voltage drops across the diodes of the bridge rectifier and neglecting the non linearities induced by the electric load to the displacement, the maximum power delivered to the load in weak coupling condition, $k_{eff}^2 Q_m \leq \pi$, occurs at $R_L = R_{opt\,\mathrm{STD}}$:

$$\begin{cases} R_{opt\,\mathrm{STD}} = \dfrac{\pi}{2\omega_{SC} C_p} \\ P_{max\,\mathrm{STD}} = \dfrac{\pi}{2} \dfrac{k_{eff}^2 Q_m}{\left(\pi + k_{eff}^2 Q_m\right)^2} \dfrac{m^2 \omega_{SC}^4 Z_{in}^2}{c_m} \end{cases} \tag{4.67}$$

When high electromechanical coupling is considered, $k_{eff}^2 Q_m > \pi$, the output power is maximised by two different values of $R_{opt\,\mathrm{STD}}$. In this case, the output power represents the maximum power that can be extracted with the standard interface:

$$\begin{cases} R_{opt\,\mathrm{STD}} = \dfrac{2\sqrt{\alpha\beta} - \pi C_p c_m \pm 2\sqrt{\alpha\beta}\sqrt{\alpha\beta - \pi C_p c_m \omega_n}}{2c_m \left(C_p \omega_{SC}\right)^2} \\ P_{lim\,\mathrm{STD}} = \dfrac{m^2 \omega_{SC}^4 Z_{in}^2}{8 c_m} \end{cases} \tag{4.68}$$

The maximisation of the output power consists in setting the load equivalent resistor R_L equal to the optimal value. The optimal resistor value depends on the electromechanical characteristics of the system and on the excitation frequency.

SSHI techniques In order to increase recovery performance, several approaches based on timed switching elements have been proposed [39, 67]. Considering the energy balance of eq.s 4.52 and 4.53, the converted energy is proportional to the work done by the electrical feedback force against the moving mass. In other words, it is proportional to the time integral of the product of the voltage at the transducer terminals and the velocity of the free-end multiplied by the GEMC factor. Hence,

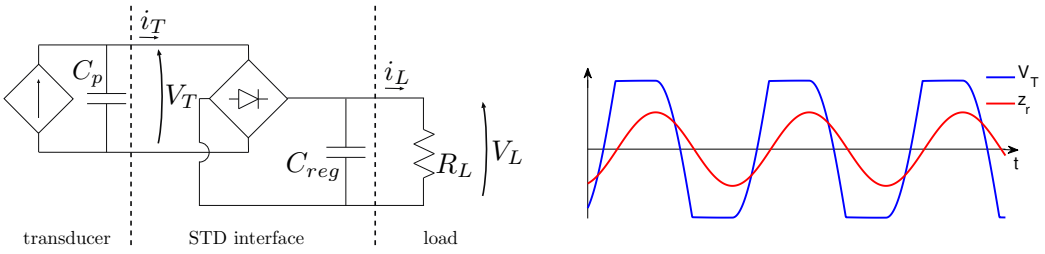

Fig. 4.10 STD technique.

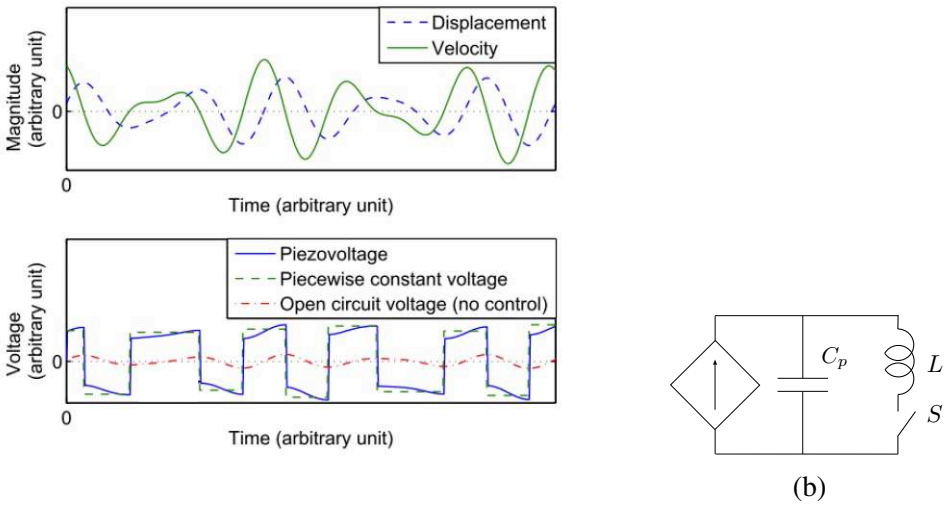

Fig. 4.11 a) Waveforms of the displacement, velocity and piezoelectric voltage V_T induced [7] and b) implementation of the SSHI.

three possible way can be followed in order to increase the energy conversion ability of the system:

- increase the electromechanical coupling term;
- increase the voltage;
- reduce the phase between velocity and voltage.

The first option consists in properly select the piezoelectric material for the application and optimally design the geometrical aspects of the EH system. Thus it is not affected by the electrical circuit connected.
Considering the OC condition, the voltage has the same trend of the displacement. It follows the conservative behaviour depicted before. However, by reversing the voltage at zero speed, namely each time the free-end reaches an extreme of its oscillation, it is possible to align the sign of voltage and speed, producing a damping effect during the whole period. Moreover, this operation ensures a cumulative process that increases the voltage magnitude. Fig. 4.11a shows how the switching approach allows both reducing the time shift between speed and voltage, as well as significantly increasing the voltage level, permitting a conversion magnification up to 20 times [39].

In order to perform the voltage inversion, the transducer is briefly connected to an inductor by means of a digital switch. A resonant electrical circuit is shaped when the switch is closed. The inductor is set to have an electrical resonant period much smaller than the mechanical. It follows that, if the switch is closed for half an electrical period, the voltage inversion occurs almost instantaneously if compared to the dynamics of the mechanical part. Due to the resistive losses into inductor and switch, the voltage inversion is characterised by an inversion coefficient, $0 \leq \gamma \leq 1$, given by the ratio between the voltage after and before the inversion process. This technique for voltage inversion is very low power consuming and it needs only the energy to control the digital switch. Different approaches to make the switch control electrically autonomous can be implemented [77]. Their energy demand is very limited and proven to be typically the 3% of the electrostatic energy available on the piezoelectric material. A negligible value if compared to the power conversion gain.

Among the several non-linear techniques proposed, in this context, only the *series Synchronised Switch Harvesting on Inductor* (s-SSHI) and the *Synchronised Electric Charge Extraction* (SECE) are considered. For an exhaustive description of the various techniques, refer to [39, 67].

s-SSHI technique The simplest architecture consist in connecting the switching element (switch + inductor) in series between the transducer and the diode bridge, Fig. 4.12. The operating principle consist in extracting energy while the transducer voltage inversion occurs. The transducer is always in open-circuit except during the voltage inversion and thus, excepting this time interval, it is an image of the mechanical displacement.
At time t_0, the mechanical displacement reaches the maximum an the transducer voltage V_T too. The switch S is turned on and the voltage inversion through the

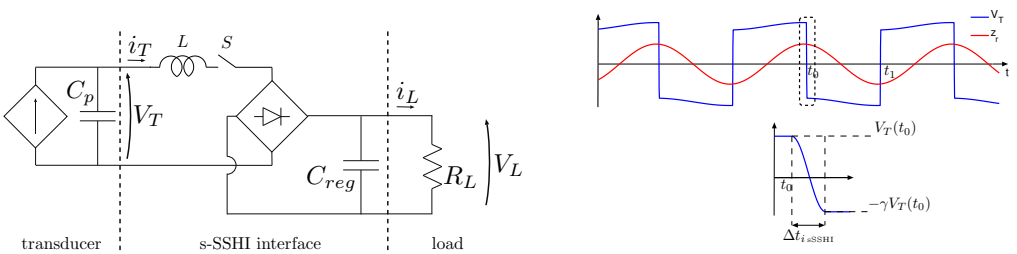

Fig. 4.12 s-SSHI technique.

inductor L begins. The transducer is connected to the load through the bridge and energy extraction is performed. After a time interval given by the duration of half period of the oscillator, $\Delta t_{i\,\text{sSSHI}} = \pi\sqrt{LC_p}$, V_T is opposite in sign, S is opened and the voltage trend is again an image of the displacement. Due to the circuit losses and the energy extraction, $V_T(t_0 + \Delta t_{i\,\text{sSSHI}}) = -\gamma V_T(t_0)$. The displacement decreases and the voltage too, but, being negative due to the inversion, increases its magnitude. When the displacement reaches its minimum, t_1, S is closed again and the inversion/extraction process repeated. Again, the output power P_{sSSHI} is maximised for an optimal value of the load resistor. The optimal load resistance $R_{opt\,\text{sSSHI}}$ is lower than $R_{opt\,\text{STD}}$ but cannot be analytically expressed. It has to be numerically derived from the expression of P_{sSSHI}. The maximum power delivered to the load when $R_L = R_{opt\,\text{sSSHI}}$ is well approximated by the analytical expression [67]:

$$P_{max\,\text{sSSHI}} = \frac{4R_L\alpha\beta(1+\gamma)^2}{(2R_LC_p\omega_{SC}(1+\gamma)+\pi(1-\gamma))^2}\frac{m^2\omega_{SC}^4Z_{in}^2}{\left(c_m+\frac{4\alpha\beta}{C_p\omega_n}\frac{1+\gamma}{2RC_p\omega_{SC}(1+\gamma)+\pi(1-\gamma)}\right)^2} \tag{4.69}$$

$$P_{max\,\text{sSSHI}} \approx \frac{k^2Q_m}{2\pi\frac{1-\gamma}{1+\gamma}+8k_{eff}^2Q_m}\frac{m^2\omega_{SC}^4Z_{in}^2}{c_m} \tag{4.70}$$

Again, power maximisation consists in setting R_L equal to the optimal value.
Using standard electrical components, the gain in terms of harvested power is up to 10 with respect to the STD technique under imposed constant relative displacement magnitude and the effective bandwidth is widened [39]. When vibrational input z_{in} is considered, the damping effect on the mechanical behaviour due to the energy extraction, cannot be neglected. The power output that can be obtained is the same as for the STD technique but, as the limit is almost reached for a lower $k_{eff}^2Q_m$, Fig. 4.14, this performance is achieved with a significantly smaller device.

SECE technique In the STD and s-SSHI techniques, the transducer is directly connected to the load. In the first case, energy transfer occurs in one single step through the only rectification circuit while, in the latter, it occurs through the diodes bridge and the inductor. As main consequence, the load characteristics heavily influence the device behaviour and thus the power recovery performance. In realistic applications, this aspect may be penalising. R_L may not be fixed in advance, or it

may change due to environmental variations (temperature or humidity) or due to the operative state of the connected electronics.

By using the switching concept in a slightly different way, it is possible to avoid the problem of load-dependence obtaining the decoupling between the energy harvester and the electric load. The Synchronous Electric Charge Extraction (SECE) technique allows achieving this target by using the inductance for voltage inversion as intermediate energy storage element. Energy is transferred to the load in two steps. The first is the extraction phase. When the displacement reaches an extreme, the whole energy available on the piezoelectric element is delivered to the inductor through the switch. Then, the transfer phase occurs. The transducer is disconnected and, the energy stored in the inductor is provided to the load. The transducer and the load are never directly connected and thus the EH is independent from the connected circuit. Fig. 4.13 illustrates SECE architecture and typical waveform. Again, power conversion is controlled by the switch S that is open most of the time. The transducer is in OC and V_T grows with the displacement accumulating charges on the piezoelectric element. When z_r reaches an extreme, $t = t_0$, S is close and the electrostatic energy accumulated in the clamped capacitance is transferred to the coupled inductor L. This time, the aim of the inductor is not to perform the voltage inversion but to extract the electrostatic energy of C_p. Thus, the time interval is given by a quarter of the oscillator period, $\Delta t_{i\,\mathrm{SECE}} = \frac{\pi}{2}\sqrt{LC_p}$. At the time $t_0 + \Delta t_{i\,\mathrm{SSHI}}$, V_T passes at zero and all the electrostatic energy is removed from the piezoelectric element. S is opened, the transducer is again in OC and L performs the energy transfer to the electric load. At resonance, the power supplied to the load is [67]:

$$P_{\mathrm{SECE}} = \frac{2}{\pi}\frac{k^2 Q_m}{\left(1+\frac{4}{\pi}k^2 Q_m\right)^2}\frac{m^2\omega_{SC}^4 Z_{in}^2}{c_m} \tag{4.71}$$

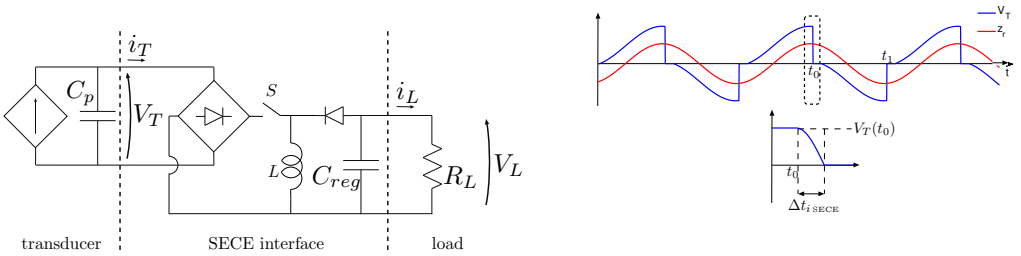

Fig. 4.13 SECE technique.

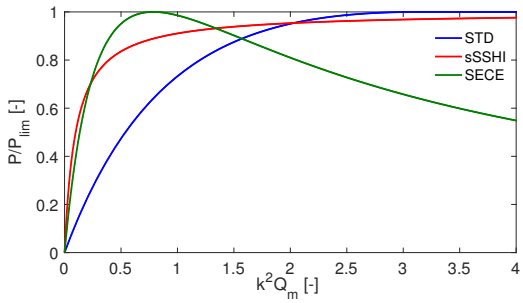

Fig. 4.14 Harvested power implementing different HIs as a function of k^2Q_m.

Compared to the s-SSHI technique, the harvested power implementing SECE is fully load independent and thus not influenced by its characteristics. It follows that, differently from the previous, there is no need for optimal resistor emulation circuit for power optimisation. In addition, when constant displacement magnitude is considered, such a technique permits to recover 4 times the energy recovered implementing the STD approach [39]. Considering the damping effect, a critical value of k^2Q_m appears. Above this threshold, the recovery performance deteriorates as k^2Q_m increases due to the impossibility to control the trade-off between energy extraction and damping effect.
In order to be able to control this trade-off, Double Synchronized Switch Harvesting (DSSH) technique [66] combines s-SSHI with SECE.

The three considered techniques are compared in Fig. 4.14 considering the harvested power with respect to the the global electromechanical coupling figure of merit k^2Q_m. For the load-dependent techniques, R_L is set to maximise the power recovery. The voltage inversion coefficient γ of s-SSHI is considered 0.75. Power is normalized with respect to the maximum recoverable amount implementing STD technique, eq. 4.68. The harvested power shows the same limit in the three cases. The difference regards the value of k^2Q_m for which this limit is reached. In the case of STD technique, this limit is achieved for $k^2Q_m > \pi$, whereas for sSSHI the power asymptotically tends to the limit value growing very fast for low k^2Q_m. For $k^2Q_m = 1$ the 90% of the limit value is gained. Conversely, SECE technique does not show a monotonic trend of power. Sharper growing than for sSSHI occurs at low k^2Q_m and for $k^2Q_m = \frac{\pi}{4}$ the limit value is reached. For larger k^2Q_m the trend is always decreasing and for $k^2Q_m > \frac{\pi}{2}$ performance is lower than the STD case.
From this analysis it is evident that for low coupled system, the amount of energy

that can be recovered implementing switching techniques is larger compared to the standard technique. Being the figure of merit $k^2 Q_m$ roughly proportional to the quantity of piezoelectric material used in the energy harvesting system, it can be noted that the implementation of these techniques allows recovering the same amount of energy with smaller piezoelectric patch.

4.4 Energy Harvesting modelling conclusions

In this chapter, the modelling of electromagnetic linear EHs and piezoelectric cantilever beam EHs is presented. Global simplified models are built taking into account mechanical and electrical parts and their energy exchange in both directions. Different techniques for power management are considered and their performance are compared in terms of the harvested power versus the global electromechanical coupling figure of merit.
It is worth noting that, since the energy extracted by the electrical part acts as a damping on the mechanical part of the system, the maximisation of the electromechanical coupling factor is not always the path to be followed in the process of performance optimization. In [78], Renno et al. clearly show as, considering steady state condition and resistive load, the amplitude of the displacement is always decreasing with coupling. Only in the case of optimal load resistance, recovered power reaches its maximum and displacement amplitude its minimum for a certain coupling value. They no more change by increasing the coupling. If load resistance is not optimised, recovered power reaches its maximum for a certain coupling value. Increasing the coupling, recovered power decreases toward zero as displacement amplitude decreases toward zero. These conclusions are achieved for a piezoelectric EH working in 33 mode employing a lumped parameters model equivalent to that herein used. Thus, outcomes can be extended to the EHs considered in this work. It is necessary to point out that, these considerations last for the case of steady state dynamics. When the dynamical behaviour of the system is governed by the transient, as in the case of shock or impact excitation, energy recovery performance can be optimized by maximizing the generalized electromechanical coupling coefficient and the mechanical quality factor of the structure [79]. In [79], Renaud et al. consider a cantilever beam piezoelectric EH employing a lumped parameters model equivalent to that herein used. It follows that, again, the results can be extended to the EHs

considered in this work.
Due to their simplicity, these models represent a very useful and lean tool for new EH application feasibility assessment and first design. Known the mechanical input of the system, by implementing such a tool in optimization algorithms, it is possible to evaluate the harvesting performance considering different scenarios (i.e. different coupling materials and phenomenon involved or different energy sources) and derive the optimal configuration of mechanical/electrical parameters. Constraints can be applied to stress out conclusions about performance and system behaviour in order to derive design guidelines. Once the application/energy source is identified, the further step consists in the building of a more specific and representative model to fine tune the parameters and to implement into the optimisation process their constraints due to the specific application considered. The final design is thus achieved.

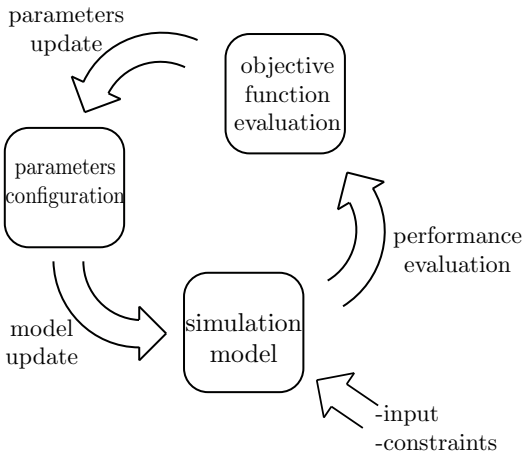

Fig. 4.15 Simulation model implementation in design/optimisation cycle.

Chapter 5

Electromagnetic EH: self-powered Bluetooth step counter

5.1 Introduction

In the context of the partnership between the *Department of Management and Production Engineering* and the *Department of Energy* of Politecnico di Torino with the *Analog and MEMS Group* of STMicroelectronics, the project aiming at developing a prototypes batch of self-powered Bluetooth step counter placed in the sole of a training shoe has been carried out.

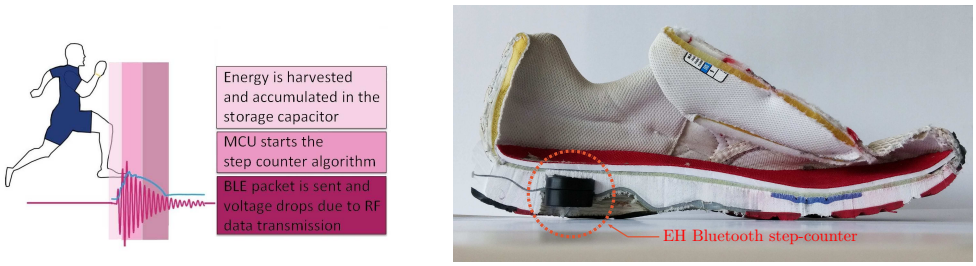

(a) (b)

Fig. 5.1 a) Device working principle and b) Bluetooth step-counter placed in the sole of a running shoe.

In the field of energy harvesting many practical applications exploiting different physical phenomena have been investigated and proposed, [80–83], but one of the most debated topics is the power supply of wearable electronics [84]. One such particular application regards sensor integrated in shoes. Two possible energy sources are available to collect energy in shoes: sole deformation during walking and shocks due to the impact of the heel on the ground. Piezoelectric devices using sole deformation are described in [85, 86] while inertial piezoelectric generators, composed by a cantilever beam with a mass on the free end, are described in [87, 88]. A generator using a flow between two pumps placed in the front and in the rear of the sole is presented in [89]. References [90, 91] present two linear electromagnetic generators with one or more magnets sliding into a guide horizontally placed in the shoe. A rotary generator activated by a harm extending under the sole is described in [92]. Reference [93] presents two electromagnetic generators, one with more magnets sliding into a guide placed horizontally in the shoe and one consisting of an oscillating cantilever arm. The mentioned works based on linear electromagnetic generators consider the transducer connected to a resistive load, neglecting the effect of actual loads containing electronic and reactive components.

In the following, the energy harvesting system for the Bluetooth step-counter developed in partnership with STMicroelectronics is presented. The energy conversion system consists of an electromechanical transducer integrated with an electronic interface. The aim is to power supply a Bluetooth step-counter placed in the sole of a training shoe exploiting only the energy harvested by the impact of the heel on the ground during each step of running activity, Fig. 5.1a. The energy demand is 3 mW at 1.8 V for 30 ms for each step in order to switch on the device, detect the event and send the data to a remote receiver. According to the standard running shoe sole size, the dimensional constraint consists of an overall $\varnothing\, 27 \times 16$ mm cylinder containing all the device components and the protective case.
For the electromechanical energy conversion, a linear electromagnetic generator like the one described in sec. 4.2 is considered. For the maximum power transfer to a storage capacitor, the transducer is embedded with a self-powered electronic interface based on a full wave boost converter that performs load decoupling and optimal load impedance emulation.
A typical acceleration profile for running steps in a slow jogging condition is shown in Fig. 5.2a. The device is placed in the heel of the shoe with the oscillation axis

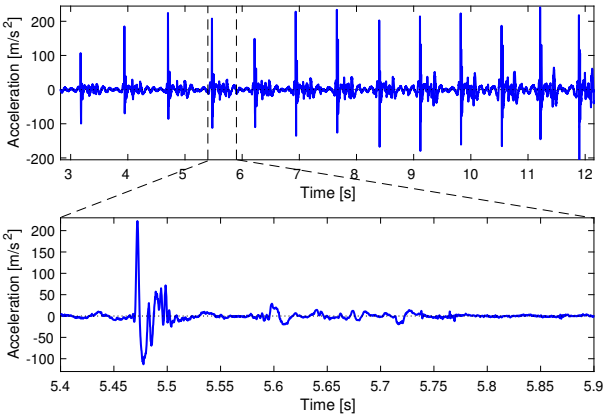

(a)

(b)

Fig. 5.2 a) Axial acceleration measured during running and detail of single step acceleration. b) Experimental setup for acceleration measurement in the heel of shoe during running.

of the magnet perpendicular to the sole, Fig 5.1b. After the heel impact, the free oscillation of the magnet with respect to the induction coils allows energy recovery. The design phase of the EH device consists of three main stages. At first, by means of an integrated mechanical and electromagnetic approach the transducer parameters have been optimised according to the dimensional constraints to maximise the converted mechanical energy. Subsequently, identifying the *electrical domain analogue matching condition* (EDAM) [56], load impedance ensuring maximum power transfer is defined in order to maximise the energy that can be provided to the electronics. Then, in order to make the energy available on the storage capacitor to the device supply, the HI is optimised to emulate the optimal load impedance resulting from the previous step.
Finally, the EH Bluetooth step-counter is prototyped. Numerical and experimental results are shown and discussed.

5.2 Self-powered Bluetooth step counter application

The aim of the considered application is to power supply a Bluetooth step-counter device with an energy harvester system in order to make it energetically autonomous. Placed in the heel of the sole of a running shoe, at each step the device switches on,

detects the event and sends the data to a remote receiver with an energy demand of 3 mW at 1.8 V for 30 ms, namely 90 µJ representing the target to be achieved.
Considering the size of the battery supplied equivalent device *Nike+ running* [94, 95], $35.0 \times 24.2 \times 7.5$ mm (width × depth × height), and considering the mean heel height of the sole in running shoes, 25 mm, a dimensional constraint consisting of a $\varnothing\, 27 \times 16$ mm cylinder containing all the device components and the protective case has been defined.
Fig. 5.2a shows the acceleration profile measured in the heel of a running shoe during slow jogging activity. Acceleration is measured along the direction perpendicular to the sole, z-direction. Acceleration along the two directions perpendicular to z, x and y-direction, are measured as well. A battery supplied *iNEMO inertial module* embedded with a storage memory for data saving, provided by STMicroelectronics, has been used for acceleration acquisition. Fig. 5.2b shows the experimental setup. As it can be seen in the upper plot of Fig. 5.2a, the steps frequency is very low, about 1.5 Hz, and it can vary during the activity. Considering the detail of the acceleration of a single step, lower plot, the peak due to the impact of the heel on the ground is very high in amplitude, around 200 m/s^2, and short in duration, around 1 ms. It follows that the mechanical source can be considered as a sort of series of impulses occurring with a time delay of approximately 0.65 s.
Generally, in energy harvesting studies the transducer is designed to work in resonance with a sinusoidal input. In this practical application, due to the nature of the input, the magneto-inductive transducer is not designed to work in resonance with the footstep frequency, but to optimally exploit the free oscillation of the floating magnet following the shock of every single step.
The working principle of the device can be summarised in three main stages. At the beginning of the step the transducer's magnet is almost motionless. After the impact, mechanical energy is transferred to the magnet that begins to oscillate with respect to the induction coils inducing voltage; the required energy amount is recovered and the target electronics supplied. As all the mechanical energy of the magnet has been converted in electric energy or dissipated by mechanical friction, at the end of the foot-step the magnet is again almost motionless. As each step is practically independent from the others, both in terms of dynamics and in terms of the electric device functioning, a single footstep is considered. According to Fig. 5.2a, the 4$^{\text{th}}$ foot-step shown is intermediate in terms of input acceleration amplitude, thus, it is considered for the design phase.

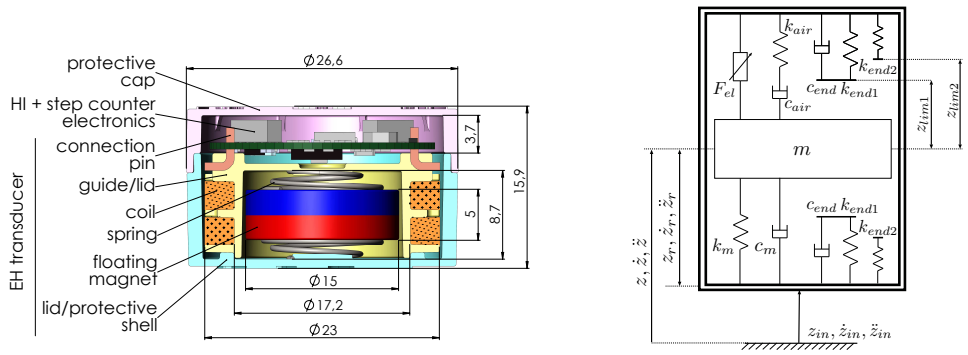

(a) (b)

Fig. 5.3 EH Bluetooth step-counter layout: main components and dimensions in mm.

5.3 Mechanical part and transducer design

Although very simple in layout, the considered EH provides high power density performance [70] resulting suitable for this kind of application. The layout is shown in Fig. 5.3a. A cylindrical magnet can slide into a cylindrical guide suspended between two conical springs providing a symmetric elastic characteristic. The device is placed in the shoe with the oscillation axis of the magnet perpendicular to the sole. Two coils connected in series are symmetrically wound around the guide in opposite directions to one another. Except for the end of the stroke, the flux through the coils is opposite in sign but not in derivative with respect to the relative displacement z_r, as shown in details in sec. 5.3.1. It follows that the overall magnetic flux linkage derivative is the sum of the single coils effects. Inertial forces, due to the impact between the shoe housing the system and the ground, induce motion in the magnet. The movement of the magnet causes a variation of the flux linkage in the coils and so a voltage is induced between the ends of the coils.

In order to better describe the system, starting from the simplified energy harvester model of eq. 4.7, the contributes due to the different elements involved in the real system have been added. In particular, the terms related to the mechanical stiffness k_m and viscous damping c_m, have been expanded in order to take into account the effect of the magnet friction against the guide, the effect of the air into the device and the effect of the impacts against the end-strokes.

Design and modelling details, numerical model validation and parameters optimisation are discussed in the following.

5.3.1 System design and modelling

Magnetic floating mass and elastic characteristic The floating mass is a NdFeBr cylindrical magnet. This material presents 7300 kg/m^3 of density and high values of residual magnetic induction, suiting the considered application requirements.
Suspending the magnet between two conical pre-compressed springs, a linear elastic characteristic is obtained. Conic springs ensure minimal close-wound encumbrance. An alternative solution consists in suspending the floating element between two fixed magnets opposite in orientation to obtain a cubic elastic characteristic [96]. This hardening characteristic allows reducing mass maximum displacement without affecting power output as shown by Green et al. [97]. The drawback is that in the practical realisation of the system, very small misalignments of the magnets lead to high radial forces acting on the floating mass. As a consequence, it is pushed against the guide producing high friction. For this reason, mechanical conical springs are adopted.

Damping characteristic Due to the input accelerations perpendicular to the oscillation axis of the magnet, friction force F_f opposes the moving of the magnet itself. Friction force is related to the force exchanged between magnet and guide by means of the friction coefficient μ_f:

$$F_f = |\boldsymbol{F}_f| = \mu_f(|\boldsymbol{F_N}|) \tag{5.1}$$

$$\boldsymbol{F_N} = \boldsymbol{F_x} + \boldsymbol{F_y} \tag{5.2}$$

where $F_x = m\ddot{x}$ and $F_y = m\ddot{y}$ are the contact forces along x and y-directions. The moment generate by F_f on the magnet is neglected.
A Stribeck exponential model depending on $\dot{z}_r$ has been considered for the friction coefficient:

$$\mu_f = \underbrace{\mu_s e^{-\alpha_\mu \dot{z}_r}}_{static term} + \underbrace{\mu_k(1-e^{-\beta_\mu \dot{z}_r})}_{kinematic term} \tag{5.3}$$

where μ_s and μ_k are the adhesion and friction coefficients, and the transition between static and kinematic behaviour is controlled through the parameters α_μ and β_μ. Model parameters cannot be determined a priori. A fitting procedure against

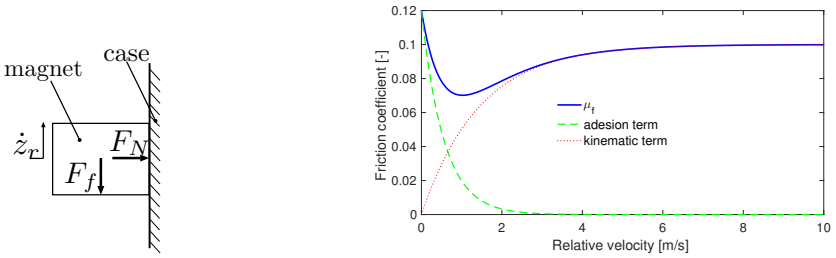

(a) (b)

Fig. 5.4 a) Friction force scheme and b) friction coefficients as a function of relative velocity.

experimental data is required. Fig. 5.4 provides an example of the friction model trend.

Coils modelling The considered EH layout presents two induction coils wound around the guide in opposite directions to one another. The magnetic flux linkage and the resistive and inductive characteristics of the two coils are proportional to the number of coil turns N_{coil}. Dividing the cross-section of the one coil by the cross-section of the wire, N_{coil} is derived. Considering a rectangular cross-section coil and a circular cross-section wire:

$$N_{coil} = p_f \frac{2(d_{c\,ext} - d_{c\,int})h_c}{\pi d_{wire}^2} \tag{5.4}$$

where $d_{c\,ext}$, $d_{c\,int}$, h_c are the external diameter, the internal diameter and the height of the coil, and d_{wire} is the diameter of the copper wire. p_f is the packaging factor, a coefficients that takes into account that, due to the circular cross-section of the wire and due to the insulating coating, not the whole coils cross-section is filled with conductor material.

The resistance of the coil R_{coil} is evaluated by multiplying the resistance of the average turn by the number of turns of the coil:

$$R_{coil} = 2\frac{1}{\sigma_{Cu}} \frac{d_{c\,ext} + d_{c\,int}}{d_{wire}^2} N_{coil} \tag{5.5}$$

where σ_{Cu} is the copper conductivity.
Through the Wheeler approximation [98, 99], coil inductance is estimated as:

$$L_{coil} = 10^{-5} \frac{3.15(d_{c\,ext} + d_{c\,int})^2 N_{coil}^2}{24(d_{c\,ext} + d_{c\,int}) + 144h_c + 80(d_{c\,ext} - d_{c\,int})} \tag{5.6}$$

Flux linkage is given by the integral of the magnetic field perpendicular to the average turn calculated on the surface of the turn itself and multiplied by N_{coil}:

$$\lambda_{coil} = N_{coil} \frac{1}{h_c} \int_{h_c} \int_{A_c} B_z \mathrm{d}A\mathrm{d}z \tag{5.7}$$

where B_z is the magnetic field along z-direction and A_c is the area of the average coil. Since the coils are connected in series and wound in opposite direction, R and L are given by the sum of the values computed for the single coils and λ' by the difference:

$$R = R_{upper\,coil} + R_{lower\,coil} \tag{5.8}$$

$$L = L_{upper\,coil} + L_{lower\,coil} \tag{5.9}$$

$$\lambda' = \lambda' upper\,coil + (-\lambda' lower\,coil) \tag{5.10}$$

FEMM software [100] for axisymmetric problems driven by Matlab script is used to integrate the magnetic field equation in order to compute λ' as a function of z_r and its derivative with respect to z_r, Fig. 5.5.
Fig. 5.6a shows the magnetic flux for the upper and lower coils, while Fig. 5.6b illustrates the flux linkage derivative.
One important parameter influencing λ is the external diameter of the coils. By increasing $d_{c\,ext}$, the flux linkage increases leading to beneficial effects. However, increasing the external diameter of the coils implies increasing wire length and thus the intrinsic resistance. The benefit due to larger λ is neutralised by larger electrical losses. Optimal balance between the two effect is one of the goal of the device design.

End-strokes modelling The oscillation of the floating mass is limited by the two flat surfaces of the guide, see Fig. 5.3a. These elements represent the end-strokes of the system and are modelled by a Kelvin-Voigt spring-dashpot model where the spring presents bi-linear characteristic [8, 101]. A piecewise linear characteristic is used to describe the impact of the moving mass against the stoppers. If the relative

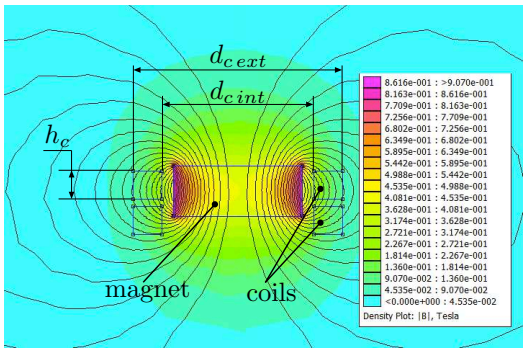

Fig. 5.5 FEMM: magnetic induction distribution for a given position of the magnet.

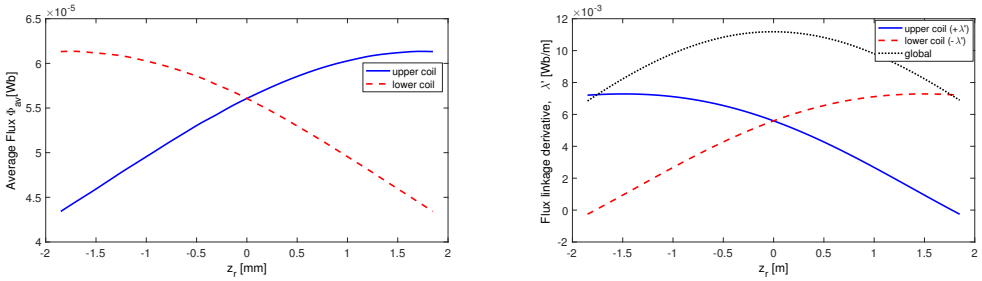

(a) (b)

Fig. 5.6 Magnetic flux (a) and magnetic flux linkage derivative (b) through the coils with respect to the relative displacement.

displacement is within $\pm z_{lim1}$, the force exerted by the end-strokes is null. When the magnet hits the stoppers, the force that they exert is due to a dissipative behaviour, c_{end}, and due to an hardening elastic behaviour, k_{end1} until $\pm z_{lim2}$, then k_{end1} and k_{end2}.

The resulting elasto-dissipative force F_{end} acting on the floating mass is:

$$F_{end} = \begin{cases} -k_{end1}(z_r - z_{lim1}) - k_{end2}(z_r - z_{lim2}) - c_{end}\dot{z}_r & \text{if } z_r > z_{lim2},\ F_{end} < 0 \\ -k_{end1}(z_r - z_{lim1}) - c_{end}\dot{z}_r & \text{if } z_r > z_{lim1},\ F_{end} < 0 \\ 0 & \text{otherwise} \\ -k_{end1}(z_r + z_{lim1}) - c_{end}\dot{z}_r & \text{if } z_r < -z_{lim1},\ F_{end} > 0 \\ -k_{end1}(z_r + z_{lim1}) - k_{end2}(z_r + z_{lim2}) - c_{end}\dot{z}_r & \text{if } z_r < -z_{lim2},\ F_{end} > 0 \end{cases} \tag{5.11}$$

Stiffness and damping parameters need to be calculated against experimental data.

Air effect modelling When the floating magnet oscillates into the guide, it acts as a sort of piston that separates two chambers connected by the small clearance between the magnet and the guide themselves. The pressure difference into the cambers due to the air compression generates an elastic force acting on the magnet. The airflow through the clearance reduces the pressure delta producing a dissipative effect.
In order to take into account the affect of the air, a Maxwell linearised model valid for small displacement [102] is employed, Fig. 5.3b. A spring k_{air} and a dashpot c_{air} in series model the elastic effect of the air and the dissipative effect of the airflow through the clearance. The first is connected to the floating mass while the second to the frame of the device. The connecting point has the coordinate z_{air} and the force equilibrium gives:

$$\begin{cases} F_{air} = -k_{air}(z - z_{air}) \\ F_{air} = -c_{air}(\dot{z}_{air} - \dot{z}_{in}) \end{cases} \tag{5.12}$$

$$F_{air} + \frac{c_{air}}{k_{air}}\dot{F}_{air} = -c_{air}\dot{z}_r \tag{5.13}$$

Also these parameters have to be tuned against experimental data by means of a fitting procedure.

Energy harvester simulator The model that describes the behaviour of the different components of the device has been implemented in the Matlab Simulink environment in order to build a simulator. A numerical model based on the *block-oriented* logic has been developed. Each part interacts with the others exchanging mutual actions and reactions. Four main subsystems compose the EH device, Fig. 5.7: the input signal, the generator (mechanical part comprehensive of transducer), the harvester interface and the electric load. The input block generates the acceleration profile that shakes the energy harvester. It can be a sinusoidal input or the acceleration profile measured in heel of the training shoe during running activity.
The generator subsystem is partitioned in several blocks corresponding to the elements that contribute to the dynamics of the system, Fig. 5.8.
Floating magnet: a 3 degrees of freedom model takes into account axial displacement z and radial displacements x, y. It gets as inputs the forces along z direction applied by other components and the system acceleration. As output it gives magnet dynamics.

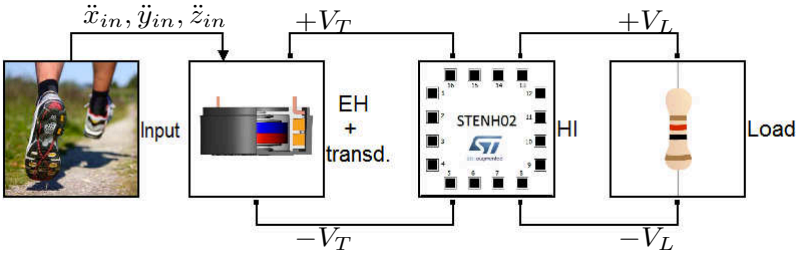

Fig. 5.7 Energy harvester simulator.

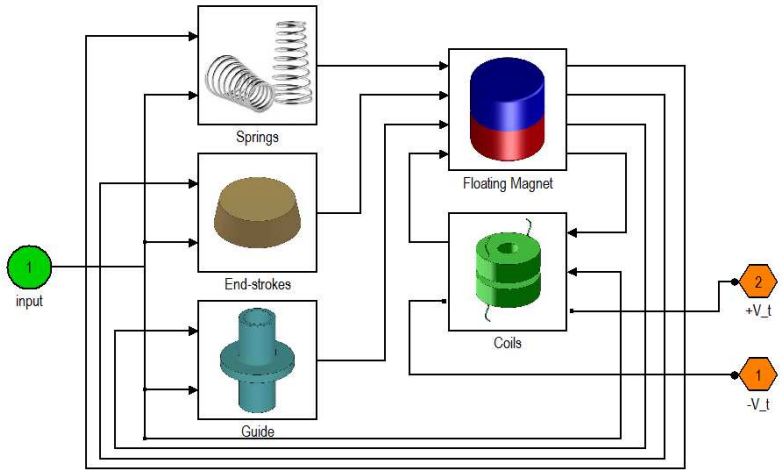

Fig. 5.8 Energy harvester generator subsystem.

Guide: this block gets the input and the magnet dynamics to compute the forces acting on the magnet due to friction against the guide wall and due to the air.
Springs: it gets the input and the magnet dynamics to compute the force due to the springs.
End-strokes: it gets the input and the magnet dynamics to compute the elastic and dissipative forces due to the impact between the floating magnet and end-strokes.
Coils: it gets the input and the magnet dynamics and the current at the transducer terminals. It computes the voltage at the transducer terminals and the force acting on the magnet due to the electrical part of the system.

5.3.2 Model validation and parameters optimisation

Model validation A first series of prototypes of electromechanical generator has been developed and tested in order to validate and tune the simulation model, Fig. 5.9a. Both constant acceleration sine sweep and both heel-strike have been simulated and experimentally tested. The experimental setup used for the model identification is based on the *LMS TestLab* system. A *Dongling ESD-045* shaker controlled in position reproduces the acceleration profile of the mechanical input. An uni-axial accelerometer placed next to the device closes the control loop. Transducer voltage signal is acquired by the *LMS TestLab* acquisition system and a Tektronix TDS210 oscilloscope. A priori unknown parameters of the model are defined by a best-fit procedure of the transducer output voltage V_T in OC condition. Satisfactory matching between simulations and experiments has been found. Fig. 5.9b shows a 0.33 Hz/s liner direct sweep from 60 to 160 Hz at 5 g of acceleration amplitude. Close to the resonance, non-linear trend is due to the impact of the magnet against the end-strokes. Fig. 5.9c reports the response to a footstep acceleration profile. The numerical model shows slightly more damped trend with the consequent shorter duration of the magnet free oscillation.
The updated model is used as starting point for the optimisation process.

Optimisation The nature of the specific application imposes very stringent dimensional constraints to the device: a cylindrical shape volume of ⌀27×16 mm that must contain the electromagnetic generator, the HI, the step-counter electronics and the protective shell. It follows a dimensional constraint for the generator even more

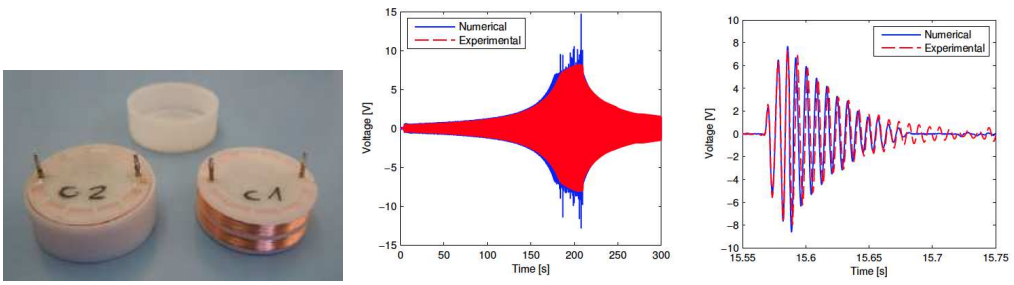

(a) (b) (c)

Fig. 5.9 Comparison between numerical and experimental transducer output voltage V_T for a) sine sweep and b) simulated heel-strike.

severe: ⌀23×16 mm.
The dimensional constraints imposed, the energy requirement of the target electronics and the exploited energy source, imply the need to maximise recovery performance. Thus, the simulation model has been implemented in an optimisation loop based on the the Pattern Search algorithm [103], a well know 0th order deterministic technique extensively used in the automated optimisation environment.
Fig. 5.11a summarises the main loop steps. Starting from the geometrical dimensions, all the operative parameters (mass, springs, oscillation amplitude, coils dimensions, number of turns in coils) are calculated. Through the FEMM model, flux linkage is calculated as a function of the magnet position. Then the system is simulated using the footstep acceleration profile to excite the device. Finally, the mean harvested power per footstep is evaluated. In this stage, a resistive electric load $R_L = R$ directly connected to the transducer terminals has been considered.
The computational cost of the optimisation process is not negligible. This is mainly due to the objective function evaluation; for a given acceleration profile, the simulation of 1 second requires about 10 minute of CPU time. Pattern Search algorithm well suites the problem. Its main features regard the search in the space of the optimisation variables along coordinate directions. The definition of a preferred search line, the *pattern*, leads to a fast motion toward region where the objective function values are high. As for the other deterministic algorithms, the result is a global optimum only in the case of convex objective function landscape. Local maxima regions, if present, may trap the search. A result dependent on the process starting point follows. Multi-starting strategy permits a wider exploration of the objective function landscape limiting local maxima errors.
Table in Fig. 5.10b summarises the degrees of freedom of the optimisation and their bounds. These parameters are the spring stiffness and the main geometrical aspects of the device shown in Fig. 5.10a. The springs are optimised considering the stiffness instead of the geometrical parameters that are subsequently derived. Being some geometrical parameters not fully independent, the optimisation parameters are less than those labelled in Fig. 5.10a. Six parameters are considered: the floating magnet diameter and height, the mechanical stiffness, the coils height and their distance.
Optimisation results are summarised in Fig. 5.11. The improvement of the recovery performance is mainly reached by tuning the elastic characteristic of the system and the magnet heigh. The first aspect affects the exploitation of the available stroke. The second implies variations both in the mass of the floating element, since its diameter

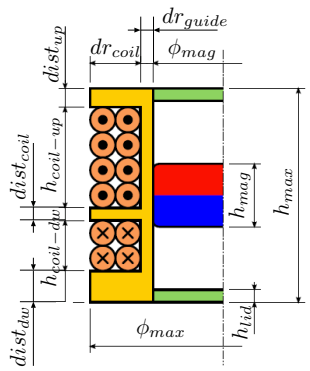

(a)

Parameter	LB	UB
magnet diameter ϕ_{mag} [mm]	10	15
magnet height h_{mag} [mm]	3	6
stiffness k_m [N/m]	1000	5000
coil gap $dist_{coil}$ [mm]	0.6	1.6
upper coil height $h_{coil-up}$ [mm]	1.6	3.2
lower coil height $h_{coil-dw}$ [mm]	1.6	3.2

(b)

Fig. 5.10 Optimisation parameters and their upper bound (UB) and lower bound (LB).

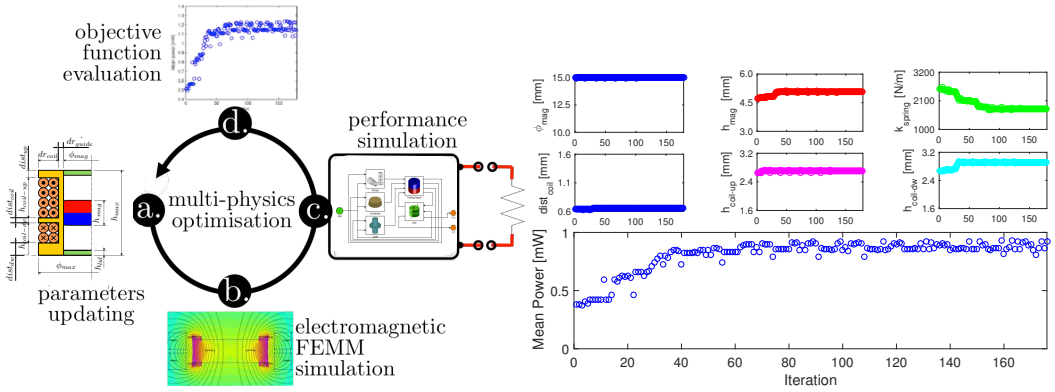

(a) (b)

Fig. 5.11 a) Optimisation process loop and b) evolution of the optimisation parameters and objective function.

remains almost unvaried, both in the magnetic characteristics of the systems, and both in the available stroke. Also the upper coil height is slightly increased.

Starting from the resulting configuration, a second series of prototypes has been made in order to experimentally refine the friction terms implementing a new best-fit procedure. Subsequently, a new optimisation process is performed to derive the best configuration.

Tab. 5.1 summarises the main parameters of the generator. For the sake of clarity, linearised value of non-linear parameters has been reported. Geometrical dimensions of the engineered solution are reported in the scheme of Fig. 5.3a and in the drawings of Fig. 5.21.

Table 5.1 Electromagnetic EH model main parameters.

m	Floating magnet mass	$5.856g$
c_m	Optimal linearised mechanical damping coefficient	$0.0502\frac{kg}{s}$
k	Overall spring stiffness	$1792.2\frac{N}{m}$
f_n	Undamped system natural frequency	$88.05Hz$
ζ	Optimal linearised mechanical damping ratio	1.55%
λ'	Linearized overall flux linkage gradient	$15.25\frac{Wb}{m}$
R	Transducer coils overall resistance	1187Ω
L	Transducer coils overall inductance	$61.56mH$

5.4 Electrical part design

In the following, harvester interface design is illustrated. Load impedance that maximises recovery performance is firstly investigated. Then, the standard (STD) and an active HI are described, simulated and compared.
[64, 37, 65] propose HI solutions based on pulse modulation and maximum power transfer tracking to perform voltage rectification/boost to charge a capacitive buffer. Here, a tunable interface consisting in a full wave boost converter driven by an input-powered control logic has been implemented. Exploiting pulse width modulation (PWM) at high frequency with respect to the mechanical dynamics of the system, the HI performs maximum power transfer impedance emulation, transducer-load decoupling and storage capacitor charging to supply the target electronics.

5.4.1 Load impedance optimisation

In order to define the electric load impedance that maximises energy transfer representing the performance upper limit, a pure resistive load is firstly considered.
A simple resistor directly connected to the ends of the transducer coils, thus subject to V_T, instantaneously dissipates the transferred power by Joule's effect. With this configuration, load impedance influence on the energy conversion chain is investigated and R_L that maximises power transfer defined fixing the maximum energy that can be recovered. Therefore, this configuration represents the reference against which the performance embedding the system with HI will be evaluated.

In [56] and [104], the power recovery of a base-excited mass-spring-damper energy harvester with limited stroke for seismic mass displacement, has been analysed in a steady-state condition. As mathematically proved in [56] and shown in sec.4.2, when sinusoidal vibration input in resonant condition is applied to a linear electromechanical system, the maximum power delivered to the electric load is obtained when:

$$R_L = R + \frac{\lambda'^2}{c_m} \tag{5.14}$$

thus introducing a new term in the classical *maximum power transfer theorem* that takes into account dissipative phenomena in the mechanical part of the system. As anticipated in sec. 4.2.3, Maximum power transfer is no more achieved in *electrical resistance matching* condition, $R_L = R$, but in EDAM condition, $R_L > R$, [56].
Optimal damping condition is considered in [105, 106] when impulsive excitation is applied. No analytical conclusions are stressed about optimal resistive load but again $R_L > R$ results.
Defining the average harvested power per running-step p_L and the overall efficiency η_{EHHI} as:

$$p_L = \frac{W}{T} \tag{5.15}$$

$$\eta_{EHHI} = \frac{W}{W_0} \tag{5.16}$$

where W is the energy dissipated on the load, W_0 is the mechanical energy converted into electrical energy and T is the foot-step duration, Fig. 5.12 shows the trends versus R_L.
Similar conclusions to that of literature for the steady-state case and for the impulsive input are still valid in the considered case. Performance in case of $R_L = R = 1187\Omega$ and $R_L = R_{opt} = 2010\Omega$ are highlighted.
As expected, the efficiency is growing with R_L as a larger part of the converted energy is dissipated on the load resistor. The maximum power transfer, 1.01 mW, occurs beyond the classical *electrical resistance matching* condition showing a performance increase of about 7.5% with respect to the 0.94 mW achieved in that condition.
The optimal resistive load configuration is held as reference for the following performance evaluations.

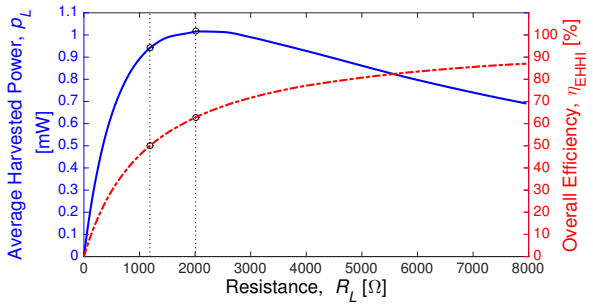

Fig. 5.12 Average harvested power per running-step (solid line) and overall efficiency (dotted line) versus R_L.

5.4.2 STD interface

The so called *standard* interface is the simplest way to ensure electrical compatibility. A diodes bridge rectifier is interposed between the transducer and the capacitor to rectify V_T. Fig. 5.13 shows the scheme of the electrical part of the system. The grey component in parallel to C_{out} represents the step-counter electronics. Its functioning is simulated by means of a power consumption p_e. Although very simple to be

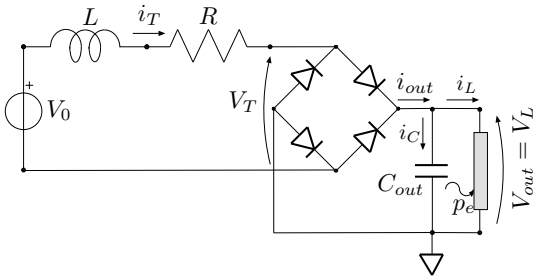

Fig. 5.13 Rectifying interface with Graetz bridge. The grey component connected in parallel with C_{out} is a controlled load draining a power p_e corresponding to the different working phases of the step-counter.

implemented, this solution presents heavy limitations due not only to the voltage drops in the bridge diodes. In this configuration, the output capacitor can be charged only when:

$$|V_T| - \Delta V_{rect} > V_L \tag{5.17}$$

where ΔV_{rect} is the voltage drop through the diodes of the rectifier. As shown in Fig. 5.9b, being the dynamics of the system the free oscillation following a shock input, the transducer voltage is an oscillation of decreasing amplitude. It follows that to the increasing of the charge of the output capacitor, corresponds the reduction of

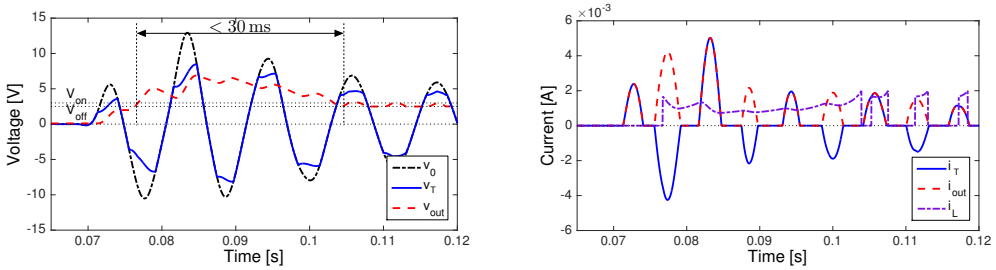

(a) (b)

Fig. 5.14 Waveforms of a) voltages and b) currents defined in Fig. 5.13.

time intervals where eq. 5.17 is satisfied. Thus the transducer remains in open-circuit and the mechanical energy extracted from the source is wasted in mechanical losses. Fig.s 5.14a and 5.14b show the waveforms of voltages and currents defined in the circuit of Fig. 5.13. The step-counter electronics is conservatively simulated as a power consumption p_e of 5 mW that starts when V_L reaches the voltage threshold $V_{on} = 3$ V and stops when it decreases below $V_{off} = 2.5$ V. It is evident how the current flux downstream the bridge rectifier is limited into the neighbourhood of the transducer voltage peaks.
It results that, by implementing this interface, at each foot-step the target electronics is supplied for a too short time interval, less than 30*ms*, proving to be unsuitable for the application.

5.4.3 Electronic interface

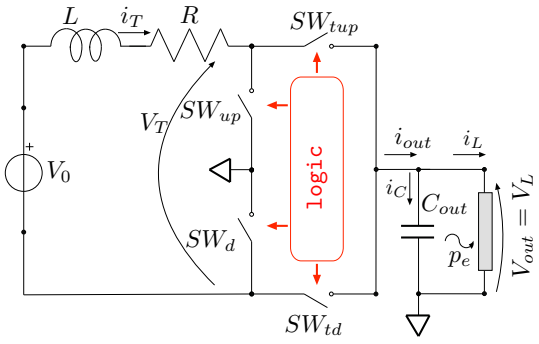

Fig. 5.15 Transducer electrical part embedding electronic interface. The grey component connected in parallel with C_{out} is a controlled load draining a power p_e corresponding to the different working phases of the step-counter.

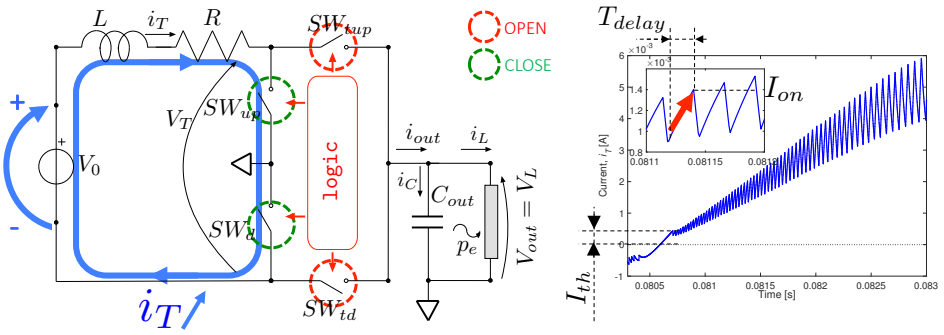

(a)

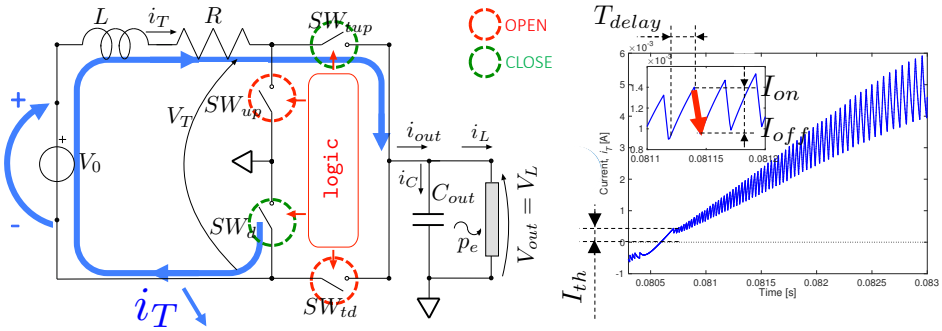

(b)

Fig. 5.16 HI working principle: a) energising and b) transferring phase.

In order to overcome the limits of the standard interface and to obtain maximum power transfer, an electronic HI has been developed.

The interface is directly connected to the terminals of the transducer and its control logic is power supplied by the transducer itself. The HI is based on a full wave active boost converter (Fig. 5.15) driven by an ultra-low power microcontroller equipped with a transducer current controller. Exploiting high frequency switching, >20 kHz, with respect to the low frequency dynamics of the transducer, <100 Hz, the interface performs PWM for optimal resistive load emulation while charging the output capacitor independently from the signal provided by the transducer (shape and voltage level) and from the voltage of the storage capacitor.

Referring to Fig. 5.15, on positive polarity of V_0 the logic keeps SW_d closed, SW_{td} opened, and acts on SW_{up} and SW_{tup}; transducer energy is transferred to C_{out} by

SW_{tup}. The opposite is valid for the negative polarity of V_0: the logic keeps SW_{up} closed, SW_{tup} opened, and acts on SW_d and SW_{td}; transducer energy is transferred to C_{out} by SW_{td}.

The working principle is based on the alternation of two phases, see Fig. 5.16: *energising* and *transferring*. Three parameters have to be set in order to tune the PWM: T_{delay}, I_{th} and α_{HI}. Their meaning is explained in the following.

Focusing on positive transducer polarity, during *energising* the control logic keeps SW_{up} and SW_d closed while SW_{tup} and SW_{td} opened. The transducer is short-circuited, i_T rapidly increases and the mechanical energy converted into electrical is in part stored in the transducer inductor L and in part inevitably dissipated in the coil resistance. This phase lasts until two conditions are contemporarily satisfied: a fixed time T_{delay} has elapsed since the phase began and i_T is above a minimum threshold I_{th}.

When both conditions are satisfied, the actual current level I_{on} is stored by means of a sample&hold circuit. The control logic opens SW_{up} and closes SW_{tup} connecting the transducer to the output capacitor. The *transferring* phase begins. i_T decreases and energy is transferred from L to C_{out}. A current sense circuit combined with the sample&hold circuit controls when the transducer current drops below I_{off} defined as:

$$I_{off} = \frac{I_{on}}{\alpha_{HI}} \tag{5.18}$$

where α_{HI} is a constant parameter set in the HI. When the condition $i_T < I_{off}$ is satisfied, SW_{tup} is opened, SW_{up} closed and the next *energising* phase begins.

The algorithm results in a hysteretic current control between two thresholds, I_{on} and I_{off}, that are directly related to the transducer voltage V_0 and are dynamically refreshed every energizing-transferring cycle.

Due to the very high frequency switching of the HI with respect to the magnet oscillation, the mechanical inertia filters out high frequency components of the current and, as a consequence, the current influencing the dynamics of the transducer is like a moving average of i_T. This value follows the same trend of the current in the case of resistive load. By tuning T_{delay}, I_{th} and α_{HI} it is possible to set the impedance seen by the transducer or, in other words, the equivalent resistor connected to the transducer. The simplicity of the proposed resistive load emulator guarantees very low quiescent current consumption.

The electrical/electronic interface is designed in the PSpice based simulator ELDO by Mentor Graphics [107] and then transposed in Simulink SimPowerSystems and

Stateflow Toolbox to be easily interfaced with the model of the generator. Parasitic resistances of the electrical components and voltage drops switches have been considered.

Fig.s 5.18a and 5.18b summarise the electrical behaviour of the transducer embedded with the active interface, the storage capacitor and the target electronics consumption p_e. Unlike the previous case, the step-counter electronics is off until V_L is less than $V_{on} = 10\,\text{V}$; then, the power consumption $p_e = 5\,\text{mW}$ begins and continues until V_L decreases under $V_{off} = 3\,\text{V}$. The voltage trend shows that the voltage on the output capacitor quickly grows and the transducer continues charging C_{out} when V_0 is lower than V_L. With the bridge rectifier this condition represents an open circuit. The first oscillations highlight the two behaviours of the system: the passive power transfer until V_L is lower than V_0 minus the voltage drops due to the switches, and the active transfer when this condition is no longer satisfied. Similar observations derive from the current plot where it is possible to note a current flux downstream the HI at every oscillation.

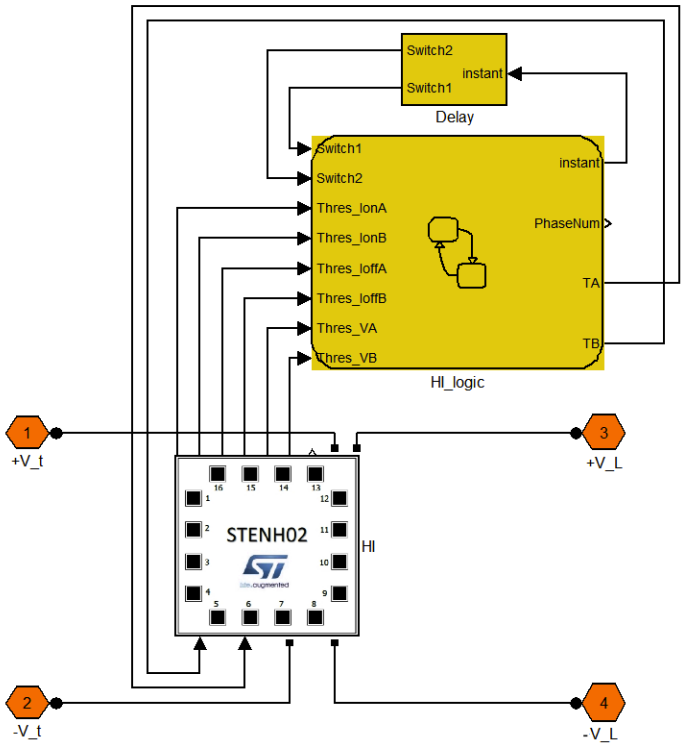

Fig. 5.17 HI subsystem.

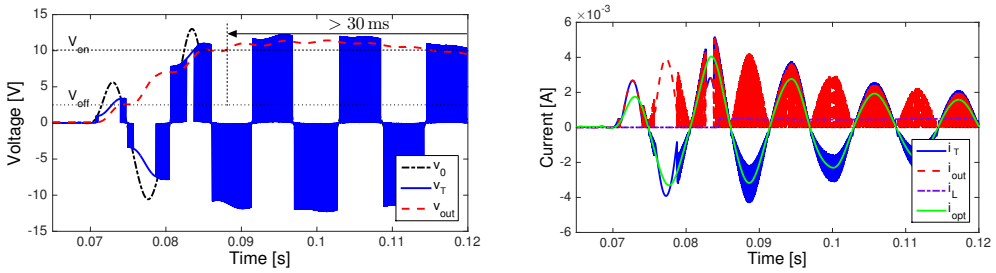

(a) (b)

Fig. 5.18 Waveforms of a) voltages and b) currents defined in Fig. 5.15 assuming $\alpha_{HI} = 2$ and $T_{delay} = 20\,\mu s$.

Parameters tuning One of the major benefits of the proposed interface is the tunability of the control logic parameters. By setting the *energising/transferring* parameters T_{delay}, I_{th} and α it is possible to vary the impedance of the equivalent load connected to the transducer.

Appropriate tuning of T_{delay} and α_{HI} results a current shape i_T whose moving average i_{eq} exactly fits the current in the case of optimal resistive load directly connected, i_{opt}.

Fig. 5.19 shows the effects of these two parameters on the transducer current i_T. The global effect of both α and both T_{delay} is to rise and increase the bandwidth of i_T, and to shift the switching between the active and passive power transfer.

By means of an optimisation process like that previously described, T_{delay} and α_{HI} that maximise the average power per foot-step provided downstream the interface have been identified. Fig. 5.20a shows the trend of this parameter as a function of T_{delay} and α_{HI}. For $\alpha = 2$ and $T_{delay} = 20$ µs the power transfer is maximum. As illustrated in Fig. 5.18b, with these parameters set, i_T fits the current i_{opt}. It follows that the generator behaves like in the case of optimal resistive load and the harvested power is 0.84 mW, approximately corresponding to the value obtained in the case of $R_L = R_{opt}$ minus the power consumed by the control logic and the power dissipated by the interface parasitic losses (see Table 5.2).

Numerical results of Fig. 5.18 confirm that, embedding this HI, higher charge level of the capacitor is achieved. The power supply of the load electronics lasts for a satisfactory time interval, longer than 30 ms, making this solution suitable for the specific purpose.

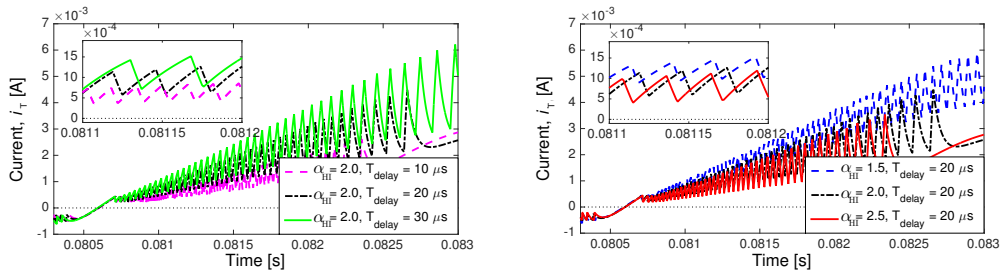

(a) (b)

Fig. 5.19 Effect of T_{delay} (a) and α_{HI} (b) on the transducer current i_T.

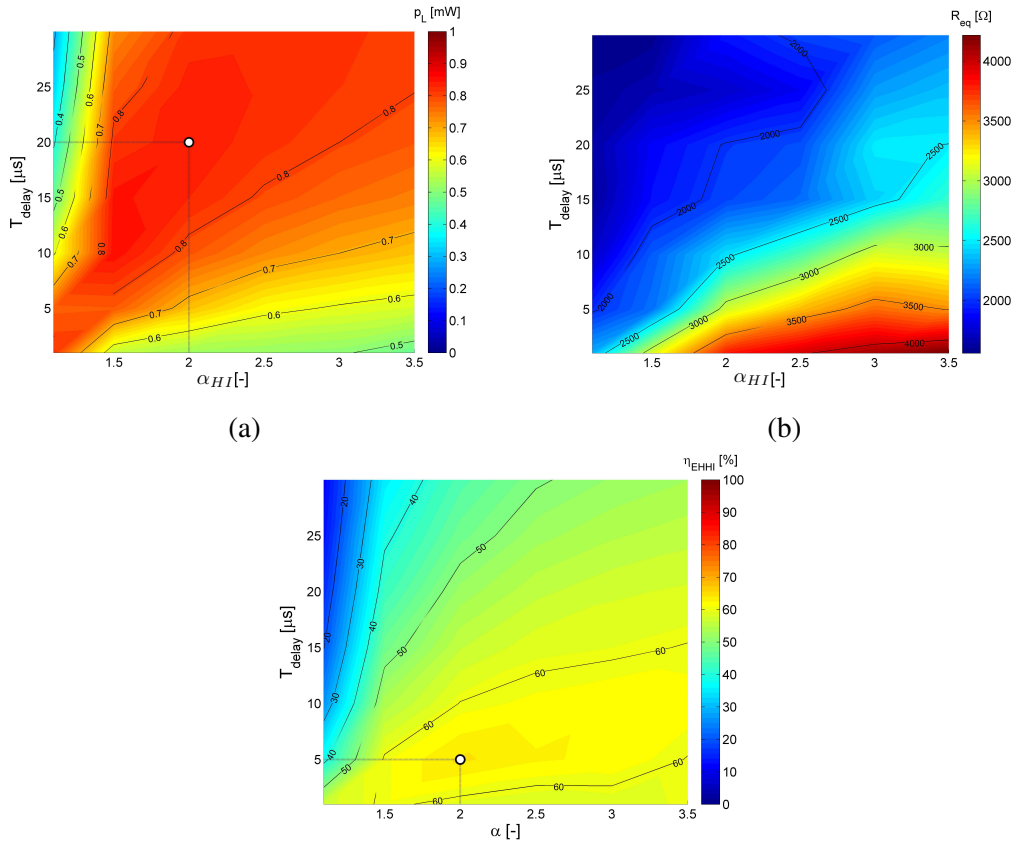

(a) (b)

(c)

Fig. 5.20 Effect of T_{delay} and α a) on the average power provided to the electric load per step, b) on the equivalent resistive load, c) on the global efficiency of the device η_{EHHI}.

5.4.4 HI efficiency analysis

In order to evaluate the energy transfer ability of the device, the following time-averaged efficiencies are defined:

$$\eta_{EH} = \frac{\frac{1}{T}\int_0^T V_T i_T dt}{\frac{1}{T}\int_0^T V_0 i_T dt} \tag{5.19}$$

$$\eta_{HI} = \frac{\frac{1}{T}\int_0^T V_L i_L dt}{\frac{1}{T}\int_0^T v_T i_T dt} \tag{5.20}$$

where T is the time duration of each running foot-step period, η_{EH} takes into account the internal electrical loss of the transducer and η_{HI} the loss due to the harvester interface.
The efficiency of the energy transfer is given by:

$$\eta_{EHHI} = \eta_{EH} \cdot \eta_{HI} \tag{5.21}$$

Table 5.2 reports the efficiency values of the different phases in the case of simple resistor, STD interface and active interface obtained from the simulation model.
In the resistive load configuration, η_{HI} is equal to 1 because all the converted power is transferred to the load. Unlike the power transfer, η_{EH} presents the monotonic increasing trend with R_L shown in Fig. 5.12. The optimal resistive load represents the best compromise between available power due to the electromechanical coupling and transfer ability due to the electric circuit parameters.
In order to take into account the feedback of the HI on the mechanical part, the standard and the active interface are related to the resistive case; the equivalent resistance seen by the EH is approximated by the running average of the ratio between V_L and i_L:

$$R_{eq} = \frac{1}{T_p}\int_{T-T_p}^{T} \frac{V_L}{i_L} dt \tag{5.22}$$

where T is the considered time instant and T_p is the time interval for the average calculation.
In the STD case, the transducer is mostly in open circuit and, thus, the equivalent resistance is higher than in the optimal load impedance case, $R_{eq} > 2500\,\Omega$. The efficiency η_{EH} is larger as well but, the poor HI energy transfer, 76%, gives rise to a lower overall efficiency, 51%. Low value of harvested power results, 0.47 mW.

Table 5.2 Efficiency values obtained by different interfaces and average power per step provided to load.

	Resistive load		**Graetz bridge**	**Active interface**	
	R_{adapt}	R_{opt}		$\alpha = 2$ $T_{delay} = 20\,\mu s$	$\alpha = 2$ $T_{delay} = 5\,\mu s$
η_{EH}	0.50	0.63	0.68	0.60	0.76
η_{HI}	1.00	1.00	0.76	0.87	0.85
η_{EHHI}	0.50	0.63	0.51	0.52	0.64
p_L [mW]	0.94	1.02	0.47	0.84	0.68

In the active interface case, by tuning T_{delay} and α_{HI}, R_{eq} is set (see Fig. 5.20b). Considering Fig.s 5.20a and 5.20c, it is clear that again the maximum power transfer configuration does not match the maximum overall efficiency one. Again, it is the best compromise between power conversion and power transfer. In this case, η_{EH} is no more monotonic increasing with the equivalent resistor due to the switching of the HI.

$T_{delay} = 20\,\mu s$ and $\alpha = 2$ give the larger power transfer; the η_{EH} comparable but lower than the R_{opt} case, 60%, together with the high value of η_{HI}, 87%, provide an overall efficiency of 52%. $T_{delay} = 5\,\mu s$ and $\alpha = 2$ give the higher η_{EHHI}; the much higher η_{EH} with the slightly lower η_{HI} provide an overall efficiency of 64%.

Comparing the HIs, similar efficiency in transferring the converted power, around 50%, is obtained. However, the electromechanical coupling achieved through optimal resistive load emulation allows the active interface recovering about 80% more power than standard configuration. The proposed HI recovers the 90% of the maximum recoverable power represented by the R_{opt} case.

5.5 Prototyping and testing

With the aim of evaluating the performance of the energy harvesting system equipped with the active interface, several prototypes have been produced and tested.

The device is a $\varnothing\, 27 \times 16\,mm$ cylinder including the transducer, the active interface, the step-counter electronics and the protective shell as described in Fig. 5.1.

In the following, manufacturing details are illustrated and discussed.

5.5.1 Energy Harvester Generator

Structure The structure of the device consists of three plastic elements, Fig. 5.21: the case, the cap and the back-cap. The case is the core part. Its role is to host the moving magnet, the springs and the coils. The cap closes the case and externally protects the coils. The back-cap protects the electronics of the device. The three parts are manufactured through moulding process in NYFLOR, a polyamide reinforced with glass fibre four times stiffer than materials for additive manufacturing and more resistant to the high temperature induced during the soldering on the connection pins. Two L shape connecting pins are co-printed to the case in order to provide a robust structure for the connection of the HI and the coil. The copper wire of the coil is welded to one end of the pins, the PCB of the electronics is welded to the other.
Parts geometries have been studied according to the requirements of the manufacturing design rules, in order to minimise internal stresses and to allow easy mounting. The flat surfaces of the case and of the cap that represent the end-stroke, present two raised circular housing for spring positioning.
After mounting, the case is bonded to the cap by means of epoxy resin in order to drown and protect coils wire and welding points. The backcap is then fixed to protect the PCB and it permanently closes the device. Once closed, the system is inserted in the sole of the shoes.

Coils The two coils, shown together with the case in Fig. 5.22a, are obtained by wounding a copper wire around the guide in the dedicated zones. The two coils are made with the same enamelled copper wire opposite wounded and welded to the side ends of the pins. Its features are external diameter $\varnothing 0.074$ mm and nominal diameter $\varnothing 0.063$ mm. The turns number per coil is 1600. The measured coils overall resistance and inductance are respectively $R = 1204\,\Omega$ and $L = 60.5$ mH.

Springs Due to the very limited stroke available for the magnet oscillation, the elastic characteristic is obtained by means of two conical compression springs. This solution ensures minimal close-wound encumbrance leading to larger available stroke compared to the use of cylindrical springs. Springs are manufactured in INOX steel in order to not interfere with the magnetic field of the floating element.
The smaller diameter end of the springs fits the dedicated housing present in the case and cap. The larger one fits the housing present on the flat surface of the floating

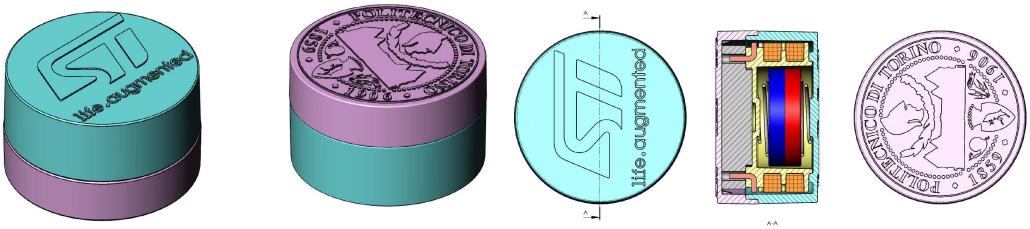

(a)

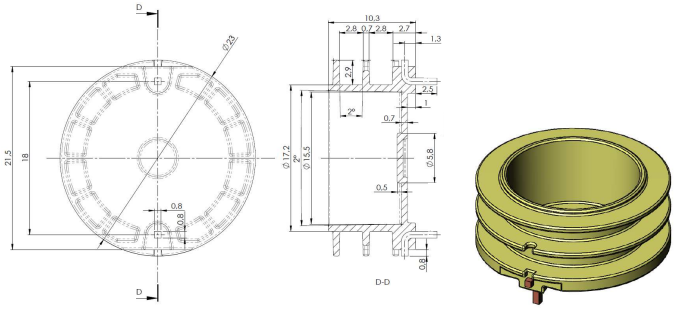

(b)

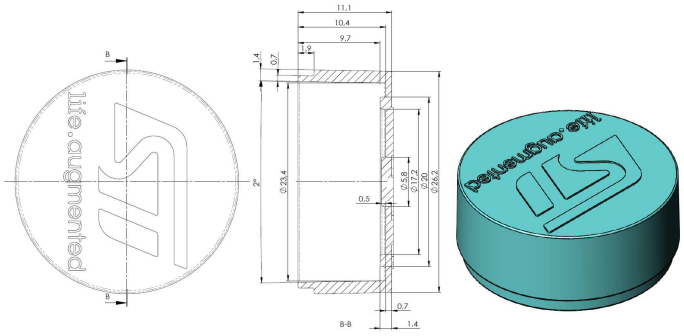

(c)

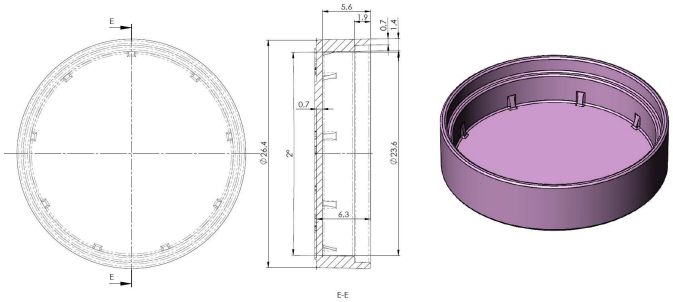

(d)

Fig. 5.21 EH structure. a) Assembly, b) case, c) cap, d) back-cap. (Dimensions are in mm)

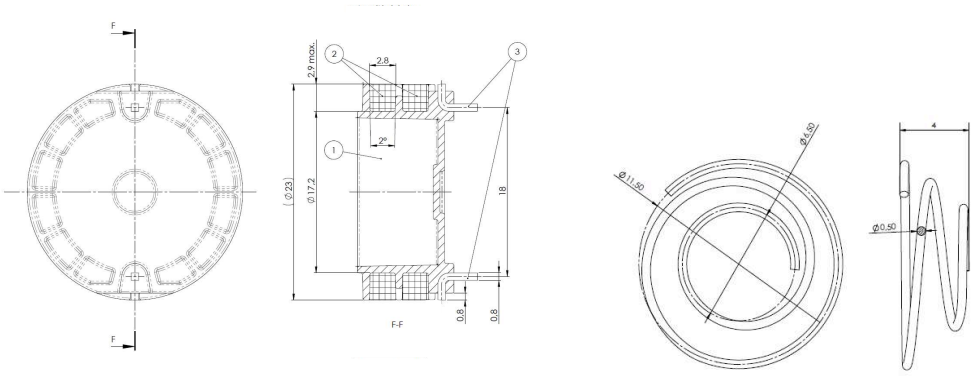

(a) (b)

Fig. 5.22 a) Drawing of the case element (1) with coils (2) and connecting pins (3), and b) drawing of the conical spring. (Dimensions are in mm)

magnet.

Fig. 5.22b shows springs geometrical dimensions. The free length is 4 mm but they are pre-compressed when the magnet is in the equilibrium position. The system stiffness k_m is given by the sum of the two springs stiffness.

The nominal stiffness of each spring is 900 N/m. Trough a best fit procedure, the actual value of the springs stiffness has been evaluated. Experimental transducer voltage when a resistor is directly connected to the coils terminals is compared to numerical results. Fig. 5.23 shows that best-fit is achieved for a stiffness of 1058 N/m per spring. In this condition, the free-oscillation frequency of the model exactly fits experimental evidence. The huge difference between the manufactured springs stiffness and the nominal specification is due to the unexpected strain hardening of the material.

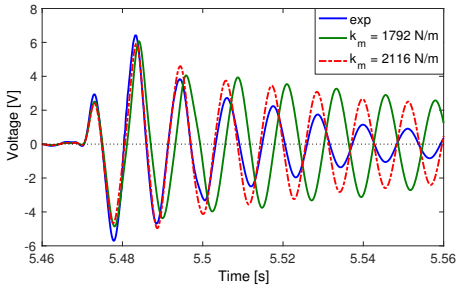

Fig. 5.23 Spring stiffness fitting: experimental vs. numerical V_T.

Magnetic floating mass The magnetic floating element of the system is a cylindrical NdFeB magnet. Due to the strict dimensional constraint imposed, the performance of the device are strongly influenced not only by the its mass and magnetic characteristics but also by its geometrical features. Magnet dimensions, in particular the height, and the available stroke are very conflicting factors and, by means of the optimisation process previously described, the optimal configuration has been derived. A ⌀15×5 magnet results with a corresponding available stroke of 2.7 mm. Even if made of INOX steel, in practical implementation conical springs present a slight magnetisation that causes lateral shifting once mounted on the flat surfaces of the magnet (see Fig. 5.24a). Anomalous behaviour of the system follows causing strong deterioration of performance. In order to overcome this issue, a centring system is required. Two solution are compared. The first consists in bonding on the magnet flat surface a plastic material ring, while the second consists in performing a circular recess.

Fig. 5.24 shows a comparison among the three cases. Plastic rings drastically reduce the available stroke while, conversely, holed solution increase it. Important gain

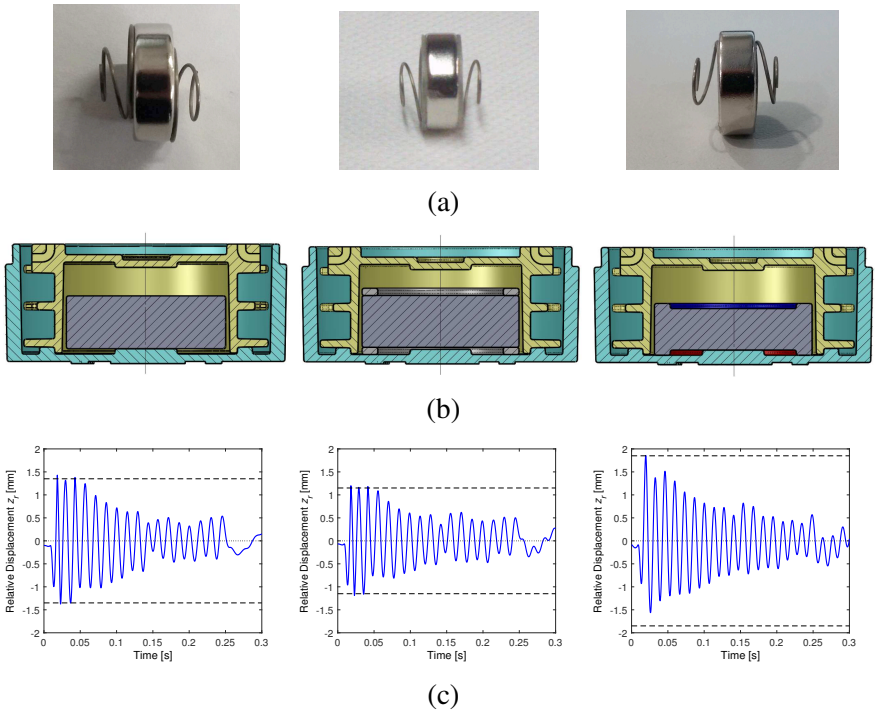

Fig. 5.24 a) Floating magnet with springs mounted, b) available stroke and c) simulated relative displacement during free-oscillation in the case of cylindrical magnet, cylindrical magnet embedded with plastic centring elements and cylindrical magnet with centring holes.

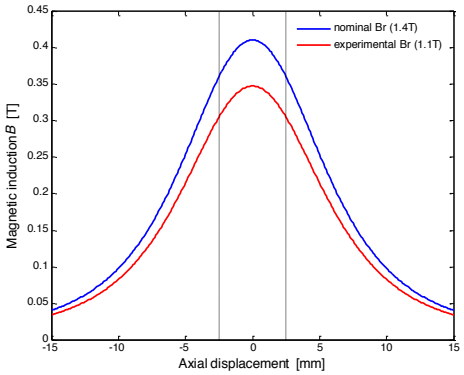

(a)

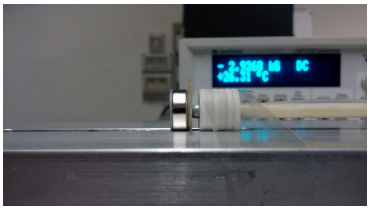

(b)

Fig. 5.25 a) Nominal vs experimental axial magnetic induction and b) measurement setup.

in system dynamics follows. The drawback is a slight reduction of the generated magnetic field and, thus, of the flux linkage. In the following section, experimental outcomes confirm the advantage of the latter solution (see Fig. 5.28b).

The NdFeB magnet employed as floating element presents a nominal residual magnetic induction B_r of 1.4 T. Experimental analysis performed measuring the generated field along the axial direction on a sample of 10 magnets, shows an actual residual magnetic induction of 1.1 T (see Fig. 5.25). This can be related to the worse than expected quality of the magnet or to the measurement procedure itself. Being the diameter of the probe large with respect to that of the magnet, respectively $\varnothing$5 mm and $\varnothing$15 mm, the measure is a mean value over the area around the axis. Since the analytical trend for a fixed distance from the magnet surface present the maximum in correspondence of the axis, a lower value than the real follows.

Friction and air model parameters fitting Trough a best fit procedure, the actual values of the friction model parameters have been evaluated. Transducer voltage when a resistor is directly connected is measured and simulated. Experimental and numerical trends are then compared to derive de best-fit parameter set. Fig. 5.26 shows the procedure result. Satisfactory matching is achieved even if the numerical model results slightly more damped during the last oscillations.

Tests and results Prototype shown in Fig. 5.27a have been tested. Experimental frequency response to a 2 g constant acceleration amplitude frequency sweep,

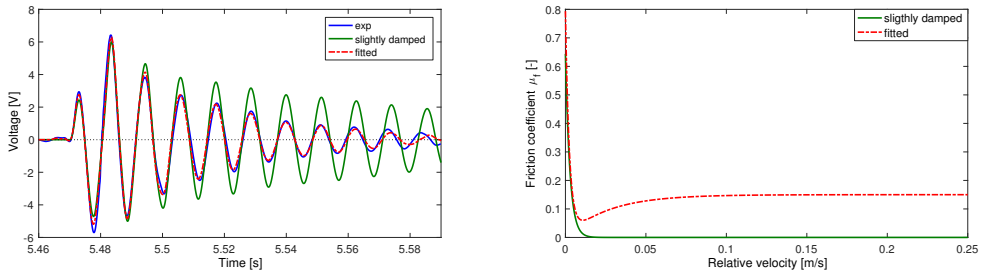

(a) (b)

Fig. 5.26 Friction fitting: a) experimental vs. numerical V_T and b) friction coefficient as a function of the relative velocity.

Fig. 5.27b, shows that the resonance frequency of the system is 87 Hz. Fig. 5.28a illustrates the numerical and experimental voltage V_T in response to the footstep input when a resistor $R_L = R$ is directly connected to the transducer terminals. Very good matching between the two trends can be appreciated.

Fig. 5.28b reports the energy experimentally dissipated/harvested on R_L by the device confirming the effectiveness of the adopted solution for spring centring. Energy recovery performance of 400 µJ are achieved overcoming of more than 4 times the energy target of 90 µJ.

Experimental analysis has been performed on a batch of 15 prototypes. Results are summarised in Fig. 5.29. Performance in terms of harvested energy spreads from a minimum of 260 µJ to a maximum of 530 µJ with a mean value of 385 µJ. Although the huge spread, the energy target is guaranteed. The frequency response

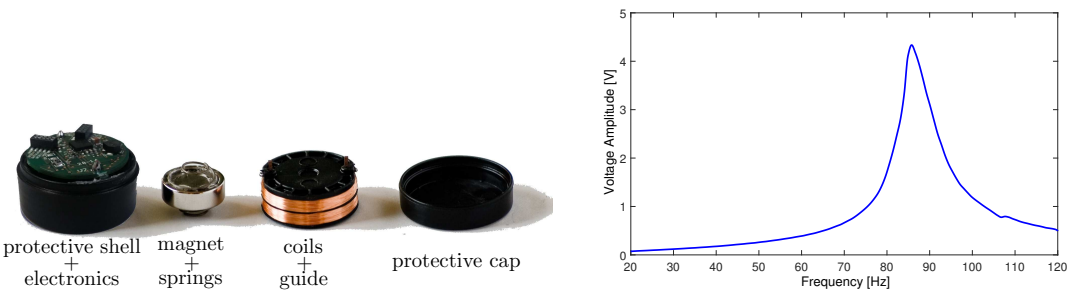

(a) (b)

Fig. 5.27 a) EH prototype and b) experimental frequency response V_T without HI when $R_L = R$.

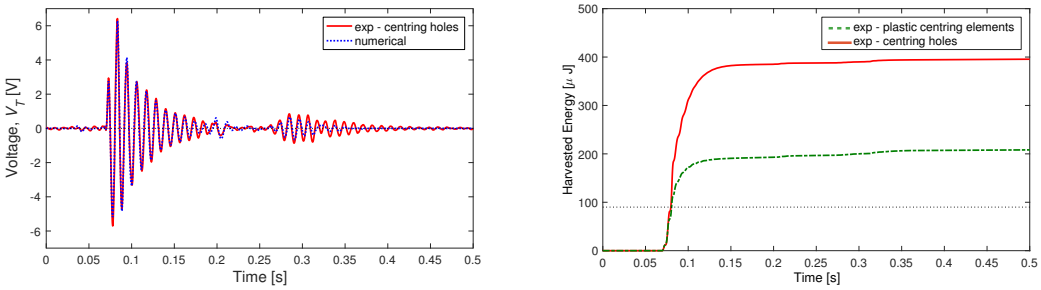

(a) (b)

Fig. 5.28 a) Numerical versus experimental voltage V_T with a resistor $R_L = R$ connected to the transducer terminals in the case of magnet with centring holes. b) Experimental energy harvested on $R_L = R$ in the case of magnet embedded with plastic centring elements and with centring holes. The dotted line indicates the target energy level.

highlights that the different behaviour of the prototypes is due to the high irregularity of the systems stiffness. As expected, the most critical elements of the device are the springs whose manufacturing is responsible of the variable stiffness and wrong magnet centring that causes high friction.

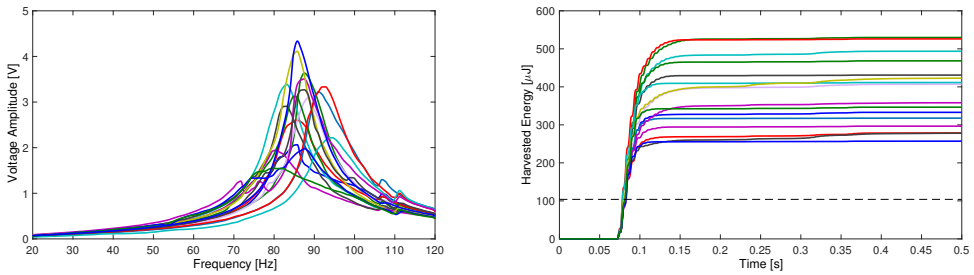

(a) (b)

Fig. 5.29 15 prototypes performance comparison. a) experimental frequency response V_T without HI when $R_L = R$ and b) harvested energy on $R_L = R$. The dotted line indicates the target energy level.

5.5.2 Harvester Interface and step-counter electronics

The electrical part of the system has been developed by STMicroelectronics and implemented on the PCB shown in Fig. 5.31a. In order to minimise electronics encumbrance, electrical components are placed on both sides of PCB. The core elements are the application-specific integrated circuit (ASIC) performing the HI logic and the step-counter electronics (STENH02), and the BlueNRG Bluetooth radio. The ASIC is developed with BIPOLAR-CMOS-DMOS (BCD) 0.35 µm technology. Passives are visible on the PCB. The main passive components connected to STENH02 are $C_{out} = 3.3\,\mu F + 2.2\,\mu F$, $L_{DCDC} = 10\,\mu H$, $C_{DCDC<1>} = 2.2\,\mu F + 1\mu F + 1\,\mu F + 1\,\mu F + 1\,\mu F$ (the first local near the STENH02 chip, the others near the the BlueNRG Bluetooth radio), $C_{DCDC<2>} = 3.3\,\mu F + 1\,\mu F$ (the first local near the STENH02 chip, the other near the BlueNRG Bluetooth radio), $R_{PULLUP(I2C)} = 3.3k\,\Omega$. The developed board does not employ commercial MOSes. The closing time of the SWs is 50 µs while the opening time can vary from a minimum of 10 µs to a maximum of 100 µs depending on the current in the transducer and on the voltage of C_{out}. It follows that the switching time between *energising* and *transferring* phases is not fixed and bounded between 6.6 kHz and 16 kHz.

The main working phases of the device can be summarised as follows. The energy harvested from the mechanical source is accumulated in the storage capacitor and it is used to supply a microcontroller (MCU), and a low power TX/RX radio (BlueNRG) to transmit the footstep count to a remote receiver (see Fig. 5.30). No other sensor is used to detect a foot-step. At each step, the micro-controller connected to the input terminals of the transducer is able to monitor the switching activity of the interface. Observing the characteristics of the interface switching, the alternation of positive and negative transducer polarities and the number of I_{on}-I_{off} cycles, the micro-controller is able to detect the foot-step and turn on the radio for the transmis-

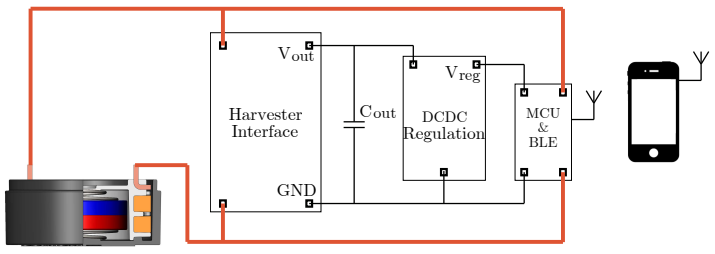

Fig. 5.30 EH system general scheme.

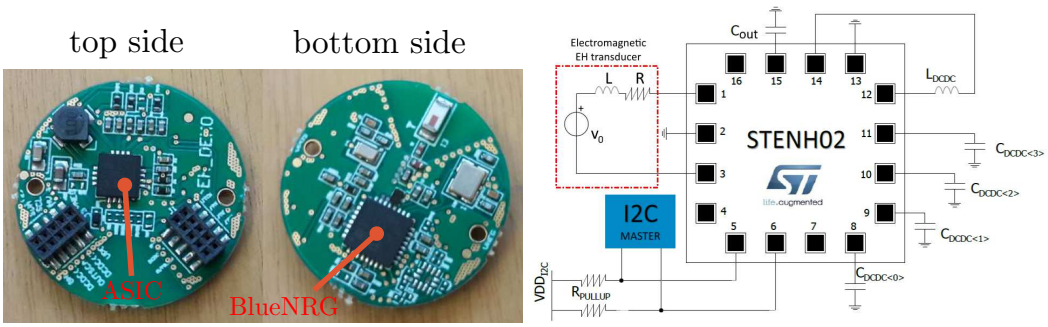

(a) (b)

Fig. 5.31 EH electrical part: a) prototype and b) general scheme.

sion.
The operational phase lasts for about 30 ms with an overall consumption of 87 µJ, namely a power need of about 3 mW. See Fig. 5.32 and Tab. 5.3 for details.

Tests and results Experimental tests have been conducted on the *EH+HI* system. A train consisting of four foot-step profiles simulated in the design phase is reproduced on the shaker. Tests have been conducted substituting the target electronics with a 330 Ω resistor.
Fig. 5.33a shows V_T, V_L and V_{reg} measured during the first step. The output capacitor C_{out} is initially discharged and V_L grows during the first magnet oscillation due to a direct power transfer. After the first oscillation, C_{out} is sufficiently charged to activate the control logic of the HI that begins to operate. The switching activity generates the V_T peaks and allows to continue charging the load capacitor. During this step,

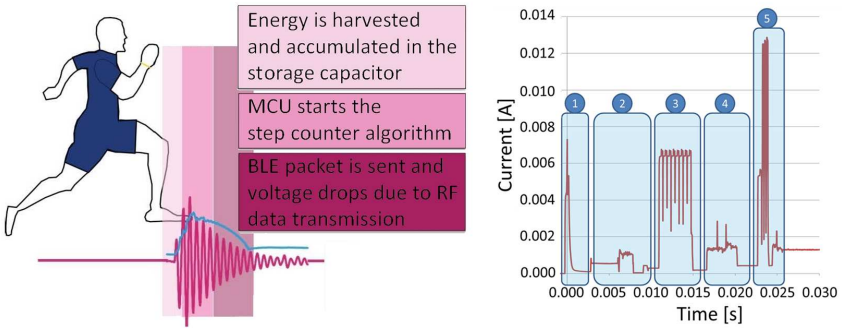

Fig. 5.32 Device general behaviour and load current absorption profile during the different phases of Tab. 5.3.

Table 5.3 Energy demand per foot-step of the step-counter electronics during the different phases.

Phase id.	**Phase description**	**Energy request** [μJ]
1	VDD decoupling cap charging	16
2	STM32 initialisation	5
3	Step counting algorithm	24
4	Bluetooth initialisation	6
5	RF transmission	36
	Total energy consumption	87

a large amount of the harvested energy is spent to initialize the HI electronics. It follows that V_L remains under the voltage level $V_{on} = 5.2$ V. V_{reg} is not activated and no power is transferred to the load resistor.

Fig.s 5.33b and 5.33c report experimental measurements during the second step. Since the beginning the HI operates from the first magnet oscillation. When V_L reaches V_{on}, V_{reg} is activated and the load resistor is supplied with a constant voltage of 1.8 V. At about the half of the third oscillation, the energy balance between the harvested and the consumed energy becomes negative and V_L begins to decrease. When it gets to the voltage level $V_{off} = 4$ V, V_{reg} is switched off and the load resistor is no longer supplied. On the current side, it can be seen that when the HI switches, i_T is the envelope of the trend measured by repeating the test substituting the active interface with the optimal resistor. This demonstrates the effectiveness of the developed active interface in providing the best electromechanical coupling condition while supplying an electric load in DC condition. Zooming a region where the current is above the threshold level $I_{th} = 1$ mA, namely a region where the second switching condition is always satisfied, *energising/transferring* phases can be analysed. *Energizing* phase lasts for 20 μs and the *transferring* phase lasts until the initial current value is halved. The irregular behaviour during the second oscillation indicates an impact of the magnet against the lid. Nevertheless, the trend of V_{reg} shown in Fig. 5.33b proves that the load resistor is power supplied with constant voltage of 1.8 V for about 35 ms. It follows that the device is able to provide about 10 mW for 35 ms, satisfying the power requirement for this application.

Comparing the energy provided by the HI to the resistive load, about 360 μJ, with the energy dissipated on the optimal resistor, about 400 μJ, the effectiveness of the

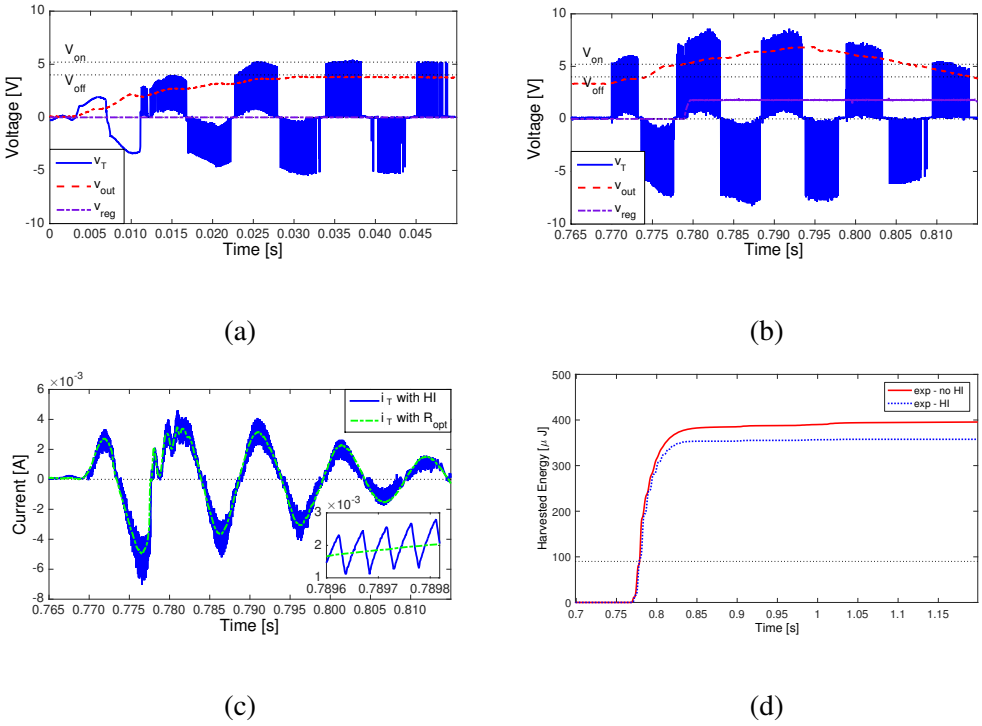

Fig. 5.33 Experimental voltages a) during the first step and b) during the second step, with $\alpha = 2$ and $T_{delay} = 20\,\mu s$. c) Experimental currents during the second step with the HI shown together with the experimental current in optimal resistive load condition. d) Harvested energy during the second step.

proposed active interface is confirmed. The 90% of the maximum recoverable energy is harvested.

In order to take into account performance variations due to the different excitation levels of the foot-steps, the whole acceleration profile measured has been reproduced on the shaker. The energy harvested at each step is reported in Fig. 5.34. Foot-step variation implies a quite huge difference of performance, from a minimum of 316 µJ registered for the 5th step shown to a maximum of 995 µJ for the 13th step, with a mean value of 644 µJ. For each foot-step, energy recovery is larger than the required threshold necessary to perform the data sending.

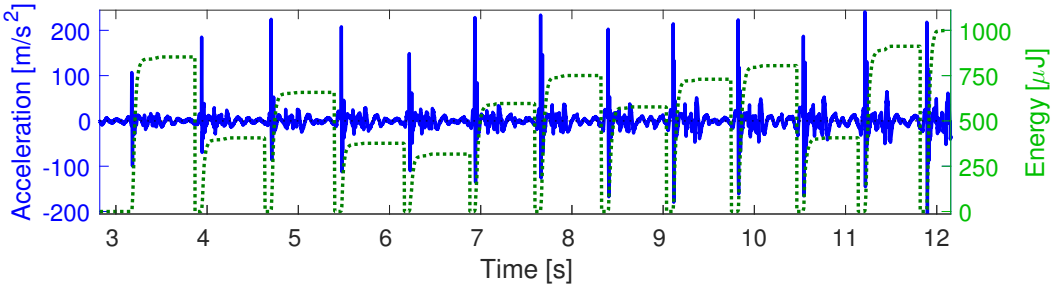

Fig. 5.34 Harvested energy at each foot-step during the whole run.

5.6 Electromagnetic EH conclusions and future developments

In this chapter, the energy harvesting project derived by the partnership between the *Department of Management and Production Engineering* of Politecnico di Torino and the *Analog MEMS Group* of STMicroelectronics has been descibed.
With the aim of power supply a wireless step-counter placed in the sole of a running shoe, a complete EH system has been developed, analysed and tested.
A magneto-inductive transducer performs energy conversion exploiting magnet oscillation due to the impact of the shoe on the ground at each foot-step. A parametric simulation model has been developed, validated and experimentally tuned. *Electrical resistance matching* condition is considered for the design of the transducer. *EDAM* condition is investigated to derive the load resistor that maximises power transfer. This configuration is taken as reference to evaluate system performance. The proposed device is embedded with an input powered HI. Exploiting PWM, the interface allows resistive load emulation while charging the output capacitor independently from its voltage level and from the signal provided by the transducer. The tunability of the HI allows equivalent resistor setting in order to match the optimal value.
Numerical analysis shows that the power recovered by the proposed system is 90% the dissipated on optimal resistive load and two times that of the standard AC-DC interface.
Experimental tests on prototypes confirm numerical results. Considering a sample foot-step, energy recovery is 360 µJ against 400 µJ dissipated on optimal resistor, 90%. Test reproducing the whole run shows that, in spite of variable excitation, at each foot-step energy recovery is higher than the required allowing the step-counter transmitting the information.

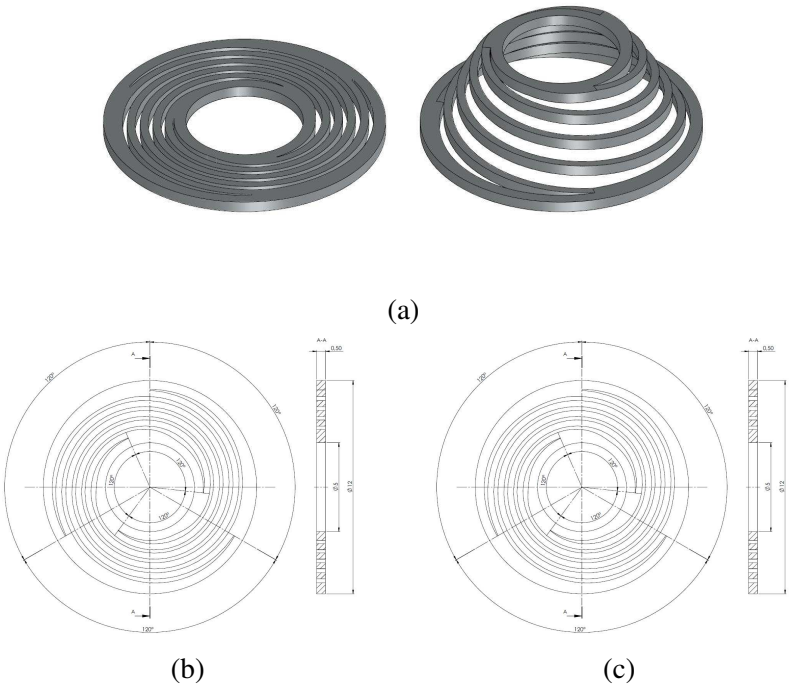

(a)

(b) (c)

Fig. 5.35 Alternative springs for the energy harvesting system for shoes application.

The analysis of a batch of 15 prototypes highlighted that the springs are the weakest point in the manufacturing process. Due to material hardening and anomalous magnet centring, springs affect the system dynamics both in term of frequency response and both in term of friction.

In order to overcome this issue, an alternative spring layout has been considered. The basic idea is to obtain the nominal stiffness through the elastic element shown in Fig. 5.35. It consists in a conical element where two rings, one larger and one smaller, are connected by three 3-spiral beams. Starting from a harmonic steel sheet, the desired geometry is obtained by laser cut process. Through folding process the 3D shape is then derived. Optimising the geometrical parameter, the target stiffness value is set.

This solution, still under investigation, represents an efficient alternative to the employed springs.

Chapter 6

Piezoelectric EH

6.1 Introduction

In the context of the collaboration between the *Department of Management and Production Engineering* and the *Department of Energy* of Politecnico di Torino with the *Matériaux, Machines et Dispositifs Electromagnétiques Avancés* team of the Grenoble Electrical Engineering Laboratory, a piezoelectric EH based on a cantilever beam and embedded with a self-powered HI has been designed, prototyped and experimentally tested on a shaker. The aims are to develop an energy harvesting device targeted to environmental vibrations energy recovery and to tune the numerical model against experimental evidence.
After the design of the mechanical part of the system, model identification has been performed in order to experimentally evaluate system parameters. Subsequently, the HIs described in sec. 4.3.3 have been designed implementing a peak detection technique for switch control directly supplied by the transducer output power. No external source is employed to drive the switch making the device self-powered. Performance of STD, s-SSHI and SECE interfaces are analysed and compared. SECE interface is finally prototyped.
In this chapter, the design and experimental activities carried out are described.

6.2 Mechanical part design

Fig. 6.1 shows the prototyped EH. The device is designed in order to have low resonance frequency, in the range between 40 and 100 Hz. The system consists of a stainless steel support beam clamped between two elements that allow fixing the device to the shaft of a shaker. A Macro Fiber Composite (MFC) piezoelectric patch is bonded on the upper surface and a proof mass at the free-end is obtained by clamping the beam with two magnets in attraction. The piezoelectric element is then connected to the electric interface described in the following section.

Support beam and tip-mass The support cantilever beam is a stainless steel beam which geometrical features are summarised in Fig. 6.2. The beam is 100 mm long, 25 mm wide, 0.5 mm tick, and consists of two parts: a clamped portion of 40 mm that is locked in the shaker fixture and a free portion of 60 mm that represents the effective oscillating elements. The clamped region presents three slots allowing the fixture bolts passing and some positioning adjustment in order to have the piezoelectric patch as close as possible to the joint even in case of imperfect bonding. At the free-end of the beam, three bends, two upward and one downward, ensure the positioning and centring of the proof mass avoiding slipping during vibrations. The beam is manufactured with laser-cut technology, subsequently it is bended at the free-end. Considering standard stainless steel, $E_s = 180$ GPa, the first flexural mode occurs at 109 Hz.
The tip-mass is obtained clamping the free-end of the beam with two $\varnothing\, 15 \times 3$ mm magnets in attraction. It results a cylindrical shape mass of $7.95\,10^{-3}$ kg which

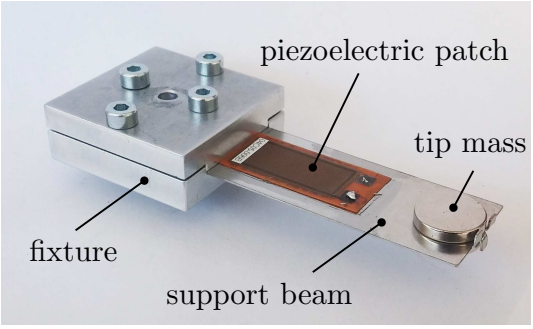

Fig. 6.1 Piezoelectric EH prototype.

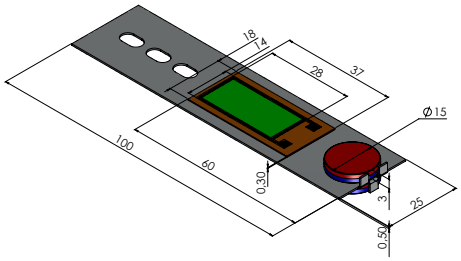

Fig. 6.2 Support beam and tip mass CAD model.

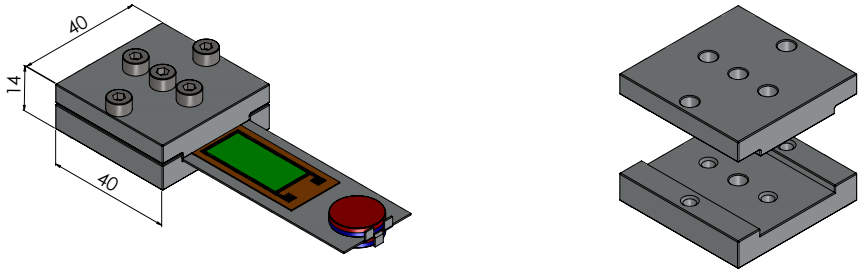

(a) (b)

Fig. 6.3 a) Piezoelectric EH CAD model and b) fastening system detail.

application point on the support beam, with respect to the free-end, is shifted half of the diameters toward the joint. It follows a shorter effective oscillating length of the support beam.
The first flexural mode of the system is at 56 Hz, that falls in the frequency range of interest.

Fixture In order to fasten the support beam to the excitation stem of the shaker, a fixing system has been developed, Fig. 6.3. The system consists of two aluminium elements that clamp the support beam by means of four bolts. The lower element presents a groove to host the beam avoiding rotation around the vertical axis and translation along the transversal one. The air gap between the upper and lower element in the lateral regions ensures that the clamping is performed acting only on the beam avoiding rotations and translations along the remaining axes. The clamping, performed on the 40% of the beam length, ensures a good approximation of a fixed-end. A central through hole allows screwing the fixing system to the shaker stem. The overall size of the mechanism is 40×40×14 mm and it weights 0.062 kg.

Piezoelectric patch The piezoelectric element bonded on the support beam is a patch of Macro Fiber Composite. Developed at NASA Langley Research Center during the late 90's, nowadays the MFCs are commercial products widely used.
In a MFC patch, rectangular, uni-axially aligned piezoelectric fibres are sandwiched between layers of adhesive and electrode polyimide films Fig. 6.4a. Different types of MFC patches exist. The employed one is the P2 type *M-2814-P2*, see Fig. 6.4c. The patch exploits PZT fibres with top and bottom electrodes obtained by dicing metallised PZT wafers. All finger electrodes of each side are connected together. Thus, the electric field is applied through the fibre thickness, see Fig. 6.4b. For further details refers to [108]. The P2 type MFC especially suits for energy harvesting applications due its higher capacitance and charge generation ability when compared with other types at the same strain level. The elastic modulus along fibres direction is $E_1 = 30\,\text{GPa}$ while the clamped capacitance is $C_p = 26.6\,\text{nF}$ and the piezoelectric coupling coefficient is $d_{31} = 210\,10^{-12}\,\text{C/N}$. The drawback of MFC patches is that the active piezoelectric area is smaller than the overall area occupied on the support beam. The considered layer dimensions are 37×18 mm while the active area is 28×14 mm. It follows that, when the patch is bonded, the active area remains shifted with respect to the fixed-end and, thus, the support beam curvature is not exploited where it is maximum.

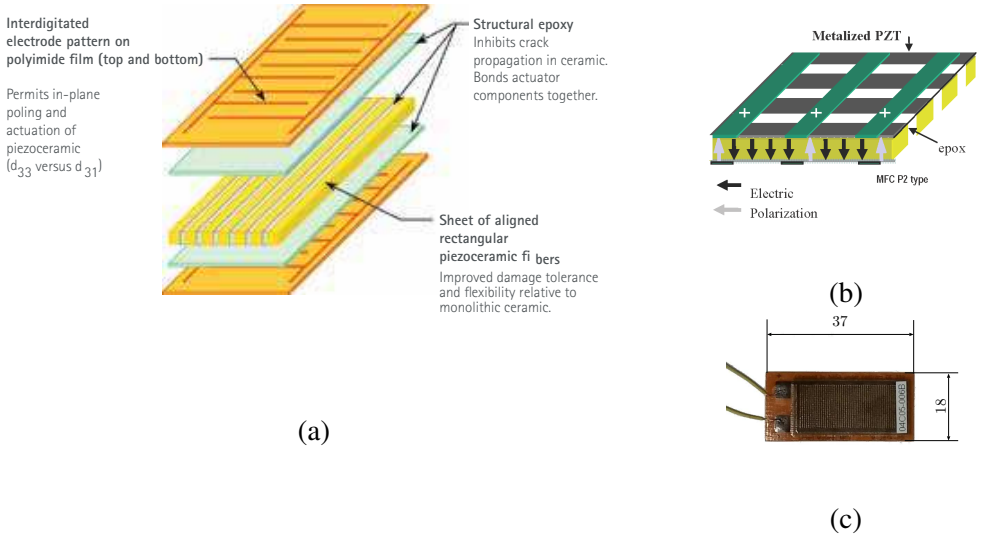

Fig. 6.4 a) Schematic structure of the MFC, b) P2 type and c) *MFC M2814-P2* patch with dimensions in mm.

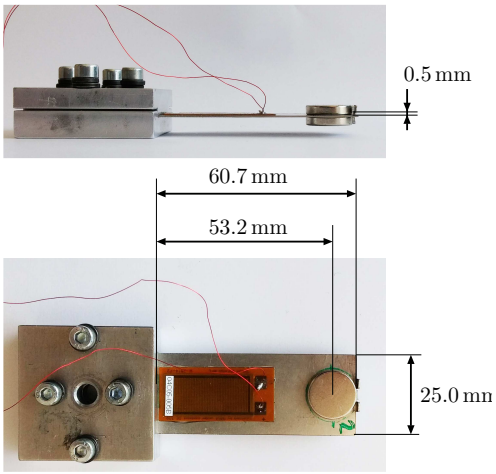

Fig. 6.5 Piezoelectric Energy Harvester.

Model identification

Fig. 6.5 illustrates the EH system with its geometrical characteristics experimentally evaluated. In the following, experimental model identification performed to identify the parameters of eq. 4.40 (m, k, c, α, β) is described.
Due to the piezoelectric element employed, model parameters cannot be simply derived from geometrical and material properties. However, the structure still presents the features of the piezoelectric electromechanical device described in sec. 4.3.

Experimental setup The experimental setup used for the model identification is based on the *LMS TestLab* system and it is shown in Fig. 6.6. A *Dongling ESD-045* shaker controlled in position reproduces the acceleration profile of the mechanical input imposed to the fixed-end of the harvester. An uni-axial accelerometer placed on top of the fixture allows closing the control loop. A *HGL-Dynamics OptoMET Laser Doppler Vibrometers* measures the displacement, velocity and acceleration of the tip-mass while voltage signals are directly acquired by *LMS TestLab*.

Preliminary tests A preliminary series of test has been conducted in order to evaluate the experimental setup. Constant base acceleration amplitude sweeps in frequency are performed considering the only support beam, the support beam em-

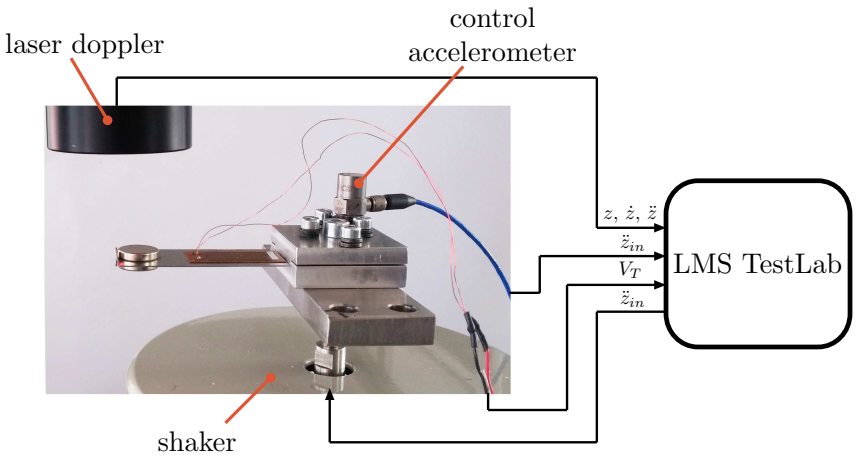

Fig. 6.6 Experimental setup.

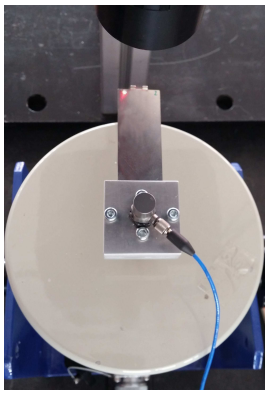

(a)

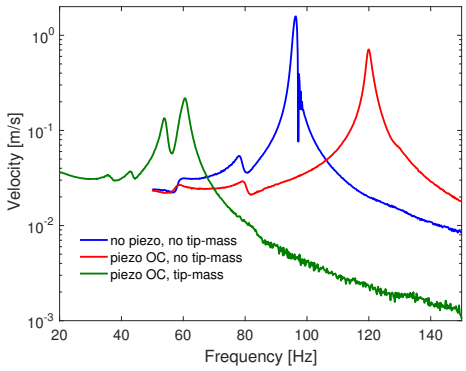

(b)

Fig. 6.7 Preliminary tests: sweep response.

bedded with the piezoelectric patch and the the support beam embedded with the piezoelectric patch and the tip-mass. Response velocity is measured in all the three cases in correspondence of a lateral extreme of the free-end of the support beam in order to consider also the torsional behaviour, Fig. 6.7a. Fig. 6.7b shows the result. According to what expected, the three curves present a main peak at about 100 Hz in the case of the only support beam (blue curve), more than 100 Hz when the piezoelectric patch is added (red curve), and about 60 Hz when the beam is embedded with the tip-mass (green curve). However, in the first two cases an unexpected trend is present between 60 and 80 Hz, and additional lower frequency peaks appear in the third case.

A deeper analysis conducted repeating the sweep test mounting the fixing mech-

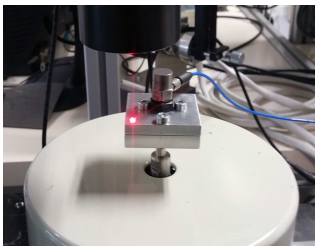

(a)

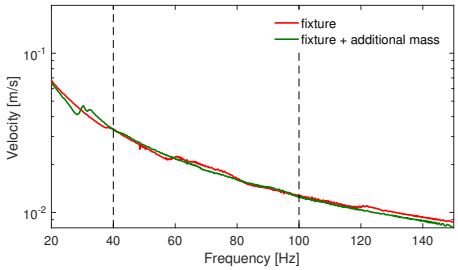

(b)

Fig. 6.8 Fixture frequency response.

anism without the beam on the shaker, shows that these anomalies are due to interference between the vibrating modes of this structure and the bending of the beam. Fig. 6.8b shows the frequency response of this system measured as shown in Fig. 6.8a. The red curve highlights that in the frequency range of interest, 40-100 Hz, a behaviour that interferes with the simple bending of the beam is present. By adding an additional mass at the bottom of the fixing mechanism (blue curve) the behaviour at lower frequency is worsen but in the range of interest the interference is avoided. As demonstrated in the experimental graphs shown in the following paragraphs, no more undesired behaviours are present in the frequency range of interest.

Support beam material identification The identification of the material of the support beam has been conducted against experimental results. A cantilever beam made with the same material of the support beam has been tested. The dimensions of the oscillating part are 59.0×23.7×0.5 mm.

The material density, ρ_s, has been evaluated from the measures of volume and weight. A density of $7.729\,10^3$ kg/m^3 results and, thus, the mass of the oscillating part is $5.9\,10^{-3}$ kg. The Young's modulus, E_s, has been identified by matching the resonance frequencies of a FEM and a continuum model of the beam (respectively red and black lines in Fig. 6.9) with experimental evidences. Experimental tests are performed considering a 2 m/s^2 constant base acceleration amplitude frequency sweep and the Fast Fourier Transform (FFT) of the free oscillation of the beam in response to non-zero initial conditions ($z_r \neq 0$ is imposed). Beam response is measured in correspondence of a lateral extreme at the free-end in order to appreciate also torsional behaviours.

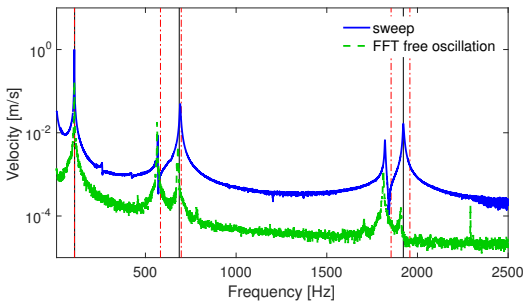

Fig. 6.9 Support beam identification.

Fig. 6.9 reports the experimental frequency response. The blue and the green curves respectively represent the sweep response and the FFT. Satisfactory correspondence between experimental and numerical results is achieved for an elastic modulus of 172.2 GPa. The first, the third an the fifth vibrating modes are the three first flexural modes identified by the two models. The second and the fourth are torsional modes and thus analytically identified only by the FEM model. A huge distance, about 400 Hz, separates the first and the second mode shapes.
Material proprieties are in accordance to what expected for a stainless steel and they suggest that the support beam is made of AISI Type 302 Stainless Steel.

Piezoelectric equivalent beam identification Fig. 6.10a shows the support beam embedded with the MFC piezoelectric patch. Due to the proprieties of the MFC patch employed, an equivalent beam is considered assuming the same geometry of the oscillating part of the support beam. Density and Young's modulus are evaluated as in the previous paragraph.

The equivalent beam density, ρ_{seq}, has been evaluated considering the volume of the support beam and the weight of this plus the piezoelectric patch. Density of $9.159\,10^3$ kg/m^3 results. Young's modulus is evaluated as in the previous case through sweep tests performed considering OC and SC condition of the piezoelectric patch. As expected, in OC the structure is stiffer than in SC due to the *spring behaviour* of the clamped capacitance of the MFC patch. Fig. 6.10a highlights a 1.2 Hz shift between the two cases. As the aim is the evaluation of only the mechanical characteristics, the Young's modulus E_{seq}, is set by matching the first flexural mode frequency of the numerical models against the experimental result in SC. Satisfactory correspondence is achieved for an equivalent elastic modulus of 259.1 GPa.
By comparing E_s and E_{seq}, it is evident that, in this case, the behaviour of the support

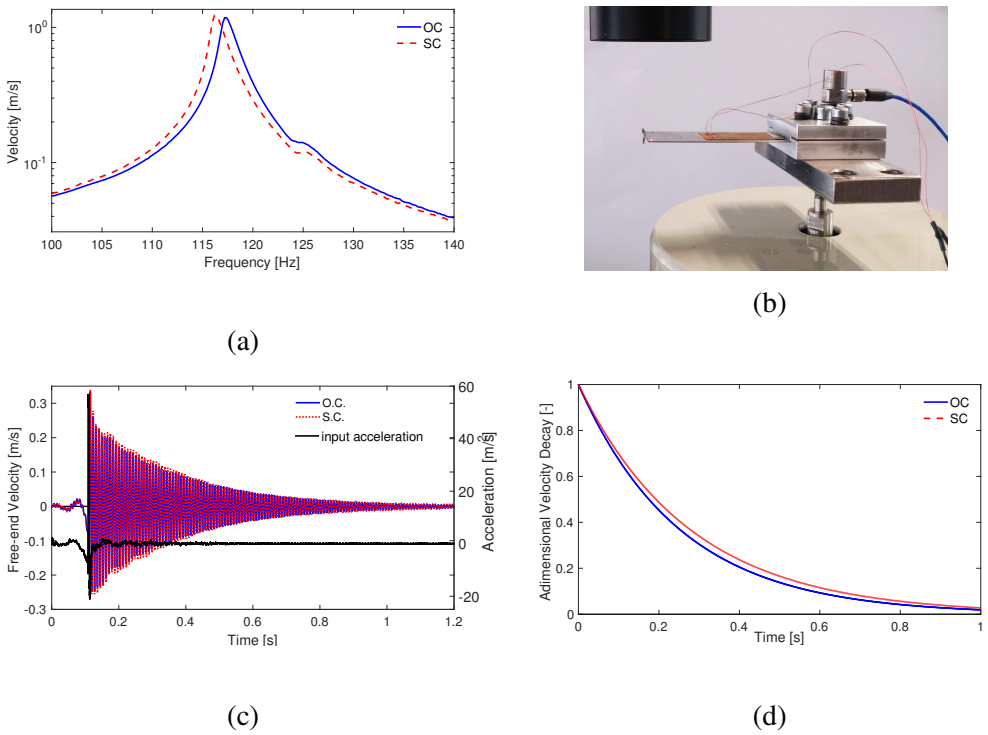

Fig. 6.10 Piezoelectric beam experimental identification.

beam is heavily influenced by the presence of the piezoelectric patch. The induced difference is about 90 GPa and the frequency of the first flexural mode shifts from 99.0 to 116.2 Hz.

Impulsive test are performed in order to evaluate the damping effect induced by the electrical losses. Impulsive acceleration profile is imposed to the fixture and the free oscillation is compared in open and short circuit, Fig. 6.10c. The envelope of the oscillation is proportional to $e^{-\frac{t}{\tau}}$ where $\frac{1}{\tau}$ is the exponential damping coefficient representing the rate of exponential decay. Velocity responses are normalised with respect to the maximum value registered in each condition. The positive envelope is plotted in Fig. 6.10d. From measurement, $\frac{1}{\tau}$ equal to 3.765 s^{-1} and 3.596 s^{-1} respectively in OC and in SC condition is derived. In SC, as no mechanical energy is converted into electrical, the oscillation decay is due exclusively to the mechanical dissipation of the structure. Conversely, a more damped structure is observed in OC, indicating that, in addition to the mechanical losses, the mechanical energy converted into electrical is not entirely returned to the mechanical system but partially dissipated.

EH mechanical parameters identification The mechanical parameters of the model describing the energy harvesting system shown in Fig. 6.5, eq. 4.40, are evaluated as follows. Fig. 6.11 shows the tests performed.
The mechanical stiffness of the system, or the stiffness in short circuit, $k = k_{SC}$, is calculated considering the equivalent piezoelectric beam, which density and Young's modulus have been identified in the previous paragraph. Beam geometry is assumed to be 53.2×25.0×0.5 mm, where the length is from the fixed-end to the centre of the mass. k_m of 1336.9 N/m derives.
Frequency sweep test is performed in short circuit condition. 2 m/s^2 constant base acceleration amplitude is applied. The mass of the model is derived from the resonance frequency, eq. 4.58. $\omega_{SC} = 55.68$ Hz and m equal to $10.92\,10^{-3}$ kg results.
The mechanical damping ratio, or the damping in short circuit, c_{SC}, results from the fitting of the response amplitude of the model against the experimental trend. $c_{SC} = 0.06786$ Ns/m derives.
Analogous sweep test is performed in open circuit. Open circuit stiffness k_{OC} due to the mechanical and electrical behaviour, eq. 4.59, is derived from the resonance frequency $\omega_{OC} = 56.20$ Hz, eq. 4.61. Again, the OC damping c_{OC} results from a fitting procedure. $k_{OC} = 1362.1$ N/m and 0.06947 Ns/m derive.
Damping coefficients are also evaluated through impulsive tests. As in previous analysis, impulsive acceleration profile is imposed to the fixture and, from the envelope of the free-oscillation, the exponential damping coefficient is derived. The damping ratios and the damping coefficients derive from:

$$\zeta_{SC} = \frac{1}{\tau_{SC}\omega_{SC}} = 0.00744 \tag{6.1}$$

$$c_{SC} = 2\zeta_{SC}\sqrt{km} = 0.05683\,\text{Ns/m} \tag{6.2}$$

$$\zeta_{OC} = \frac{1}{\tau_{OC}\omega_{OC}} = 0.00880 \tag{6.3}$$

$$c_{OC} = 2\zeta_{OC}\sqrt{k_{OC}m} = 0.06786\,\text{Ns/m} \tag{6.4}$$

Results show that in this condition the system is less damped. Damping coefficient are about 20% lower than in the case of harmonic excitation. Tab. 6.1 summarises the model parameters.
According to eq. 4.41, θ is equal to 0.43, indicating that the mass of the beam participates for its 43% at the dynamics of the system.
Damping coefficient resulting from sweep test is considered. In order to take into

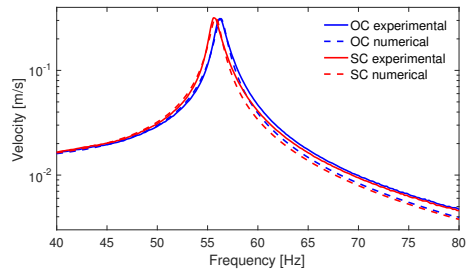

(a)

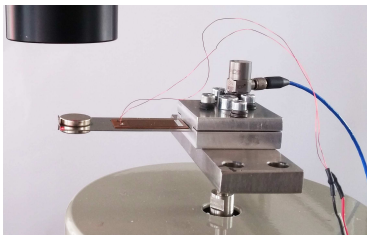

(b)

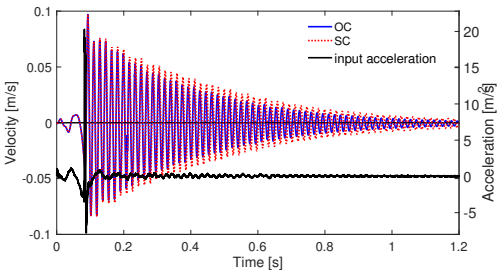

(c)

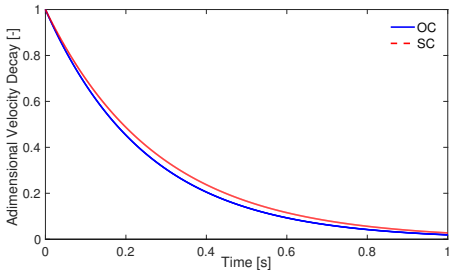

(d)

Fig. 6.11 EH mechanical parameters identification.

account dielectric losses, the damping value considered is the open circuit one, $c_m = c_{OC}$.

Considering the Young's modulus of the support beam material, k_m can be decomposed according to eq. 4.44 in the contribution due to the stainless steel beam, $k_s = 888.5\,\text{N/m}$, and due to the bonded piezoelectric patch, $k_{peq} = 448.4\,\text{N/m}$. It is worth noting the heavy stiffness increase introduced bonding the piezoelectric patch, about 50%.

The difference between k_{OC} and k_m, eq. 4.59, gives the equivalent stiffness due to the clamped capacitance of the piezoelectric element, $k_{el} = 25.1\,\text{N/m}$.

The effective coupling factor of the system k^2 derived from eq. 4.63 results 0.0184 while the global electromechanical coupling figure of merit $k^2 Q_m$ is 1.0465. Considering the frequency response of Fig. 6.11a discrepancy between the experimental and numerical trend can be noted outside the resonance peak. Experimental trends (continuous lines) are always higher than the respective numerical (dotted lines). Being the numerical model SDOF, it is able to well describe the experimental trend around the first resonance frequency, while leaving this condition discrepancy increases.

EH electromechanical coupling parameters identification The direct coupling coefficient β has been evaluated in steady state condition following the procedure proposed in [58]. A short circuit configuration is emulated by connecting the piezoelectric patch terminals to a low resistor, $R_L = 110.5\,\Omega$, as shown in Fig. 6.12a. The electrical feedback on the mechanical part αV_T is almost cancelled. The load resistor impedance is at least two orders of magnitude lower than that of the clamped capacitance at the involved frequencies and, thus, the current through C_p is negligible. The induced current $\beta \dot{z}_r$ flows almost entirely through the load resistor so that:

$$i_T = \frac{V_T}{R_L} \cong \beta \dot{z}_r \Rightarrow \beta = \frac{V_T}{\dot{z}_r R_L} \tag{6.5}$$

Measuring the amplitude of the output voltage V_T and of the mass relative velocity $\dot{z}_r$, the direct coupling coefficient β is derived. Vibrating mechanical input is applied at the short circuit resonance frequency ω_{SC} considering two acceleration amplitude levels, 0.5 and 0.8 m/s^2. Two slightly different values derive for the direct coupling coefficient, difference lower than 3%. The mean value is considered and $\beta = 7.993\,10^{-4}$ As/m results.

The reverse coupling coefficient α has been evaluated considering the definition of k_{el}, eq. 4.60:

$$\alpha = \frac{C_p k_{el}}{\beta} \tag{6.6}$$

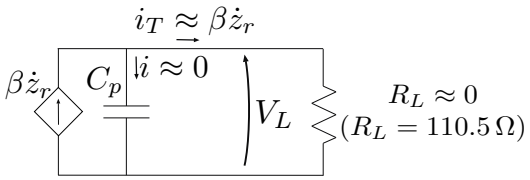

(a)

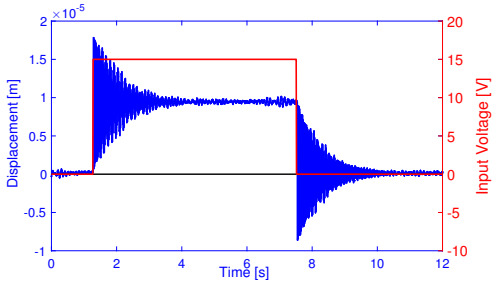

(b)

Fig. 6.12 a) Electric scheme for β coefficient evaluation. b) Mechanical response to imposed voltage.

Table 6.1 Piezoelectric EH model main parameters.

m	Tip-mass	$10.9g$
c_m	Mechanical damping coefficient	$0.06947\frac{kg}{s}$
k_m	Spring stiffness	$1336.9\frac{N}{m}$
$f_{SC} - f_{OC}$	Short and open circuit natural frequency	$55.68 - 56.20Hz$
ζ	Mechanical damping ratio	0.00901
$\beta - \alpha$	Forward and reverse coupling factors	$7.993\,10^{-4}\,\frac{As}{m} - 8.386\,10^{-4}\,\frac{N}{V}$
C_p	Piezoelectric patch clamped capacitance	$26.6nF$
k^2Q_m	Global electromechanical coupling figure of merit	1.0465

$\alpha = 8.353\,10^{-4}$ N/V results. A second evaluation of α has been performed considering static condition in order to cancel the direct piezoelectric effect. Constant voltage is applied to the transducer terminals. The first of eq. 4.40 becomes:

$$kz_r + \alpha V_T = 0 \Rightarrow \alpha = \frac{kz_r}{V_T} \tag{6.7}$$

and by measuring the mass displacement z_r at equilibrium, α is derived. When $V_T = 15$ V is applied, $z_r = 9.4447\,10^{-6}$ m is measured and $\alpha = 8.418\,10^{-4}$ N/V follows. The difference between the two values obtained for α results lower than 1%. The mean value $\alpha = 8.386\,10^{-4}$ N/V is considered.

EH mechanical model For the sake of clarity, the result of the model identification is summarised in Tab. 6.1.

6.3 Harvester interface design

The electric interfaces described in section 4.3.3 have been implemented in order to be fully self-powered interfaces.
The standard full-wave bridge rectifier is a passive design and, thus, it can be considered a fully self-powered interface. As shown in Fig. 6.13, the STD interface consists of four 1N4004 diodes for the bridge rectifier and a 10 µF regulation capacitor to filter the output voltage.

Conversely, sSSHI and SECE techniques are based on the control signal that

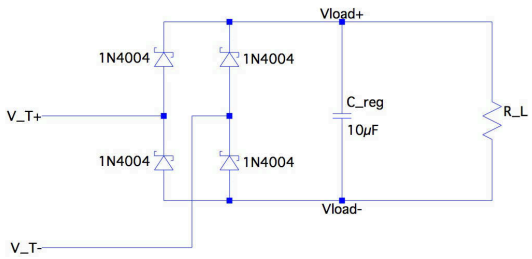

Fig. 6.13 STD HI electrical scheme.

drives the switch and allows voltage inversion or clamped capacitance discharging. Therefore, in order to make the interface electrically autonomous, there should be a self-powered electronics that generates the control signal, Fig. 6.14. As the switching operation has to be synchronised with the mass oscillation, the electronics must be able to sense the vibration behaviour and provide the real-time signal that drives the switch. At the same time, the switching signals has to be generated with ultra-low power consumption in order not to spend for the control an important part of the recoverable energy. To control the switches, mass displacement or velocity signal is required, and the best way to sense them is to exploit the piezoelectric element itself. According to the operative condition, the transducer voltage or the outgoing current may be proportional to the mass displacement or velocity. In open circuit the piezoelectric patch voltage is proportional to the mass displacement, while in short circuit the output current is proportional to the mass velocity. Choosing mass displacement or velocity signal as criterion to control the switching operation implies implementing different electronics. Several control electronics have been proposed basing on two main control loops [77].

In order to exploit the displacement signal, a *peak detector* is used to sense the

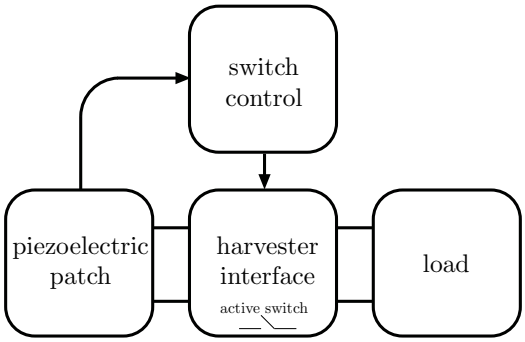

Fig. 6.14 Piezoelectric EH embedded with self-powered synchronized switching interface.

extremes of the mass oscillation through V_T. The control circuit consists in a switch, a comparator and a voltage envelope detector.
In order to exploit the velocity signal, a *zero-crossing detector* is used to detect the extremes of the mass oscillation by sensing the zeros of the velocity through i_T. In this case, as the outgoing current is not proportional to the velocity because the piezoelectric element is not in the short circuit state, a phase compensation must be performed. To avoid the phase compensation, additional piezoelectric patches can be bonded on the support beam. In this case, the control circuit consists of three parts. Velocity is sensed through a conditioning circuit connected to one additional piezoelectric patch. A comparator, power supplied by a third piezoelectric patch, performs the zero-crossing detection and generates the pulse signal that drives the switches.
In s-SSHI and SECE techniques, current flows to the load only during the brief time interval when the switch is closed, thus, the piezoelectric element is mostly in OC state. Transducer voltage directly represents mass displacement and the peak detector well suits to drive the switching. In the following, only the peak detector is described. For further details about zero-crossing detector see [77, 49, 109, 110].

Peak detector The peak detector detects mass displacement extremes through the transducer voltage peaks. Peak detection is performed through the electronic breaker proposed by [111] and illustrated in Fig. 6.15. It consists in a switch, a comparator and an envelope detector. By comparing the actual piezoelectric voltage with its envelope the peak is detected and the switch activated. The energy consumption of this circuit is very limited, approximately the 5% of the electrostatic energy available on the piezoelectric element.

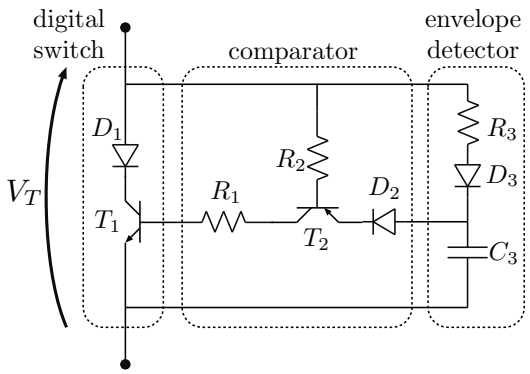

Fig. 6.15 Electronic switch on maxima.

For the sake of simplicity, in working principle description let's assume ideal diodes and positive piezoelectric voltage. The envelope detection of the input signal is performed by R_3, D_3 and C_3. In the beginning, capacitor C_3 is charged by the piezoelectric voltage through the path R_3-D_3-C_3. Due to voltage drop across R_3, voltage on capacitor C_3 is slightly lower than V_T and the emitter-base polarization of the transistor T_2 is reverse bias. The transistors T_2 and T_1 are both blocked. When the voltage peak is reached and V_T begins to decrease, voltage on C_3 remains constant at the peak value of V_T because D_3 prevents discharging. Once the difference between the capacitor voltage and V_T reaches the threshold voltage of T_2, it starts conducting. Due to D_3, C_3 discharges through the path D_2-T_2-R_1-T_1 unblocking the transistor T_1 and thus closing the switch of the interface. The clamped capacitor of the piezoelectric element is connected to the inductor and the L-C_p resonance begins. When the outgoing current i_T reaches zero again, corresponding to the inversion of voltage, the diode D_1 disconnects the inductor. The capacitor C_3 is totally discharged. As this peak detector allows the current flowing only in one direction, in the case of s-SSHI, Fig. 4.12, the switch S is obtained combining two parallel peak detectors in opposite direction, one for the positive voltage peak and one for the negative. In the case of SECE, Fig. 4.13, being S downstream the rectifier, a single peak detector is sufficient. In this case, the voltage inversion process is naturally stopped by the rectifier when V_T reaches zero.

s-SSHI The s-SSHI interface has been modelled implementing the scheme proposed in [68]. This configuration is an improved version of the topology proposed in [111] where the electronic breakers previously described are directly applied. The implemented s-SSHI enhances the switching performance by minimising the interference among the different parts of the circuit and, by removing some resistive components, diminishes the energy dissipation due to the switching processes.
Fig. 6.16a presents the electrical scheme of the s-SSHI.

Two electronic breakers are present, one for the switching at maximum voltage/displacement and one for the switching at minimum voltage/displacement. Transducer voltage rectification is performed exploiting the two diodes of the switches and two additional diodes.
For positive maximum switching, R_1, D_1 and C_1 form the envelope detector. T_1 and T_2 are cut off while V_T increases. At maximum, the voltage across C_1 is $V_{C_1} = V_{T\,MAX+} - V_D$, where V_D is the forward voltage drop of a diode. After the peak,

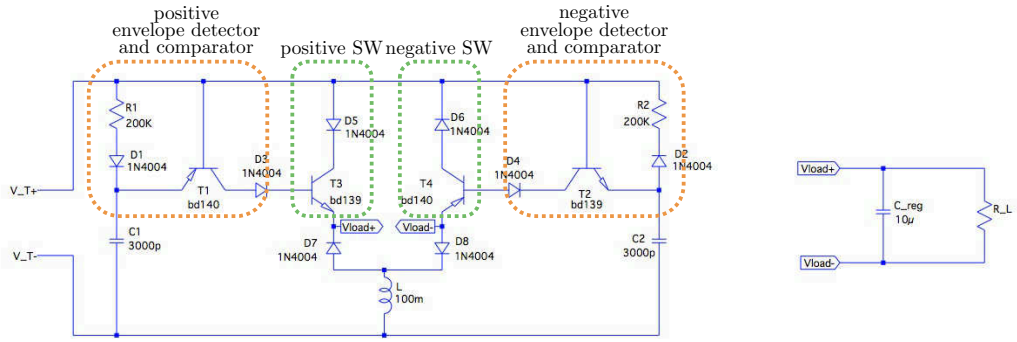

(a)

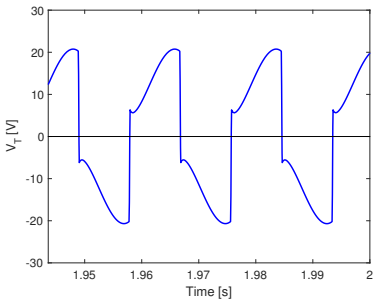

(b)

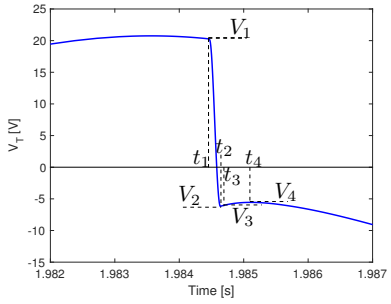

(c)

Fig. 6.16 sSSHI technique: a) electrical scheme and b)-c) V_T in response to 2 m/s^2 56.2 Hz sinusoidal input with $R_L = 50\,\text{k}\Omega$.

V_T decreases. When the drop reaches $V_D + V_{BE}$, where V_{BE} denotes the threshold voltage of a transistor, $V_T = V_1$ and T_1 conducts ($t = t_1$). C_1 begins discharging through the path T_1-D_3-$T_{3(BE)}$-*load*-D_8-L, making T_3 conduct. The inductive path D_5-$T_{3(CE)}$-*load*-D_8-L is unlocked. C_p is connected to L and rapidly discharges reaching the local minimum V_2 ($t = t_2$). Through D_2-R_2, also C_2 is connected to the inductive path and discharges. At t_2, the current through the induction path tends to reverse its direction but is blocked by D_8 and D_5. As the transistor T_4 is cut off, a small and uncharged parasitic capacitance in present across emitter and collector. Thus, for a very brief time interval, the current flow is reversed through the D_7-*load*-$T_{4(CE)}$-D_6 until the parasitic capacitance of T_4 is charged and $V_T = V_3$ ($t = t_3$). The local minimum may interfere with the desired behaviour of the negative breaker, making it recognise an undesired peak. Therefore, resistor R_2 is necessary because ensures that C_2 discharges slower than C_p skipping the local minimum and preventing interference between inversion process and switching operation. After t_3,

the load is disconnect as both T_3 and T_4 are cut off. C_2 continues discharging flowing charges toward C_p and C_1 until they have the same voltage, V_4, slightly higher than V_3 ($t = t_4$). The half cycle of voltage minimum detection begins. The principle is similar to the described above.
As in the case of STD interface, 1N4004 diodes are considered. A 100 mH inductor performs the voltage inversion. BD139 NPN and BD140 PNP transistors are considered respectively for T_2, T_3 and for T_1, T_4. 1000 pF capacitors are employed in the envelope detectors while a 10 µF regulation capacitor filters the output voltage.
An inversion time of 0.24 ms and an inversion coefficient of 0.3 derive.

SECE Fig. 6.17a illustrates the electrical scheme of the modelled SECE interface. The switch is downstream the bridge rectifier. Here the voltage is always positive and, thus, a single electronic breaker is sufficient. When V_T reaches the maximum, C_p is connected to L and voltage inversion begins. The process is naturally stopped by the bridge rectifier when $V_T = 0$, namely when the piezoelectric capacitance is completely discharged. L is disconnected and the transducer is again in OC. The energy accumulated on the inductor is transferred to the load.
A 1000 pF capacitor is used for the envelope detector, a BD140 PNP transistor for

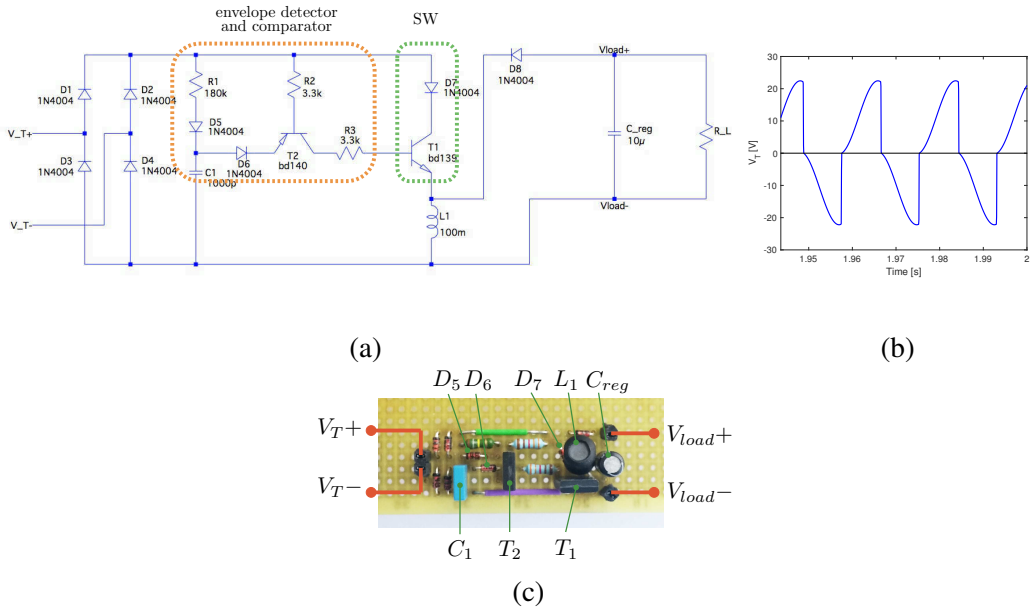

Fig. 6.17 SECE technique: a) electrical scheme, b) V_T in response to 2 m/s^2 56.2 Hz sinusoidal input with $R_L = 50$ kΩand c) prototype.

the comparator and a BD139 NPN transistor for the switch. All the diodes are 1N4004. Piezoelectric capacitance is discharged through a 100 mH inductor. A 10 µF regulation capacitor filters the output voltage. Fig. 6.17c shows the prototyped interface.
A discharging time of 0.13 ms derives.

6.4 Simulations and test

The piezoelectric EH embedded with the STD, the sSSHI and the SECE interfaces have been simulated and compared.
A vibrational input $\ddot{z}_{in}$ of 2 m/s^2 at the open circuit resonance frequency, 56.20 Hz, is considered and different resistive loads are applied. Fig. 6.18 shows the results.
From Fig.s 6.17b and 6.16b, the different operation of sSSHI and SECE HI can be appreciated for the same resistive load, $R_L = 50\,\text{k}\Omega$. sSSHI interface performs inversion when V_T achieves a peak while SECE interface performs C_p discharge. Considering

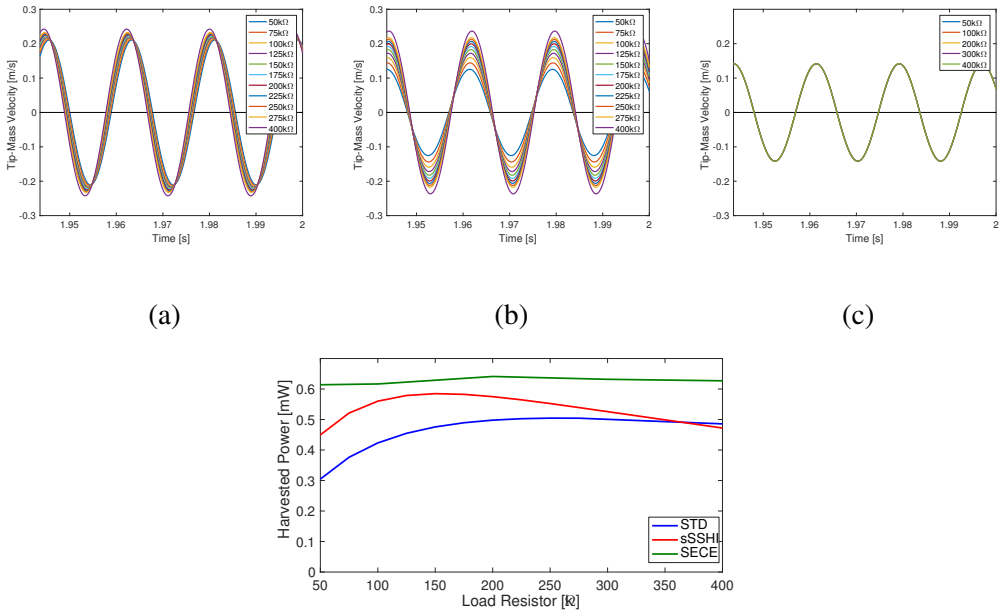

(a) (b) (c)

(d)

Fig. 6.18 Numerical comparison among STD, sSSHI and SECE interfaces. Tip mass velocity in the case of a) STD, b) sSSHI and c) SECE interface for different load resistor values. d) Harvested power as a function of R_L.

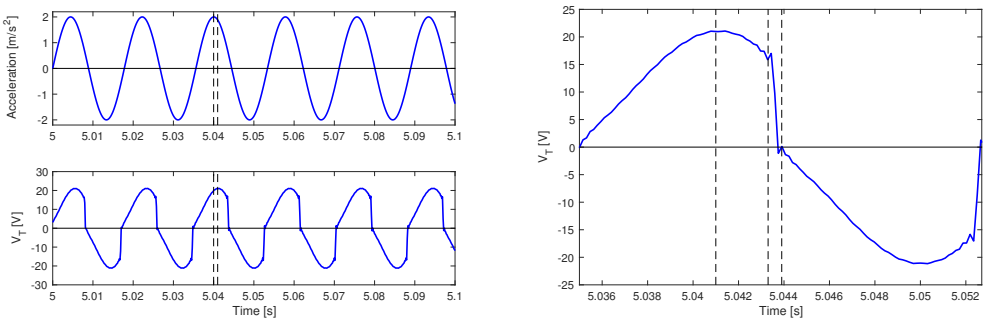

Fig. 6.19 SECE technique: experimental voltage response to 2 m/s^2 56.2 Hz sinusoidal input acceleration.

the tip mass velocity plotted in Fig.s 6.18a, 6.18b and 6.18c, the damping induced by the electrical part to the mechanical results. It is evident as the damping effect is strictly connected to the value of the resistive load when STD and sSSHI interfaces are used. For the considered range of R_L, induced damping is higher in the case of sSSHI interface. In the case of SECE interface, load decoupling results and the oscillation amplitude no more depends on R_L. The drawback of this configuration is that for low level of input acceleration, the induced damping may result to penalising for the dynamics of the system.

Fig. 6.18d shows the harvested power, namely the power dissipated on the resistive load, as a function of R_L. Again, the recovery performance of the SECE interface does not depend on R_L and is about 0.62 mW. Conversely, STD and sSSHI interfaces present an optimal load. As expected, the optimal resistive load for the sSSHI interface is lower than the one of the STD: respectively 0.58 mW at 150 k$\Omega$and 0.50 mW at 250 kΩ.

From the numerical analysis, the higher effectiveness of the SECE technique derives. Thus this solution has been experimentally implemented and tested. Fig. 6.19 shows the voltage response to the 2 m/s^2 56.2 Hz input sinusoidal acceleration. Due to both mechanical and both electrical parameters of the system, a 1.09 ms time delay occurs between the acceleration (and thus displacement) maximum and the transducer voltage one. Due to the electronics driving the switch, the synchronisation between the transducer voltage peak and the switch activation is not perfect but a 2.19 ms delay occurs before the discharging phase begins. This phase is slower than in the simulations and lasts for 35 ms.

Considering the amplitude of the voltage trend, the experimental analysis highlights that the prototyped device presents voltage peaks slightly smaller than in the numeri-

cal simulations, 22 V in the first case against the 24 V of the second. The same stands for the harvested power performance. In the numerical case the harvested power is 0.62 mW while the developed device recovers 0.56 mW.

6.5 Piezoelectric EH conclusions and future developments

In this chapter, the energy harvesting project derived by the partnership between the *Department of Management and Production Engineering* of Politecnico di Torino and the *Matériaux, Machines et Dispositifs Electromagnétiques Avancés* team of the Grenoble Electrical Engineering Laboratory has been descibed.
In order to investigate the piezoelectric energy harvesting capability, a complete piezoelectric EH system has been designed, analysed and tested.
The developed device performs mechanical energy extraction and conversion exploiting the oscillation of a mass placed at the free-end of a cantilever beam with a piezoelectric patch bonded on the upper surface. The system is embedded with self powered electric interface for power managing and recovery performance increase.
After the design of the mechanical part of device and the experimental identification of the system parameters, sSSHI and SECE electrical interfaces based on synchronised switching have been numerically simulated. Exploiting voltage peak detection by means of the electronic breaker, the logic driving the switch of the interface is made self-powered and with no need of external additional power source.
Numerical results show that the harvested power implementing SECE and sSSHI are 0.62 and 0.58 mW in response to 2 m/s^2 56,2 Hz sinusoidal input, respectively the 125% and the 115% of that in case of STD interface. Considering the k^2Q_m of the prototyped piezoelectric beam, these techniques allow recovering the same amount of energy of the standard one by using a piezoelectric patch about 10 times smaller.
Due to the better performance in terms of harvested power and in terms of electric load decoupling derived from the numerical analysis for the SECE interface, this solution has been prototyped and experimentally tested. In response to the same sinusoidal input, experimental recovery performance are slightly lower than the numerical, 0.56 mW against 0.62 mW, but still compliant with standard low-power electronics. The higher amount of losses in the circuit and in the switch control

electronics leads to higher time delay between voltage peak and switch activation, and to voltage levels slightly lower than the expected.

Piezoelectric energy harvesting has demonstrated to be a suitable solution for energy recovery from low frequency mechanical vibration. A deeper experimental analysis is still necessary to point out issues and difficulties in the device manufacturing, especially when miniaturisation is considered.

Chapter 7

Conclusions and future developments

The aim of developing infinite-life autonomous wireless electronics, powered by the energy of the surrounding environment, drives the research efforts in the field of Energy Harvesting. Electromagnetic and piezoelectric techniques for vibrational energy harvesting are deemed to be the most attractive technologies for powering small-scale autonomous electronic devices due to their energy source power density, versatility and abundance in the environment.

This thesis derives from the partnership between Politecnico di Torino and STMicroelectronics and is targeted to investigate both the electromagnetic and both the piezoelectric technology applied to the energy harvesting in order to design and develop functional prototypes. For both the technologies, the research project focuses on the entire energy conversion chain: the mechanical structure for the extraction from the environment, the transduction mechanism for the conversion, the electric interface for performance maximisation. In the first part, a unified SDOF approach is used to develop a global lumped parameter model to describe the behaviour of the energy harvesting system under the application of a kinematic input to the host structure. The model, implementing the mobility electromechanical analogy, takes into account both the mechanical and both the electrical aspects involved. Subsequently, system modelling details and specific power managing techniques are considered in a separate analysis of the two typologies of harvester. The importance of a global optimisation of the EH features is highlighted. The analysis shows that circuit topologies implementing non-linear techniques allow increasing harvesting performance in terms of recovered power for a given device or in terms of needed

active material for a given energy target.
Basing on the resulting outcomes, the analytical models are applied to the development of two energy harvesting demonstrators: a self-powered Bluetooth step counter placed in the sole of a training shoe that exploits magneto induction to convert environmental energy, and a piezoelectric cantilever beam energy harvester embedded with a self-powered HI.

In the context of the collaboration with the AMG team of STMicroelectronics, the project of a self-powered Bluetooth step counter has been carried out. The aim is to power supply a wireless electronic device for the foot-step sensing placed in the sole of a training shoe exploiting only the energy harvested by the impact of the heel on the ground during each foot-step of running activity. The developed device is a cylinder $\varnothing\, 27 \times 16$ mm including the mechanical part, the interface circuit for power managing and performance maximisation, the step-counter electronics and the protective shell.
Environmental energy extraction occurs exploiting the vibration of a permanent magnet in response to the specific acceleration input. Energy conversion is performed via electromagnetic induction by coupling the permanent magnet with an induction coil. For the maximum power transfer to a storage capacitor for the load supply, the device is embedded with a self-powered electronic interface. Based on a full wave boost converter driven by an ultra-low power microcontroller equipped with a current controller, the interface exploits PWM for optimal resistive load emulation and load decoupling.
Although the variable nature of the energy source and the stringent constraints, experimental tests performed reproducing the acceleration profile sampled in the sole af a shoe during running demonstrate that the electric load power requirement is satisfied at each foot-step. This result is achieved by means of an effective and reliable design tool developed in Matlab Simulink environment that takes into account the multi-physics nature of the system. Mechanical modelling is optimised with respect to the specific application. Performance of the proposed electric interface is double with respect to that of standard technique. Considering the upper limit fixed by the energy dissipated on the optimal resistive load, the developed device is able to recover the 90% of that energy.
Experimental analysis conducted on a batch of prototypes highlighted that, although encouraging results have been achieved, self-powered step-counter performance in terms of repeatability and reliability needs to be improved. New mechanical springs

topology is under evaluation in order to better control system stiffness and magnet positioning during functioning.

In the context of the collaboration with the Grenoble Electrical Engineering Laboratory under the supervision of the AMG team of STMicroelectronics, the project of a piezoelectric energy harvester based on a cantilever beam has been carried out. With the aim of exploiting environmental vibrations with a frequency in the range of 40 and 100 Hz for energy recovery, a system consisting of a stainless steel beam 60 mm long, 25 mm wide and 0.5 mm tick, with a MFC piezoelectric patch bonded on the upper surface and a proof mass at the free-end has been designed, analysed and tested on a shaker for the experimental identification of the system parameters. The device is embedded with a self-power electric interface for harvesting performance maximisation. SECE and sSSHI techniques based on synchronised switching have been considered. Numerical results show that harvesting performance are respectively the 125% and the 115% of that in case of STD interface confirming the effectiveness of these solutions. In addition, considering the k^2Q_m of the prototyped piezoelectric beam, these techniques allow recovering the same amount of energy of the standard one by using a piezoelectric patch about 10 times smaller.
Due to the better performance in terms of harvested power and in terms of electric load decoupling, SECE interface has been prototyped and experimentally tested. In response to 2 m/s^2 56,2 Hz sinusoidal input, experimental power recovery of 0.56 mW is achieved demonstrating that this device is compliant with standard low-power electronics requirements.
Piezoelectric energy harvesting has demonstrated to be a suitable solution for energy recovery but deeper experimental analysis is still necessary to point out issues and difficulties in the device manufacturing, especially when miniaturisation is considered.

References

[1] Jean-Christophe Eloy and Eric Mounier. Status of the mems industry. In *MOEMS-MEMS Micro & Nanofabrication*, pages 43–49. International Society for Optics and Photonics, 2005.

[2] Internet of things – iot guide with definitions, examples, trends and use cases. https://www.i-scoop.eu/internet-of-things-guide. [Last accessed on Feb. 26, 2017].

[3] Questel new portal for patent. https://www.orbit.com/. [Last accessed on Feb. 26, 2017].

[4] Wenzhao Jia, Gabriela Valdés-Ramírez, Amay J Bandodkar, Joshua R Windmiller, and Joseph Wang. Epidermal biofuel cells: energy harvesting from human perspiration. *Angewandte Chemie International Edition*, 52(28):7233–7236, 2013.

[5] Wei Guo, Liuxuan Cao, Junchao Xia, Fu-Qiang Nie, Wen Ma, Jianming Xue, Yanlin Song, Daoben Zhu, Yugang Wang, and Lei Jiang. Energy harvesting with single-ion-selective nanopores: A concentration-gradient-driven nanofluidic power source. *Advanced functional materials*, 20(8):1339–1344, 2010.

[6] Stephen Beeby and Neil M White. *Energy harvesting for autonomous systems*. Artech House, 2010.

[7] Mickaël Lallart and Daniel Guyomar. *Ferroelectric materials for small-scale energy harvesting devices and green energy products*. INTECH Open Access Publisher, 2011.

[8] Stefano Tornincasa, Maurizio Repetto, Elvio Bonisoli, and Francesco Di Monaco. Energy harvester for vehicle tires: Nonlinear dynamics and experimental outcomes. *Journal of Intelligent Material Systems and Structures*, 23(1):3–13, 2012.

[9] Elvio Bonisoli, Nicoló Manca, and Maurizio Repetto. Multi-physics optimisation of energy harvesters. *COMPEL: The International Journal for Computation and Mathematics in Electrical and Electronic Engineering*, 34(5):1392–1403, 2015.

[10] Elvio Bonisoli, Maurizio Repetto, Nicoló Manca, and Alessandro Gasparini. Electro-mechanical and electronic integrated harvester for shoes application. *IEEE/ASME Transactions on Mechatronics*, 2017.

[11] Mark Billinghurst and Daniela Busse. Rapid prototyping for wearables: concept design and development for head- and wrist-mounted wearables (smart watches and google glass). In *Proceedings of the Ninth International Conference on Tangible, Embedded, and Embodied Interaction*. ACM, 2015.

[12] Argenis Bilbao, Davis Hoover, Jennifer Rice, and Jamie Chapman. Ultra-low power wireless sensing for long-term structural health monitoring. *Sensors and Smart Structures Technologies for Civil, Mechanical, and Aerospace Systems (San Diego, California, USA,)*, pages 798109–14, 2011.

[13] KA Cook-Chennault, N Thambi, and AM Sastry. Powering mems portable devices—a review of non-regenerative and regenerative power supply systems with special emphasis on piezoelectric energy harvesting systems. *Smart Materials and Structures*, 17(4):043001, 2008.

[14] Helios Vocca and Francesco Cottone. Kinetic energy harvesting. *ICT-Energy-Concepts Towards Zero-Power Information and Communication Technology*, pages 25–48, 2014.

[15] James P Thomas, Muhammad A Qidwai, and James C Kellogg. Energy scavenging for small-scale unmanned systems. *Journal of Power sources*, 159(2):1494–1509, 2006.

[16] Adnan Harb. Energy harvesting: State-of-the-art. *Renewable Energy*, 36(10):2641–2654, 2011.

[17] Jan M. Rabaey, M. Josie Ammer, Julio L. da Silva, Danny Patel, and Shad Roundy. Picoradio supports ad hoc ultra-low power wireless networking. *Computer*, 33(7):42–48, 2000.

[18] Shad Roundy, Paul K Wright, and Jan Rabaey. A study of low level vibrations as a power source for wireless sensor nodes. *Computer communications*, 26(11):1131–1144, 2003.

[19] Joseph A Paradiso and Thad Starner. Energy scavenging for mobile and wireless electronics. *IEEE Pervasive computing*, 4(1):18–27, 2005.

[20] Ruud JM Vullers, Vladimir Leonov, Tom Sterken, and Andreas Schmitz. Energy scavengers for wireless intelligent microsystems. *On Board Technol., June*, page 34, 2006.

[21] Eugenio Cantatore and Martin Ouwerkerk. Energy scavenging and power management in networks of autonomous microsensors. *Microelectronics journal*, 37(12):1584–1590, 2006.

[22] Paul D Mitcheson, Eric M Yeatman, G Kondala Rao, Andrew S Holmes, and Tim C Green. Energy harvesting from human and machine motion for wireless electronic devices. *Proceedings of the IEEE*, 96(9):1457–1486, 2008.

[23] JW Matiko, NJ Grabham, SP Beeby, and MJ Tudor. Review of the application of energy harvesting in buildings. *Measurement Science and Technology*, 25(1):012002, 2013.

[24] JFM Oudenhoven, RJM Vullers, and R Schaijk. A review of the present situation and future developments of micro-batteries for wireless autonomous sensor systems. *International Journal of Energy Research*, 36(12):1139–1150, 2012.

[25] Adolf Goetzberger, Christopher Hebling, and Hans-Werner Schock. Photovoltaic materials, history, status and outlook. *Materials Science and Engineering: R: Reports*, 40(1):1–46, 2003.

[26] Hossein Mousazadeh, Alireza Keyhani, Arzhang Javadi, Hossein Mobli, Karen Abrinia, and Ahmad Sharifi. A review of principle and sun-tracking methods for maximizing solar systems output. *Renewable and sustainable energy reviews*, 13(8):1800–1818, 2009.

[27] Trishan Esram and Patrick L Chapman. Comparison of photovoltaic array maximum power point tracking techniques. *IEEE Transactions on Energy Conversion EC*, 22(2):439, 2007.

[28] Xin Lu and Shuang-Hua Yang. Thermal energy harvesting for wsns. In *Systems Man and Cybernetics (SMC), 2010 IEEE International Conference on*, pages 3045–3052. IEEE, 2010.

[29] Sun Jin Kim, Ju Hyung We, and Byung Jin Cho. A wearable thermoelectric generator fabricated on a glass fabric. *Energy & Environmental Science*, 7(6):1959–1965, 2014.

[30] A Cuadras, M Gasulla, and Vittorio Ferrari. Thermal energy harvesting through pyroelectricity. *Sensors and Actuators A: Physical*, 158(1):132–139, 2010.

[31] Poorna Mane, Jingsi Xie, Kam K Leang, and Karla Mossi. Cyclic energy harvesting from pyroelectric materials. *IEEE transactions on ultrasonics, ferroelectrics, and frequency control*, 58(1):10–17, 2011.

[32] Andreas Molisch. *Wireless Communications*. John Wiley & Sons, 2nd edition, 2011.

[33] Hiroshi Nishimoto, Yoshihiro Kawahara, and Tohru Asami. Prototype implementation of ambient RF energy harvesting wireless sensor networks. In *Sensors, 2010 IEEE*, pages 1282–1287. IEEE, 2010.

[34] RJM Vullers, Rob van Schaijk, Inge Doms, Chris Van Hoof, and R Mertens. Micropower energy harvesting. *Solid-State Electronics*, 53(7):684–693, 2009.

[35] Thomas Lafont, L Gimeno, J Delamare, GA Lebedev, DI Zakharov, B Viala, O Cugat, N Galopin, L Garbuio, and O Geoffroy. Magnetostrictive–piezoelectric composite structures for energy harvesting. *Journal of Micromechanics and Microengineering*, 22(9):094009, 2012.

[36] Yuan Rao and David P Arnold. Input-powered energy harvesting interface circuits with zero standby power. In *Applied Power Electronics Conference and Exposition (APEC), 2011 Twenty-Sixth Annual IEEE*, pages 1992–1999. IEEE, 2011.

[37] Dominic Maurath, Philipp F Becker, Dirk Spreemann, and Yiannos Manoli. Efficient energy harvesting with electromagnetic energy transducers using active low-voltage rectification and maximum power point tracking. *IEEE Journal of Solid-State Circuits*, 47(6):1369–1380, 2012.

[38] Emmanuelle Arroyo and Adrien Badel. Electromagnetic vibration energy harvesting device optimization by synchronous energy extraction. *Sensors and Actuators A: Physical*, 171(2):266–273, 2011.

[39] Daniel Guyomar and Mickaël Lallart. Recent progress in piezoelectric conversion and energy harvesting using nonlinear electronic interfaces and issues in small scale implementation. *Micromachines*, 2(2):274–294, 2011.

[40] Tra Nguyen Phan, Mehdi Azadmehr, Cuong Phu Le, and Einar Halvorsen. Low power electronic interface for electrostatic energy harvesters. In *Journal of Physics: Conference Series*, volume 660, page 012087. IOP Publishing, 2015.

[41] Perpetuum ltd. http:///perpetuum.com. [Last accessed on Feb 5, 2017].

[42] Ferro solutions inc. http://www.ferrosi.com. [Last accessed on Feb 5, 2017].

[43] Mide volture. http://http://www.mide.com. [Last accessed on Feb 5, 2017].

[44] Steve P Beeby, RN Torah, MJ Tudor, P Glynne-Jones, T O'Donnell, CR Saha, and S Roy. A micro electromagnetic generator for vibration energy harvesting. *Journal of Micromechanics and microengineering*, 17(7):1257, 2007.

[45] Shad Roundy, Paul K Wright, and Kristofer SJ Pister. Micro-electrostatic vibration-to-electricity converters. In *ASME 2002 International Mechanical Engineering Congress and Exposition*, pages 487–496. American Society of Mechanical Engineers, 2002.

[46] Fabio Peano and Tiziana Tambosso. Design and optimization of a MEMS electret-based capacitive energy scavenger. *IEEE/ASME Journal of Microelectromechanical Systems*, 14(3):429–435, 2005.

[47] P Basset, D Galayko, A Mahmood Paracha, F Marty, A Dudka, and T Bourouina. A batch-fabricated and electret-free silicon electrostatic vibration energy harvester. *Journal of Micromechanics and Microengineering*, 19(11):115025, 2009.

[48] P Miao, PD Mitcheson, AS Holmes, EM Yeatman, TC Green, and BH Stark. MEMS inertial power generators for biomedical applications. *Microsystem Technologies*, 12(10-11):1079–1083, 2006.

[49] Dejan Vasic, Yu-Yin Chen, and François Costa. Self-powered piezoelectric energy harvester for bicycle. *Journal of Mechanical Science and Technology*, 28(7):2501–2510, 2014.

[50] Guang Zhu, Aurelia C Wang, Ying Liu, Yusheng Zhou, and Zhong Lin Wang. Functional electrical stimulation by nanogenerator with 58 v output voltage. *Nano letters*, 12(6):3086–3090, 2012.

[51] Henry A Sodano, G Park, and DJ Inman. Estimation of electric charge output for piezoelectric energy harvesting. *Strain*, 40(2):49–58, 2004.

[52] Elie Lefeuvre, Adrien Badel, Claude Richard, and Daniel Guyomar. Piezoelectric energy harvesting device optimization by synchronous electric charge extraction. *Journal of Intelligent Material Systems and Structures*, 16(10):865–876, 2005.

[53] Hui Shen, Jinhao Qiu, Hongli Ji, Kongjun Zhu, and Marco Balsi. Enhanced synchronized switch harvesting: a new energy harvesting scheme for efficient energy extraction. *Smart Materials and Structures*, 19(11):115017, 2010.

[54] Adrien Badel, Manuel Lagache, D Guyomar, Elie Lefeuvre, and C Richard. Finite element and simple lumped modeling for flexural nonlinear semi-passive damping. *Journal of Intelligent Material Systems and Structures*, 2007.

[55] CB Williams and Rob B Yates. Analysis of a micro-electric generator for microsystems. *sensors and actuators A: Physical*, 52(1):8–11, 1996.

[56] NG Stephen. On energy harvesting from ambient vibration. *Journal of Sound and Vibration*, 293(1):409–425, 2006.

[57] Paul D Mitcheson and Tzern T Toh. Power management electronics. *Energy Harvesting for Autonomous Systems*, pages 1–57, 2010.

[58] Aldo Romani, Rudi Paolo Paganelli, Enrico Sangiorgi, and Marco Tartagni. Joint modeling of piezoelectric transducers and power conversion circuits for energy harvesting applications. *IEEE Sensors Journal*, 13(3):916–925, 2013.

[59] Kimihiko Nakano, Stephen J Elliott, and Emiliano Rustighi. A unified approach to optimal conditions of power harvesting using electromagnetic and piezoelectric transducers. *Smart Materials and Structures*, 16(4):948, 2007.

[60] P Gardonio and MJ Brennan. *Mobility and impedance methods in structural dynamics*, volume 9. chapter, 2004.

[61] A Bloch. Electromechanical analogies and their use for the analysis of mechanical and electromechanical systems. *Electrical Engineers-Part I: General, Journal of the Institution of*, 92(52):157–169, 1945.

[62] Floyd A Firestone. A new analogy between mechanical and electrical systems. *The Journal of the Acoustical Society of America*, 4(3):249–267, 1933.

[63] Michael ZQ Chen, Christos Papageorgiou, Frank Scheibe, Fu-Cheng Wang, and Malcolm C Smith. The missing mechanical circuit element. *IEEE Circuits and Systems Magazine*, 9(1):10–26, 2009.

[64] Yuan Rao and D.P. Arnold. Input-powered energy harvesting interface circuits with zero standby power. In *Applied Power Electronics Conference and Exposition (APEC), 2011 Twenty-Sixth Annual IEEE*, pages 1992–1999, March 2011.

[65] Gyorgy D Szarka, Stephen G Burrow, Plamen P Proynov, and Bernard H Stark. Maximum power transfer tracking for ultralow-power electromagnetic energy harvesters. *IEEE Transactions on Power Electronics*, 29(1):201–212, 2014.

[66] Mickaël Lallart, Lauric Garbuio, Lionel Petit, Claude Richard, and Daniel Guyomar. Double synchronized switch harvesting (dssh): a new energy harvesting scheme for efficient energy extraction. *IEEE transactions on ultrasonics, ferroelectrics, and frequency control*, 55(10):2119–2130, 2008.

[67] Elie Lefeuvre, Claude Richard, Daniel Guyomar, and Mickail Lallart. *Piezoelectric material-based energy harvesting devices: advance of SSH optimization techniques (1999-2009).* INTECH Open Access Publisher, 2010.

[68] Junrui Liang and Wei-Hsin Liao. An improved self-powered switching interface for piezoelectric energy harvesting. In *Information and Automation, 2009. ICIA'09. International Conference on*, pages 945–950. IEEE, 2009.

[69] Stephen P Beeby and Terence O'Donnell. Electromagnetic energy harvesting. In *Energy Harvesting Technologies*, pages 129–161. Springer, 2009.

[70] Paul D Mitcheson, Elizabeth K Reilly, T Toh, Paul K Wright, and Eric M Yeatman. Performance limits of the three mems inertial energy generator transduction types. *Journal of Micromechanics and Microengineering*, 17(9):S211, 2007.

[71] Thorsten Hehn and Yiannos Manoli. *Piezoelectricity and Energy Harvester Modelling*, pages 21–40. Springer Netherlands, Dordrecht, 2015.

[72] Emmanuelle Arroyo. *Récupération d'énergie à partir des vibrations ambiantes: dispositif électromagnétique et circuit électronique d'extraction synchrone*. PhD thesis, Université de Grenoble, 2012.

[73] AH Meitzler, HF Tiersten, AW Warner, D Berlincourt, GA Couqin, and FS Welsh III. Ieee standard on piezoelectricity, 1988.

[74] Shad Roundy, Paul Kenneth Wright, and Jan M Rabaey. *Energy scavenging for wireless sensor networks*. Springer, 2003.

[75] M Renaud, K Karakaya, Tom Sterken, P Fiorini, Christiaan Van Hoof, and Robert Puers. Fabrication, modelling and characterization of mems piezoelectric vibration harvesters. *Sensors and Actuators A: Physical*, 145:380–386, 2008.

[76] Daniel Guyomar, Adrien Badel, Elie Lefeuvre, and Claude Richard. Toward energy harvesting using active materials and conversion improvement by nonlinear processing. *IEEE transactions on ultrasonics, ferroelectrics, and frequency control*, 52(4):584–595, 2005.

[77] Yuan-Ping Liu and Dejan Vasic. *Self-powered electronics for piezoelectric energy harvesting devices*. INTECH Open Access Publisher, 2012.

[78] Jamil M Renno, Mohammed F Daqaq, and Daniel J Inman. On the optimal energy harvesting from a vibration source. *Journal of sound and vibration*, 320(1):386–405, 2009.

[79] Michael Renaud, Paolo Fiorini, and Chris Van Hoof. Optimization of a piezoelectric unimorph for shock and impact energy harvesting. *Smart Materials and Structures*, 16(4):1125, 2007.

[80] Yu-Jen Wang, Chung-De Chen, and Cheng-Kuo Sung. System design of a weighted-pendulum-type electromagnetic generator for harvesting energy from a rotating wheel. *Mechatronics, IEEE/ASME Transactions on*, 18(2):754–763, April 2013.

[81] S. Sadeqi, S. Arzanpour, and K.H. Hajikolaei. Broadening the frequency bandwidth of a tire-embedded piezoelectric-based energy harvesting system using coupled linear resonating structure. *Mechatronics, IEEE/ASME Transactions on*, PP(99):1–10, November 2014.

[82] J.J. Wang, G.P. Penamalli, and Lei Zuo. Electromagnetic energy harvesting from train induced railway track vibrations. In *Mechatronics and Embedded Systems and Applications (MESA), 2012 IEEE/ASME International Conference on*, pages 29–34, July 2012.

[83] Xiudong Tang, Teng Lin, and Lei Zuo. Design and optimization of a tubular linear electromagnetic vibration energy harvester. *Mechatronics, IEEE/ASME Transactions on*, 19(2):615–622, April 2014.

[84] N.G. Elvin and A.A. Elvin. Vibrational energy harvesting from human gait. *Mechatronics, IEEE/ASME Transactions on*, 18(2):637–644, April 2013.

[85] N.S. Shenck and J.A. Paradiso. Energy scavenging with shoe-mounted piezoelectrics. *Micro, IEEE*, 21(3):30–42, May 2001.

[86] José Gerardo Rocha, Luis Miguel Goncalves, PF Rocha, MP Silva, and Senentxu Lanceros-Mendez. Energy harvesting from piezoelectric materials fully integrated in footwear. *Industrial Electronics, IEEE Transactions on*, 57(3):813–819, 2010.

[87] Wen G Li, Siyuan He, and Shudong Yu. Improving power density of a cantilever piezoelectric power harvester through a curved l-shaped proof mass. *Industrial Electronics, IEEE Transactions on*, 57(3):868–876, 2010.

[88] L. Moro and D. Benasciutti. Harvested power and sensitivity analysis of vibrating shoe-mounted piezoelectric cantilevers. *Smart Materials and Structures*, 19(11):115011, 2010.

[89] Dan Dai, Jing Liu, and Yixin Zhou. Harvesting biomechanical energy in the walking by shoe based on liquid metal magnetohydrodynamics. *Frontiers in Energy*, 6(2):112–121, 2012.

[90] D. Carroll and M. Duffy. Modelling, design, and testing of an electromagnetic power generator optimized for integration into shoes. *Proceedings of the Institution of Mechanical Engineers, Part I: Journal of Systems and Control Engineering*, 226(2):256–270, 2012.

[91] Can-Fei Wang, Dong-Min Miao, P.C.-K. Luk, Jian-Xin Shen, Chi Xu, and Dan Shi. A shoe-equipped linear generator for energy harvesting. In *Sustainable Energy Technologies (ICSET), 2010 IEEE International Conference on*, pages 1–6, December 2010.

[92] R. Baghbani and M. Ashoorirad. A power generating system for mobile electronic devices using human walking motion. In *Computer and Electrical Engineering, 2009. ICCEE '09. Second International Conference on*, volume 2, pages 385–388, December 2009.

[93] K Ylli, D Hoffmann, A Willmann, P Becker, B Folkmer, and Y Manoli. Energy harvesting from human motion: exploiting swing and shock excitations. *Smart Materials and Structures*, 24(2):025029, 2015.

[94] T Scott Saponas, Jonathan Lester, Carl Hartung, and Tadayoshi Kohno. Devices that tell on you: The nike+ ipod sport kit. *Dept. of Computer Science and Engineering, University of Washington, Tech. Rep*, 2006.

[95] Nike+ iPod frequently asked questions (technical). http://support-en-us.nikeplus.com/app/answers/detail/a_id/20936/p/4282,4291,4292. [Last accessed on May 31, 2016].

[96] BP Mann and ND Sims. Energy harvesting from the nonlinear oscillations of magnetic levitation. *Journal of Sound and Vibration*, 319(1):515–530, 2009.

[97] PL Green, K Worden, K Atallah, and ND Sims. The benefits of duffing-type nonlinearities and electrical optimisation of a mono-stable energy harvester under white gaussian excitations. *Journal of Sound and Vibration*, 331(20):4504–4517, 2012.

[98] Harold A Wheeler. Simple inductance formulas for radio coils. *Proceedings of the Institute of Radio Engineers*, 16(10):1398–1400, 1928.

[99] Dirk Spreemann and Yiannos Manoli. *Electromagnetic vibration energy harvesting devices: Architectures, design, modeling and optimization*, volume 35. Springer Science & Business Media, 2012.

[100] D Meeker. Finite element method magnetics. http://www.femm.info. [Last accessed on December 31, 2016].

[101] Stefano Tornincasa, Elvio Bonisoli, Francesco Di Monaco, Sandro Moos, Maurizio Repetto, and Fabio Freschi. Nonlinear dynamics of an electromechanical energy scavenger. In *Modal Analysis Topics, Volume 3*, pages 339–349. Springer, 2011.

[102] ZQ Li, YL Xu, and LM Zhou. Adjustable fluid damper with sma actuators. *Smart materials and structures*, 15(5):1483, 2006.

[103] Robert Hooke and Terry A Jeeves. Direct search solution of numerical and statistical problems. *Journal of the ACM (JACM)*, 8(2):212–229, 1961.

[104] M. Hendijanizadeh, S.M. Sharkh, and M. Moshrefi-Torbati. Energy harvesting from a rotational transducer under random excitation. *Journal of Renewable and Sustainable Energy*, 6(4):043120, 2014.

[105] G Gatti, MJ Brennan, MG Tehrani, and DJ Thompson. Harvesting energy from the vibration of a passing train using a single-degree-of-freedom oscillator. *Mechanical Systems and Signal Processing*, 66:785–792, 2016.

[106] Kevin Remick, D Dane Quinn, D Michael McFarland, Lawrence Bergman, and Alexander Vakakis. High-frequency vibration energy harvesting from impulsive excitation utilizing intentional dynamic instability caused by strong nonlinearity. *Journal of Sound and Vibration*, 370:259–279, 2016.

[107] Mentor Graphics, ELDO. https://www.mentor.com/products/ic_nanometer_design/analog-mixed-signal-verification/eldo/?sfm=free_form. [Last accessed on May 31, 2016].

[108] Thomas Daue and Jan Kunzmann. Energy harvesting systems using piezoelectric mfcs. In *2008 17th IEEE International Symposium on the Applications of Ferroelectrics*, volume 1, pages 1–1. IEEE, 2008.

[109] Alexander G Mihalca, Jonathan G Drosinos, Malika Grayson, and Ephrahim Garcia. Using aeroelastic structures with nonlinear switching electronics to increase potential energy yield in airflow: investigating analog control circuitry for automated peak detection. In *SPIE Smart Structures and Materials+ Nondestructive Evaluation and Health Monitoring*, pages 94390K–94390K. International Society for Optics and Photonics, 2015.

[110] Yu-Yin Chen, Dejan Vasic, François Costa, Chih-Kung Lee, and Wen-Jong Wu. Self-powered semi-passive piezoelectric structural damping based on zero-velocity crossing detection. *Smart Materials and Structures*, 22(2):025029, 2013.

[111] Mickaël Lallart and Daniel Guyomar. An optimized self-powered switching circuit for non-linear energy harvesting with low voltage output. *Smart Materials and Structures*, 17(3):035030, 2008.

Appendix A

A and *B* coefficients calculation

In a cantilever beam EH system, the piezoelectric force F acting on the piezoelectric patch along the 1 direction, due to the characteristics of the system produces a force F_T applied to the free-end of the cantilever beam along the z axis. In the same way, the displacement of the free-end along the z axis, due to the characteristics of the system induces elongation along the 1 direction of the piezoelectric patch.
In order to correlate the dynamics of the free-end of the beam to that of the electrical part of the system, it is necessary to refer the force F and the elongation speed $\dot{\varepsilon}$ of eq. 4.31 to the force F_T and the relative velocity $\dot{z}_r$ by means of two coefficients A and B. In the following the two coefficients are derived.

A **coefficient** When voltage ia applied at the piezoelectric patch along the 3 direction, a force F is produced along the 1 direction due to piezoelectric 31 effect.

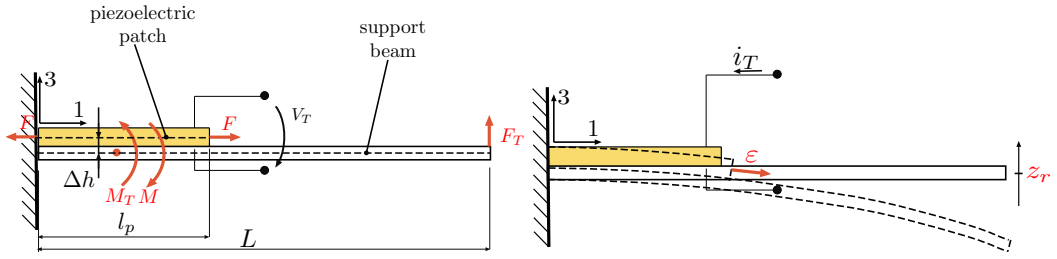

(a) (b)

Fig. A.1 Piezoelectric cantilever beam schemes for a) the calculation of A and b) B coefficients.

Being the patch neutral surface at a distance Δh from the neutral surface of the support beam, the piezoelectric layer imposes a moment M to the support beam. The equilibrium of the system is achieved applying a force F_T at the free-end of the support beam that generates a moment M_T that opposes M, Fig. A.1a. The coefficient that relates F and F_T is derived as follows.

$$M_T + M = 0 \tag{A.1}$$

$$F_T\left(L - \frac{l_p}{2}\right) + F\Delta h = 0 \tag{A.2}$$

$$F_T + \frac{\Delta h}{\left(L - \frac{l_p}{2}\right)} F = 0 \tag{A.3}$$

$$F_T = -\frac{\Delta h}{\left(L - \frac{l_p}{2}\right)} F = -AF \tag{A.4}$$

$$\Rightarrow A = \frac{\Delta h}{\left(L - \frac{l_p}{2}\right)} \tag{A.5}$$

***B* coefficient** A displacement z imposed to the free-end of the piezoelectric beam induces a curvature to the neutral surface, Fig. A.1b. In the hypothesis that the mechanical proprieties of the piezoelectric material are negligible with respect to that of the support beam material, and thus the neutral surface of the support beam is not shifted, the curvature of the neutral surface of the cantilever beam loaded at the free end and its displacement are:

$$\frac{d^2 z_r}{dx^2} = \frac{F_T}{E_s I_s}(L - x) \tag{A.6}$$

$$z_r = \frac{L^3}{3E_s I_s} F_T \tag{A.7}$$

$$\Rightarrow \frac{d^2 z_r}{dx^2} = \frac{3}{L^3} z_r (L - x) \tag{A.8}$$

Being the patch at a distance Δh from the neutral surface of the support beam, strain is induced along the 1 direction. The average strain is obtained integrating $\delta_1(x)$

along the priezoelectric patch:

$$\delta_1(x) = -\Delta h \frac{d^2 z_r}{dx^2} = -\Delta h \frac{3}{L^3} z_r (L-x) \tag{A.9}$$

$$\delta_1 = -\frac{3\Delta h\, z_r}{L^3} \frac{1}{l_p} \int_0^{l_p} (L-x)dx = -\frac{3\Delta h}{L^3} z_r \big(L - \frac{l_p}{2}\big) \tag{A.10}$$

The piezoelectric patch elongation is:

$$\varepsilon = l_p \delta_1 = -l_p \frac{3\Delta h}{L^3} \big(L - \frac{l_p}{2}\big) z_r = -B z_r \tag{A.11}$$

$$\Rightarrow B = l_p \frac{3\Delta h}{L^3} \big(L - \frac{l_p}{2}\big) \tag{A.12}$$

$$\dot{\varepsilon} = -B \dot{z}_r \tag{A.13}$$